Title
Acoustically Driven Ferromagnetic Resonance for Device Applications

Author
Labanowski, Dominic

Publication Date
2017

Peer reviewed|Thesis/dissertation

Acoustically Driven Ferromagnetic Resonance for Device Applications

by

Dominic Labanowski

A dissertation submitted in partial satisfaction of the

requirements for the degree of

Doctor of Philosophy

in

Engineering - Electrical Engineering and Computer Sciences

in the

Graduate Division

of the

University of California, Berkeley

Committee in charge:

Professor Sayeef Salahuddin, Chair
Professor Ali Niknejad
Professor Ramamoorthy Ramesh

Fall 2017

Acoustically Driven Ferromagnetic Resonance for Device Applications

Abstract

Acoustically Driven Ferromagnetic Resonance for Device Applications

by

Dominic Labanowski

Doctor of Philosophy in Engineering - Electrical Engineering and Computer Sciences

University of California, Berkeley

Professor Sayeef Salahuddin, Chair

Magnetic devices have become increasingly integrated into modern technology as they enable technologies as varied as computer hard drives, RF circulators, and medical diagnostic equipment. Electrically controlling magnetism in the small scale, however, has always been difficult due to the inefficiencies of generating the localized nanoscale magnetic fields necessary to precisely control such devices. Traditional macroscale methods (such as simple Oersted fields) fail when scaled to the sizes of modern device components, and even the most efficient established techniques (spin transfer torque, spin hall effect) are current-based and thus dissipate substantial power when used to switch magnetic elements.

Recent work in the field of multiferroic materials has opened the potential for using voltage, rather than current, to manipulate magnetism in these systems, potentially increasing the efficiency of nanoscale magnetic control by several orders of magnitude. In this thesis, we explore the Acoustically Driven Ferromagnetic Resonance effect in composite strain-coupled multiferroic bilayers. This technique allows for a voltage-driven piezoelectric excitation to drive magnetostrictive thin films into resonance with a much greater coupling efficiency than is possible using traditional methods. By leveraging this enhanced coupling, it is possible to develop a number of novel devices based on this interaction that span a number of extremely important commercial fields.

This thesis experimentally explores the dependence of this effect on a number of factors such as operating frequency, input power, magnetic element size and thickness, and magnetic element composition. We also study three high-potential applications for this technology: magnetic sensing, antenna miniaturization, and room-temperature coupling to quantum systems - specifically diamond nitrogen-vacancy centers. While some of these applications are far from commercial readiness, we are able to demonstrate proof-of-concept examples for each of these concepts that demonstrate that the core concept is valid and is worth further exploration.

To my family

Thank you for your support and guidance throughout the years

Contents

List of Figures

List of Tables

Acknowledgments

I would like to begin by thanking my advisor, Sayeef Salahuddin, for his consistent and valuable mentorship over the years. While I came into the Ph.D. program thinking I knew what I was doing, it didn't take long for me to be disillusioned of that notion. His help was instrumental towards putting me on a path where I could confront my lack of knowledge and build towards a greater understanding. Sayeef was able to present me a number of opportunities to improve and test myself during my time at Berkeley, from giving talks to writing grant proposals, that helped me better understand the non-technical side of academia. Beyond scientific competency, his ability to see the future value in incredibly nascent technologies is something that I truly admire - and is a skill I hope to develop further throughout my career.

Beyond my advisor, I would like to thank my other committee members, Ali Niknejad and Ramamoorthy Ramesh, for their advice and counsel during my graduate studies. My work touched on a number of topics and specialties outside of my core knowledge, and I greatly value the conversations I was able to have with both my committee members (and their students). Their input and advice has been critical to my success, and has dramatically enhanced my understanding of their fields. With their guidance I was not only able to accrue a greater technical understanding, but was also able to better understand the needs and struggles within their respective disciplines.

Furthermore, I would like to thank the members of TANMS for all our valuable collaborations and discussions during the course of my degree. The years of conversations we have had over a wide variety of topics have been incredibly enlightening, and have exposed me to points of view that I never would have considered had I not reached outside of Berkeley. It was truly a defining opportunity of my Ph.D. to be able to discuss my work and ideas with experts in so may diverse fields - from mechanical engineering to chemistry and ranging the gamut from experiment to theory. In addition, I greatly value the friendships that have come from these interactions, built among center retreats and funding reviews, that will hopefully far outlast my years at Berkeley. I would especially like to thank Colin, Hammy, Jackie, John, Laura, Mark, and Paul for all the valuable conversations (and plenty of entirely irrelevant ones) we had in the early years - it was people like you that really made TANMS feel like a family.

I would also like to thank my mentors and collaborators at OSU for their guidance over the better part of the last decade. Starting my journey of research as a freshman back in 2009, I had little vision for where I wanted my life to lead. The mentorship provided to me by Vidya Bhallamudi and Chris Hammel was instrumental to bringing me to where I am today. I was also especially privileged to work with these same individuals as I finished up by Ph.D. as a collaborator to share expertise and produce novel research that incorporated both our strengths.

A critical experience for me during the completion of this degree was my summer at AFRL in the summer of 2016. I would like to greatly thank Mike McConney for the opportunity and for his guidance during my time there. I would also like to thank everyone I worked

with, including Maneesh and Sahil Gupta, Brandon Howe, Amber Reed, and Piyush Shah, for their insights and support. It was great to get a view on research from a setting outside of academia and industry, and the experience definitely helped me to grow and see things from a different angle. I have fond memories of my summer spent in Dayton, and I hope that we are able to remain in touch as I move on from Berkeley and begin on an independent career.

Finally, I would like to thank all my group members for their help and support during the last few years. I will always owe Varun a debt for keeping me sane and optimistic (or at least as optimistic as I am capable of being) those first few years. I don't know how I would have been able to make the transition into grad school without a compatriot there going through everything with me. I would like to specifically thank Long for his mentorship, especially with regards to nanoscale fabrication, at the start of my degree. I would also like to thank Adi for his help in performing this work - I definitely learned and grew as I mentored you throughout your undergrad degree, and I hope that you were able to learn something from me as well. Thanks are also due to Korok, Niklas, Praveen, and Sam for being the first people I always went to with questions (academic or personal), and who I had such a variety of interesting (and universally useless) lunchtime conversations with. I would also like to thank the other members of the magnetics subgroup Debanjan and Charles, and all other members of the LEED group for their assistance and valuable discussions.

Chapter 1

Introduction

Magnetic devices have had an enormous impact on the computing industry in the form of hard disk drives[36], and have garnered further interest as non-volatile random access memories (MRAM).[78] However, while scaling for transistor technologies brings operating enhancements beyond density (for example lower power operation)[101], scaling down MRAM devices both reduces their thermal stability and thus reducing their retention time.[17] In order to combat this effect, it becomes necessary to increase the thickness of the magnetic layers and thus to increase the critical current density necessary to switch the state of the bit. The result of these tradeoffs is that even as MRAM devices are scaled, the current required to switch an individual bit does not decrease - leading to a situation where high density chips will inevitably develop power dissipation issues.

The problems with scaling MRAM devices are generally indicative of the trend that as magnetic particles scale down in size, they become more difficult to switch with conventional methods (ie. applying external Oerstead fields).[7] This realization has spurred substantial interest in the field of multiferroics[110, 98, 81, 16] - materials systems that display multiple degrees of ferroic ordering (ie. ferroelectricity and ferromagnetism) and where those ferroic orders are coupled to each other. An illustration of these coupled degrees of freedom can be seen in Figure 1.1. By using such multiferroic materials, it has been shown that the application of an electric field (without the need for a flowing charge current) is sufficient to switch the direction of the magnetization in certain systems, such as bismuth ferrite[41].

Due to the dearth of room temperature, intrinsic magnetoelectric multiferroics (that is, materials that by themselves are show an ability to manipulate their magnetization with the application of an electric field), a number of composite systems have also been investigated. In such systems, a piezoelectric material is combined with a magnetoelastic material in order to allow for the effect of a magnetoelastic multiferroic via the mediation of a common state variable (in this case, strain). A schematic diagram of such a system implemented via thin-film deposition can be seen in Figure 1.2.

Beyond memory applications[46, 45, 63, 44, 103], the potential for high-efficiency, voltage-controlled magnetism has also drawn interest as a potential mechanism to enable extremely electrically small antennas ($l < \lambda/100$).[119, 120, 1]. This was the initial motivation for the

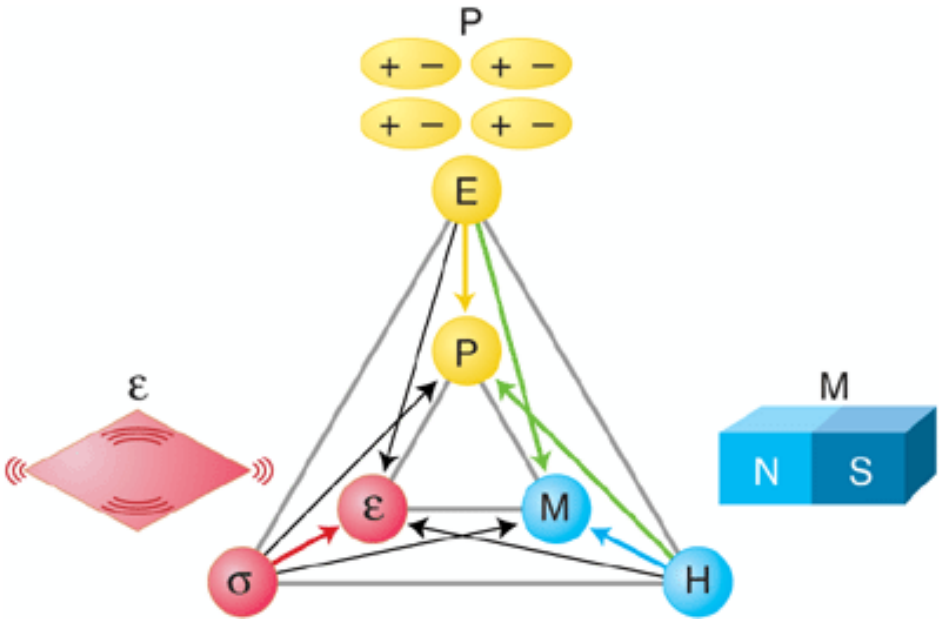

Figure 1.1: Relation between electrical, mechanical, and magnetic degrees of freedom in a multiferroic material. Such materials show multiple types of ferroic ordering (ie. ferroelectricity and ferromagnetism) and show a coupling between their ferroic orders (ie. switching the polarization may switch the magnetization). Reproduced from [98].

investigation of the device applications of acoustically driven ferromagnetic resonance, as an efficient mechanism for driving magnetic dipoles into resonance could be used to enable a GHz-range antenna whose radiation properties were largely independent of size.

In our investigations of ADFMR as a potential driving mechanism for antenna applications, we were surprised by the extremely large absorption efficiency observed in these devices, even at low driving frequencies[58]. This led to the exploration of a number of other applications. One such application was magnetic sensing - due to the linear nature of the phenomenon and the extremely steep absorption when entering / leaving resonance, it was determined that ADFMR devices could be extremely sensitive room-temperature magnetometers. Moreover, due to their preferential sensitivity along the axis 45° from the SAW propagation direction, they could be used as vector magnetometers - an application space is long overdue for a technological advance. We were also able to work with collaborators to demonstrate the use of ADFMR to drive off-resonant coupling to diamond NV centers, enabling zero-field excitation of a quantum defect at room temperature in an on-chip form factor.

This thesis describes my work on these applications of acoustically driven ferromagnetic resonance for various device applications, and is divided into eight chapters:

i *Chapter 1*: This introductory chapter discusses the motivations behind pursuing the

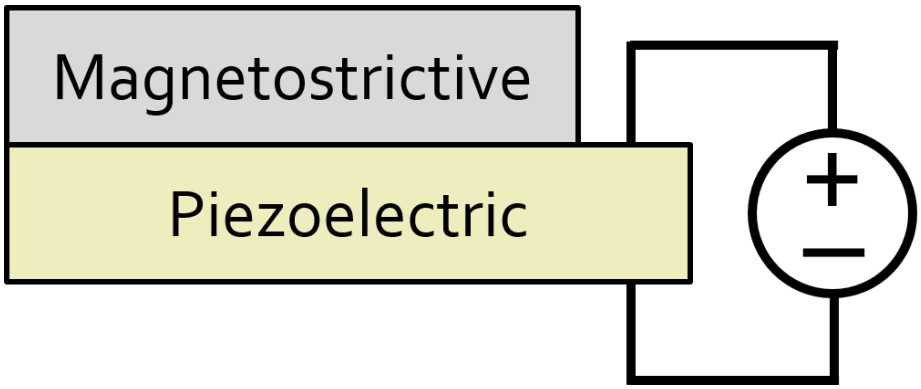

Figure 1.2: Schematic diagram of a planar composite multiferroic. In the case of this example, a magnetoelastic ferromagnet is deposited on top of a piezoelectric substrate. Applying an electric field to the substrate creates a strain that is then transferred into the magnetic thin film. This strain then induces a magnetization rotation in the ferromagnet through the effect of a strain-dependent anisotropy term in the free energy of the system. Conversely, a change in the film magnetization creates a strain in the piezoelectric substrate that can be measured as a voltage.

work presented in this thesis.

ii *Chapter 2*: The second chapter of this work provides a brief overview of the background required to understand the results presented in later chapters. It describes the phenomenon of ferromagnetic resonance, the origin of the magnetoelastic driving field, and the transducer structures used to implement acoustically driven ferromagnetic resonance (ADFMR) devices.

iii *Chapter 3*: The following chapter reports details on the experimental setup and data analysis techniques. It also includes plots of raw data from a number of measurements on ADFMR devices, including frequency, thickness, length, and power dependence studies. Comments on the importance of such measurements are also included.

iv *Chapter 4*: This chapter discusses the use of ADFMR devices as high sensitivity magnetometers, with sensitivities more than 1000x better than current solid state sensors. ADFMR magnetometers (and gradiometers) have the potential to replace the current state of the art sensors (SQUID and SERF magnetometers) in a number of critical applications.

v *Chapter 5*: The fifth chapter of this thesis focuses on work done with the TANMS (Translational Applications of Nanoscale Multiferroic Systems) ERC on applications of ADFMR (and more generally, acoustic manipulation of magnetism) for antenna applications. It includes a discussion on FMR as a mechanism for generating far-field

radiation, and includes considerations critical for developing a multiferroic antenna system.

vi *Chapter 6*: The next chapter details our work on coupling the ADFMR system to nitrogen vacancy (NV) centers in diamond. NV centers have garnered substantial interest as quantum computers, clock sources, sensors, and for many other applications. NV centers can undergo off-resonant coupling with systems undergoing FMR, and in this chapter we discuss our work with using ADFMR to drive this off-resonant excitation.

vii *Chapter 7*: The final chapter presenting new material focuses on the modeling of the ADFMR system, detailing the derivations of these models and how they were used to extract material properties. Using precise formulations for the power absorption in ADFMR has allowed us to extract the damping and magnetoelastic coefficients in these systems. Also detailed are a variety of magnetic measurements performed to extract material parameters.

viii *Chapter 8*: The last chapter summarizes the work presented in this thesis and comments on potential avenues for future research in the field of acoustically driven ferromagnetic resonance and its applications.

Chapter 2

Acoustically driven ferromagnetic resonance

Acoustically-driven ferromagnetic resonance (ADFMR) has recently emerged as an efficient method for spin-wave generation in magnetoelastic thin films.[112, 27, 111, 102, 121] Spin wave generation via ADFMR has been utilized for spin-wave spectroscopy[35], and has been proposed as a potential mechanism for enabling device applications such as spin wave-based logic[13, 12] and memory elements.[13]

ADFMR is driven by dynamic strain/stress fields and spin-wave amplitudes local to the magnetoelastic film / driving piezoelectric interface. The standard device configuration for the measurement of this phenomenon consists of an input and output interdigitated transducer (IDT) on a piezoelectric substrate, with a thin ferromagnetic film deposited between the two. A schematic diagram of this system can be seen in Figure 2.1. Surface acoustic waves (SAWs) generated by an AC voltage incident on the input IDT travel through the substrate, where some of the SAW power is absorbed by the ferromagnet, driving it into resonance. The remaining SAW power continues to propagate through the substrate until it reaches the output IDT, where it is converted back into an AC voltage. The magnitude of absorption by the magnetic film is used to characterize the effect.

The remaining portion of this chapter is intended to give a brief background on ferromagnetic resonance and how the time-varying strain created by a traveling surface acoustic wave is capable of exciting this effect in a magnetostrictive ferromagnet. Section 2.1 describes the basics of ferromagnetic resonance, Section 2.2 describes how a time-varying strain can create the effective RF magnetic field required to drive FMR, and Section 2.3 describes how the surface acoustic wave devices used to generate the strain waves operate and how they were optimized.

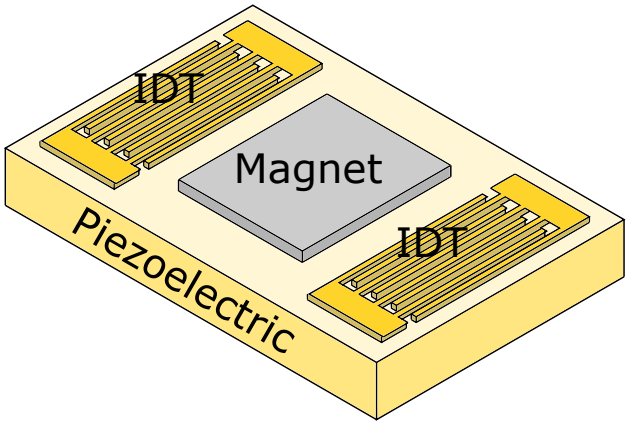

Figure 2.1: Schematic diagram of an exemplary ADFMR device. An input and output IDT are deposited on a piezoelectric substrate, and then a magnetoelastic ferromagnetic film is deposited between the two. By measuring the attenuation of the transmission between the two IDTs, it is possible to quantify the absorption of the traveling SAW by the ferromagnetic film.

2.1 Ferromagnetic resonance

Ferromagnetic resonance (FMR) has been historically utilized to extract the magnetic properties of materials. This technique relies on characterizing the absorption of RF power by a magnetic sample as a function of an external bias field H. By using a macrospin approximation, we can describe this technique as follows. When the external field H is applied to a magnetic sample, this causes the sample magnetization to precess around the applied field until damping causes the film to eventually align with the applied field. This precessional behavior can be described by the Landau Lifshitz Gilbert equation shown in Eq. 2.1[33].

$$\frac{\partial \mathbf{M}}{\partial t} = -\gamma \mathbf{M} \times \mathbf{H_{eff}} - \lambda \mathbf{M} \times (\mathbf{M} \times \mathbf{H_{eff}}) \tag{2.1}$$

Where $\mathbf{M}$ is the sample magnetization, $\mathbf{H_{eff}}$ is the effective applied magnetic field, γ is the gyromagnetic ratio and λ is a phenomenological damping parameter that can be written as:

$$\lambda = \alpha \frac{\gamma}{M_s} \tag{2.2}$$

Where α is the Gilbert damping parameter and M_s is the saturation magnetization of the film. A graphical representation of this behavior can be seen in Figure 2.2.

In order to maintain the precession that is the hallmark of ferromagnetic resonance, the constant application of an RF 'tickle' magnetic field is required to counteract the damping of the sample magnetization. In conventional FMR experiments, this tickle field is provided either by the electromagnetic field inside a resonant cavity[31], or by the Oerstead field

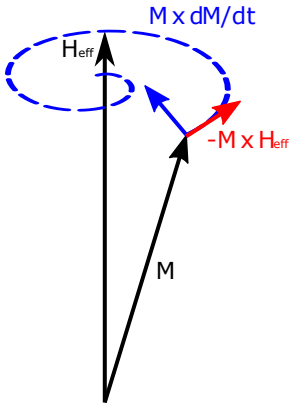

Figure 2.2: Graphical illustration of magnetic precession in the presence of an external magnetic field H_{eff}. The behavior of the magnetization is dictated by a term orthogonal to the direction of precession ($-\mathbf{M} \times \mathbf{H_{eff}}$) and a damping term that drives the magnetization towards the applied magnetic field direction($\mathbf{M} \times \frac{\partial \mathbf{M}}{\partial t}$).

generated by an RF current flowing through a stripline.[52] More recent work has explored the use of spin transfer torque[48] and the spin hall effect[64] to achieve the same goal, leveraging these effects to enable the generation of larger field magnitudes at lower input power levels.

FMR experiments are traditionally performed by measuring RF power absorption by a magnetic sample located either in a resonant cavity [31] or on a stripline structure.[52] In these techniques, the change in power absorption on and off of resonance is usually on the order at most a few percent, requiring a sensitive measurement apparatus in order to observe a strong signal above the noise. An equation for the amount of power absorbed by a magnet undergoing ferromagnetic resonance can be found in Eq. 2.3. The reason for low absorption in traditionally-excited FMR setups is that the power absorption depends on the effective excitation field. Using a current to generate an Oerstead field (as is the basis of these techniques) is extremely inefficient, so that only a small portion of the transmitted power is actually converted into an oscillating magnetic field. A schematic diagram of FMR characterization setups of both of these types can be found in Fig. 2.3.

$$P_{abs} = \frac{\mu_0 \omega}{2} Im\{\chi\} \int_V |\mathbf{H_{eff}}|^2 dV \tag{2.3}$$

An example of the extracted permeability (χ) can be found in Figure 2.4. As can be seen, the permeability has a maximum at the ferromagnetic resonance frequency (and it's derivative goes through a zero crossing there). The linewidth of the resonance is given by the distance between the maximum and minimum of the derivative (or the full-width half-max of the permeability). The resonant frequency for a given applied field (and thus the resonant

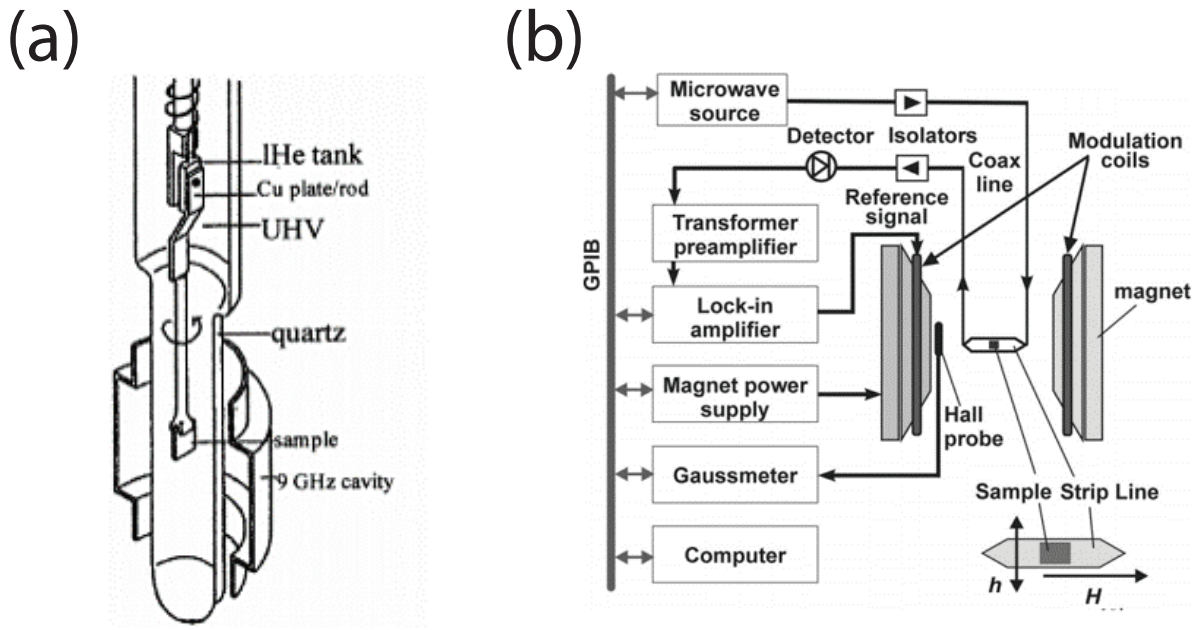

Figure 2.3: (a) Diagram showing a traditional setup for high-sensitivity cavity FMR experiments, showing a rotatable sample suspended in a resonant cavity tuned to 9 GHz. This implementation also has the sample attached to a coldfinger and suspended in high vacuum to allow for cryogenic refrigeration. RF power is applied to the resonant cavity, and the power absorbed by the sample is measured as a function of applied magnetic field. This figure was reproduced from [31]. (b) Schematic showing a standard stripline FMR setup. An RF excitation is passed through a stripline with a sample attached to it. The absorption of RF power as a function of applied magnetic field is measured in order to obtain a measurement of the sample permeability. In this setup, a set of modulation coils allow for a lock-in measurement of the derivative of this signal $\frac{\partial \chi}{\partial H}$ to help reduce measurement noise. This figure was reproduced from [52].

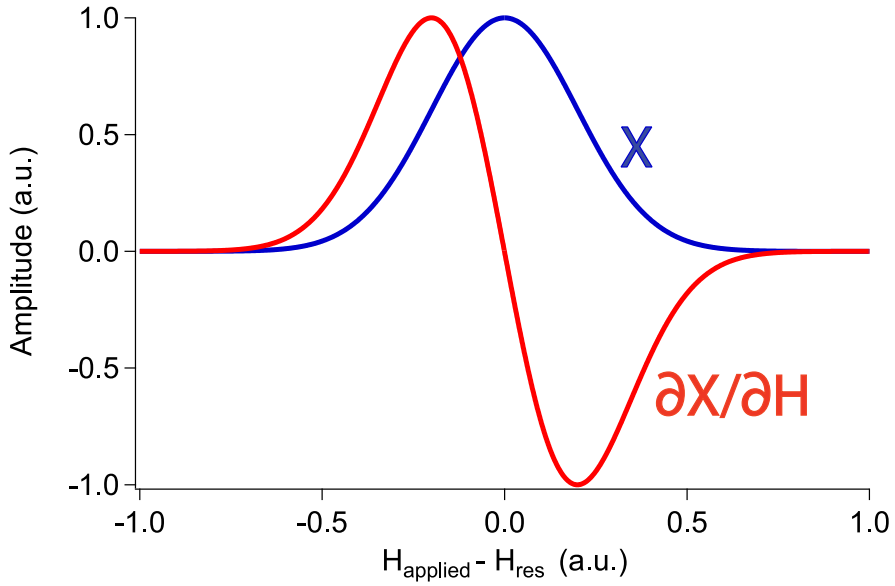

Figure 2.4: Idealized plot of normalized extracted χ (blue) and $\frac{\partial \chi}{\partial H}$ (red). χ reaches a maximum at the resonance field H_{res} for a given drive frequency, while $\frac{\partial \chi}{\partial H}$ has a zero crossing. The distance between the maximum and minimum of $\frac{\partial \chi}{\partial H}$ (the full-width half-maximum (FWHM) of χ) is referred to as the linewidth of the magnetic sample. The frequency dependence of the linewidth allows for the extraction of the Gilbert damping coefficient as shown in Equation 2.5.

field for a given excitation frequency) is given by the Kittel formula as shown in Equation 2.4. [53] The FMR linewidth can be used to extract the Gilbert damping parameter for the film, which is an indication of how quickly magnetic excitations in the film relax. The linewidth has a linear dependence on frequency, which can be used to extract the damping parameter as shown in Equation 2.5. [52]

$$f_0 = \frac{\gamma}{2\pi}\sqrt{B_{eff}(B_{eff} + \mu_0 M_s)} \tag{2.4}$$

$$\Delta H = \Delta H_0 + \frac{4\pi\alpha f}{|\gamma|} \tag{2.5}$$

2.2 Magnetoelastic excitation

The tickle field used to drive FMR in acoustically driven ferromagnetic resonance is unique in that it does not require the application of a charge current, as is standard in all previously

discussed methods. Instead, the tickle field is generated by the interaction of the time-varying strain (created by the traveling surface acoustic wave) and the magnetoelastic film. This method of excitation is extremely efficient - at 2 GHz, a 1 μW excitation power can create an effective tickle field in a nickel film of ≈ 1.25 Oerstead over a width of 100 μm. Generating the same field by flowing RF current through a 50 Ω stripline with a nominal thickness of 35 microns (standard thickness for 1 oz copper plating on PCBs), alternatively, would require ≈ 35 mW.

The effective magnetic field caused by the surface acoustic waves in this system is calculated by using the method of Dreher et. al.[27]. We define a new reference frame (1,2,3), where $\mathbf{m}$ is in the direction of the 3-axis, and the 2-axis is in the film plane. We allow small deviations from the equilibrium direction, so the magnetization can be written as:

$$\mathbf{m} = \underbrace{\begin{pmatrix} 0 \\ 0 \\ 1 \end{pmatrix}}_{m_0} + \begin{pmatrix} m_1 \\ m_2 \\ 0 \end{pmatrix} + O(m_1^2, m_2^2) \tag{2.6}$$

The transformation matrix between (x,y,z) and (1,2,3) is given below.

$$\begin{pmatrix} m_x \\ m_y \\ m_z \end{pmatrix} = \begin{pmatrix} \cos(\theta_0)\cos(\phi_0) & -\sin(\phi_0) & \sin(\theta_0)\cos(\phi_0) \\ \cos(\theta_0)\sin(\phi_0) & \cos(\phi_0) & \sin(\theta_0)\sin(\phi_0) \\ -\sin(\theta_0) & 0 & \cos(\theta_0) \end{pmatrix} \begin{pmatrix} m_1 \\ m_2 \\ m_3 \end{pmatrix}$$

Where θ_0 is the angle between +z and m_0, and ϕ_0 is the angle between the +x axis and m_0 The effective field can then be calculated by solving:

$$\mu_0 \mathbf{H_{eff}} = -\nabla_{\mathbf{m}} G^{tot} \tag{2.7}$$

Where G^{tot} is the total free-enthalpy density of the nickel film, $-\nabla_{\mathbf{m}} = (\partial_{m1}, \partial_{m2}, \partial_{m3})$ is the vector differential operator with respect to $\mathbf{m}$, and $\mathbf{H_{eff}}$ is the effective field seen by the magnet. Here we focus only on the dynamic, magnetoelastic component of the free-enthalpy density[14]:

$$\begin{aligned} G^d = b_1[\varepsilon_{xx}(x,t)m_x^2 + \varepsilon_{yy}(x,t)m_y^2 + \varepsilon_{zz}(x,t)m_z^2] \\ +2b_2[\varepsilon_{xy}(x,t)m_x m_y + \varepsilon_{xz}(x,t)m_x m_z + \varepsilon_{yz}(x,t)m_y m_z] \end{aligned} \tag{2.8}$$

We now insert this expression for G^d into equation 2.7 and evaluate at $\mathbf{m_0}$ to obtain $\mathbf{H_{eff}^d}$ in the $\mathbf{m_1}$ and $\mathbf{m_2}$ directions:

$$\begin{aligned}\mu_0 H^d_{eff,1} = -\frac{\partial G^d}{\partial m_1}|_{m_0} = \\ 2b_1\cos(\theta_0)\sin(\theta_0)[\cos(\phi_0)^2\varepsilon_{xx} + \sin(\phi_0)^2\varepsilon_{yy} - \varepsilon_{zz}] \\ +2b_2[\cos(\theta_0)^2(\cos(\phi_0)\varepsilon_{xz} + \sin(\phi_0)\varepsilon_{yz}) \\ -\sin(\theta_0)^2(\cos(\phi_0)\varepsilon_{xz} + \sin(\phi_0)\varepsilon_{yz}) \\ +\cos(\theta_0)\sin(\theta_0)\sin(2\phi_0)\varepsilon_{xy}]\end{aligned} \tag{2.9}$$

$$\begin{aligned}\mu_0 H^d_{eff,2} = -\frac{\partial G^d}{\partial m_2}|_{m_0} = \\ 2b_1\cos(\phi_0)\sin(\phi_0)\sin(\theta_0)[\varepsilon_{yy} - \varepsilon_{xx}] \\ +2b_2[\cos(\theta_0)(\cos(\phi_0)\varepsilon_{yz} - \sin(\phi_0)\varepsilon_{xz}) \\ +\sin(\theta_0)\cos(2\phi_0)\varepsilon_{xy}]\end{aligned} \tag{2.10}$$

These magnetoelastic driving fields are further used in a series of calculations in Section 7.3 to extract the magnetoelastic coupling coefficient for the films measured in this thesis. An understanding of the source of these fields is critical to the analysis of the ADFMR effect, as they enforce a distinct angular dependence on the measured absorption that distinctly identifies the acoustic driving mechanism from traditional current-based excitations.

2.3 Surface acoustic wave devices

While acoustically driven ferromagnetic resonance could theoretically be implemented by coupling a magnetoelastic ferromagnet to any source of RF strain, applications of this technique thus far have relied on a surface acoustic wave delay line structure. [112, 27, 111, 102, 35, 58] SAW delay lines have been under development since the 1960s[96], and are used for applications as varied as RF signal filtering[99], gas sensing[22], and biological sensing[59]. By designing ADFMR devices whose core RF transmission characteristics are based on SAW delay lines, we are capable of leveraging decades of research and design experience in order to reduce the workload required to fabricate well-matched and efficient devices at the relevant RF frequencies of 100's of MHz to a few GHz.

SAW delay lines operate by using an input RF signal to generate surface acoustic waves in a piezoelectric substrate by using a periodic electrode structure known as an interdigitated transducer. This transducer is a periodic array of ground and signal electrodes spaced such that the periodicity is equal to the wavelength of the SAW at their center operating frequency. This wavelength is obtained by dividing the SAW propagation speed in the substrate material (usually a few thousand meters per second) by the target operating frequency. The number of periods in the structure determines the bandwidth of the IDT structure, with more fingers

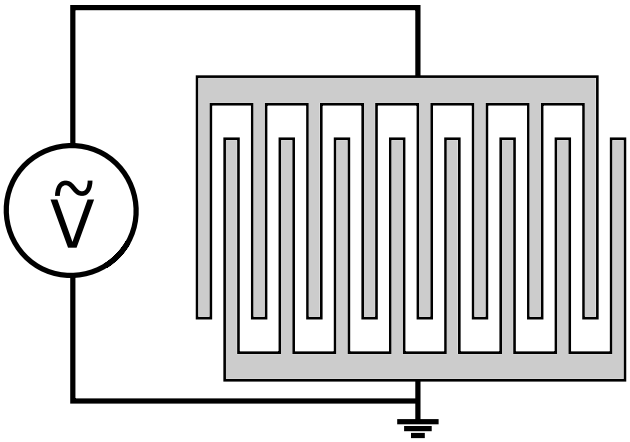

Figure 2.5: Schematic illustration of an interdigitated transducer structure used to generate and receive surface acoustic waves. One set of electrodes are usually grounded, while the other set is connected to an RF signal source (pictured) or a spectrum analyzer or other measurement system.

resulting in a smaller bandwidth figure.[96] A schematic drawing of such an IDT can be seen in Figure 2.5.

The generation of the surface acoustic waves is caused by constructive interference of the time-varying strain within the IDT. When a voltage is applied across the IDT electrodes, the piezoelectric substrate is strained between the electrode pairs. Normally, such a strain would remain localized to the electrode structure, but by carefully timing the voltage excitation such that the propagating strain constructively interferes during each cycle, it is possible to generate a propagating wavefront that is emitted from both sides of the electrode array and travels along the surface of the substrate. This emission has a peak at the fundamental design frequency (determined by the SAW propagation speed in the material divided by the IDT periodicity), but notable emission also can occur at harmonics of this fundamental frequency where the constructive interference criteria are also met. Due to the crystalline properties of the substrate, these acoustic excitations experience very little loss. In lithium niobate, for example, SAW attenuation is only $\approx$ 2 dB / cm at an excitation frequency of 2 GHz, and reduces further as the frequency is lowered (0.6 dB / cm at 500 MHz).[93] These favorable attenuation properties, coupled with the easy ability to tune bandwidth (and thus Q-factor) have resulted in large industrial interest and adoption for filter applications.

On the other side of the device, an identical IDT structure is used to detect the incoming surface acoustic wave. As the strain travels through the substrate material, the spatially-varying strain generates a corresponding voltage due to distortions of the piezoelectric crystal. This voltage can be read out by the periodic electrodes on the receiving end of the device to recover the input signal. Using reflector structures to ensure that all SAW signals are directed in one direction (as opposed to the default bidirectional case shown in Figure 2.5), lithium niobate delay line structures have reached insertion loss figures of as low as 1.0

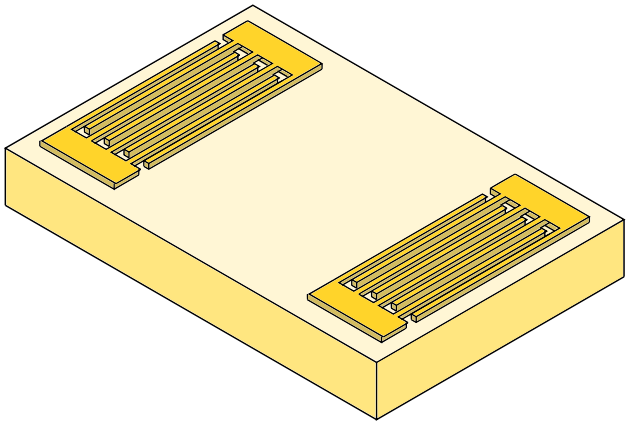

Figure 2.6: Schematic illustration of a generic SAW delay line structure. The delay line is fabricated on a crystalline piezoelectric structure to allow for the generation and propagation of the surface acoustic waves. Input and output interdigitated transducers are used to generate and measure the SAWs.

dB.[118] A schematic illustration of a complete delay line structure can be seen in Figure 2.6.

A number of more complex fabrication techniques can be used to improve the efficiency of IDT structures. For example, to reduce loss from the bidirectional nature of a simple interdigital transducer, reflector structures can be used to ensure that the emitted acoustic waves travel only in one direction, reducing the insertion losses of delay line devices by 3 dB. [95, 20] In addition, multi-electrode designs can be used to increase performance when driving SAW devices at harmonics of the fundamental frequency. [42, 69] The wealth of existing literature on such device enhancements was a critical factor in deciding to use the SAW structure for these experiments. In this work, we utilize a double-electrode structure to enhance harmonic performance, as the ability to measure a range of frequencies on a single device is critical for a thorough characterization of the ADFMR effect.

A transmission measurement from 50 MHz to 3 GHz of a fabricated ADFMR structure at 0 field can be seen in Figure 2.7. The inset in the bottom-right corner of this figure shows a schematic diagram of the IDT structure, which is of a double-finger design to enhance operation at higher excitation frequencies. This measurement was taken with a continuous-wave excitation by a vector network analyzer, and clearly shows transmission maxima at the first three odd harmonics (1st, 3rd and 5th) of the IDT fundamental frequency.

Time gating

One major problem with measuring transmission between a pair of interdigitated transducers operating at high harmonics of the fundamental frequency is the growing influence of electromagnetic interference. Operating IDTs at high harmonics substantially increases the

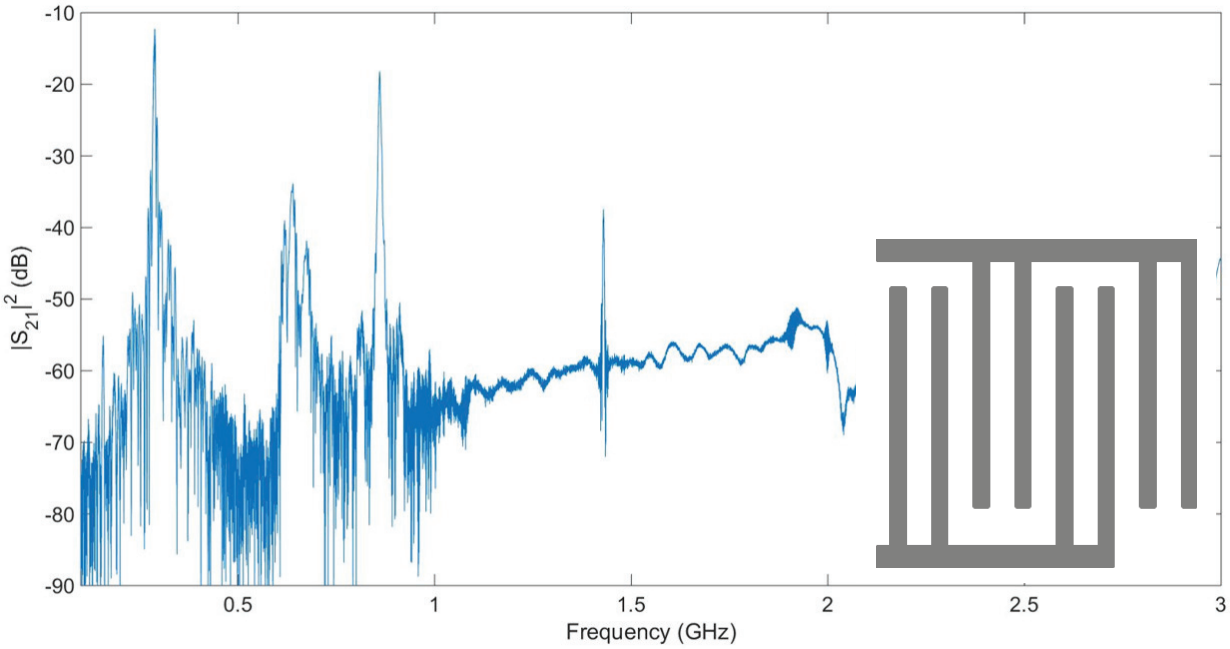

Figure 2.7: Transmission (S_{21}) measurement between input and output IDTs plotted as a function of frequency for an exemplary surface acoustic wave delay line designed for a fundamental frequency of $\approx$ 287 MHz. The first (287 MHz), third (861 MHz) and fifth (1430 MHz) harmonics can easily be observed, but higher order modes are drowned out by electromagnetic interference. The double finger IDT structure used in these devices is shown in the inset.

insertion loss of the devices, which results in a transmitted SAW signal that is substantially diminished. While this could normally be corrected for by the use of sensitive measurement equipment, there is also non-SAW coupling between interdigitated transducers that begins to dominate the signal.

In addition to generating SAWs, the IDT electrodes also radiate and absorb a small portion of the incident RF power as electromagnetic radiation. This radiation is generated by any time-varying charge current, but is generally very small in our IDT structures as their design is such that they are not resonant (and thus act as poor antennas) at the selected excitation frequencies. Since the electrodes are far from resonance, the radiation emitted by them is very broad-band, with a roughly constant amplitude over the excitation frequencies of interest.

This combination of decreasing transmitted SAW power with a constant transmitted electromagnetic radiation power creates a situation in which, after a certain frequency threshold is passed, the electromagnetic component of the transmitted signal dominates. As magnetoelastic excitation of the ferromagnetic film in these measurements nominally does not modulate the electromagnetic signal at all, this electromagnetic signal only serves to add

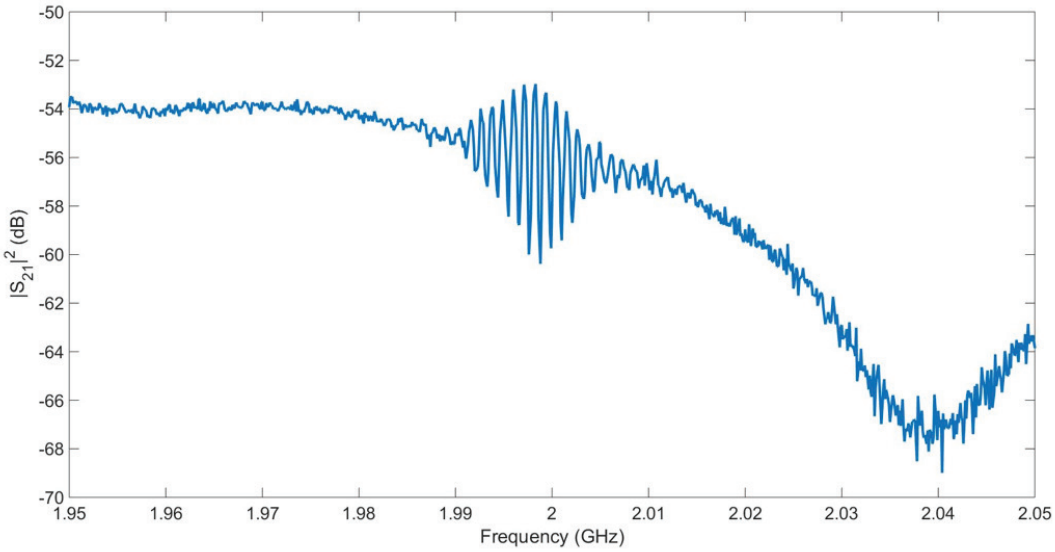

Figure 2.8: An un-gated transmision signal between two IDTs measured in the frequency domain. Note the extremely small amplitude and interference fringes between the surface acoustic wave and the electromagnetic wave. This extremely small signal is due to the fact that the IDTs are being driven at their 7th harmonic.

noise into the measurement of the field-dependent SAW attenuation. This interference can be quite substantial, to the point where the change in the SAW signal at high harmonics can be so comparatively small that it is unmeasurable.

One method that can be utilized to minimize this harmful interference is to leverage the vastly different propagation speeds between the elastic and electromagnetic waves. Since one wave travels at the speed of light ($\approx 3 * 10^8$ m/s) and the other travels at the speed of sound in the piezoelectric material ($\approx$ 3500 m/s), there is a very measurable difference in arrival times of the two waves at the output transducer if the signal on the input transducer is pulsed. In a 2.5 mm delay line on lithium niobate, for example, this time difference is approximately 700 nanoseconds.

As a result, the signal can be gated in the time-domain to ensure that only the output signal induced by the traveling SAW is measured. This can be done by taking a frequency-domain sweep with sufficient resolution using a continuous wave excitation source (as in a VNA, for example) as is shown in Figure 2.7.[79] A zoomed-in view of the extremely weak transmission peak seen at $\approx$ 2 GHz can be found in Figure 2.8. The interference fringes from the phase difference between the acoustic and electromagnetic waves impinging on the output IDT can be clearly seen. If one takes the inverse fourier transform of this signal to transform it into the time domain, a set of clear peaks can be observed - one at t$\approx$0 (the electromagnetic wave) and one at t$\approx$700 ns (the acoustic wave). By 'gating' this time domain

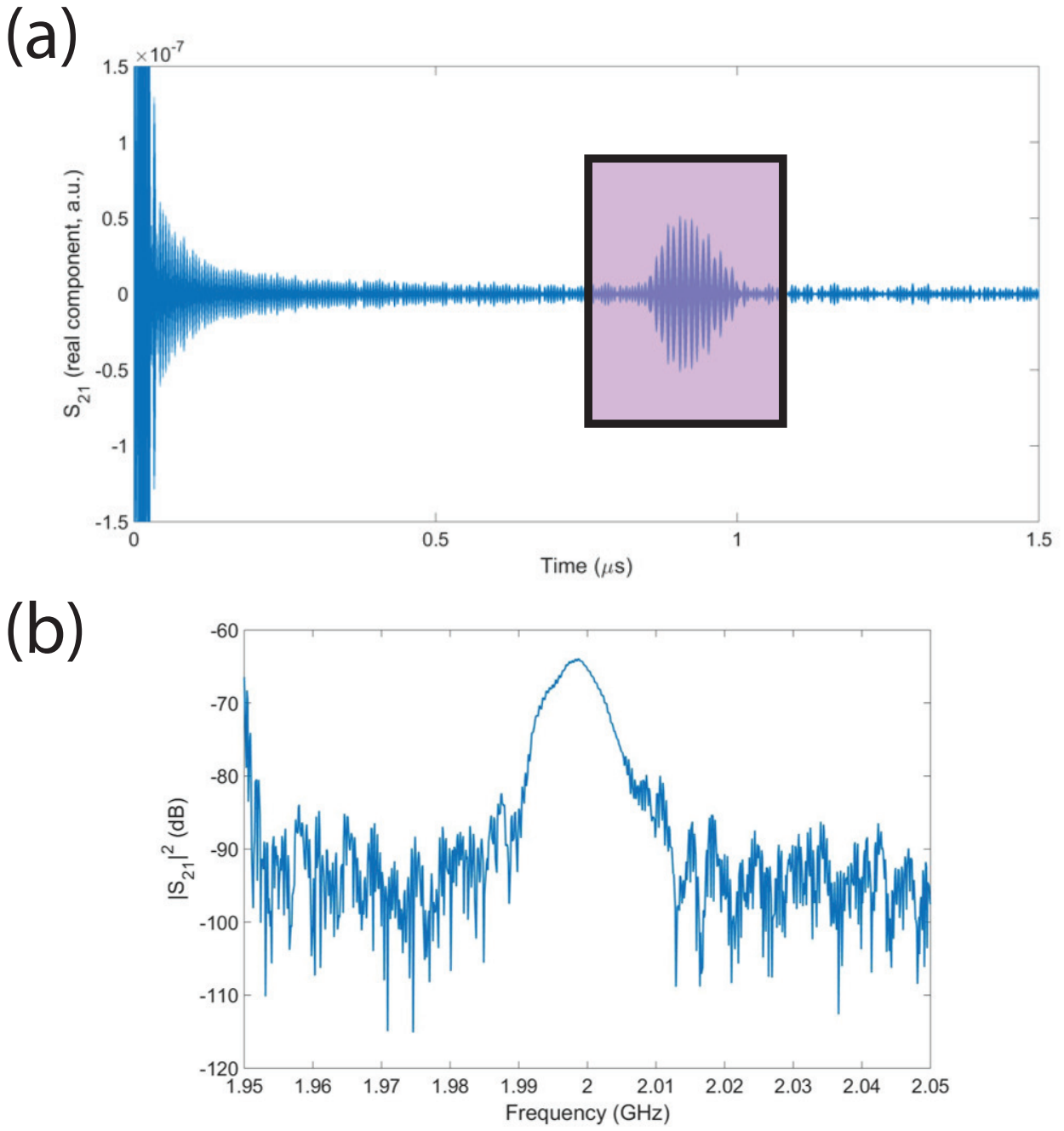

Figure 2.9: Illustration of the time-gating procedure.(a) is the same signal as shown in Figure 2.8 in the time domain, clearly showing a peak due to electromagnetic waves near t=0, and a second peak from SAW transmission at t≈800 ns. The purple box indicates the region that was preserved after time gating - all other points were set to 0. (b) is the signal re-plotted in the frequency domain after time gating, showing a substantial reduction of background signal and visible interference fringes, and thus an enhanced visibility of the SAW peak.

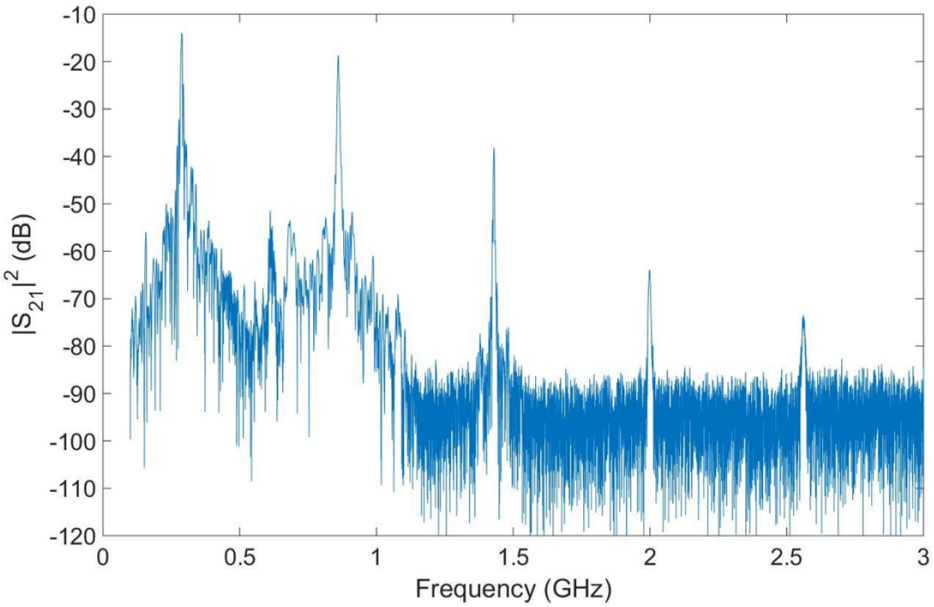

Figure 2.10: A time-gated transmission (S_{21}) measurement between input and output IDTs plotted as a function of frequency for the same device as shown in Figure 2.7 above. The first (287 MHz), third (861 MHz), fifth (1430 MHz), seventh (2000 MHz), and ninth (2565 MHz) harmonics are easily visible, as the background noise level has been reduced from ≈ -60 dB to ≈ -90 dB.

signal, one can reject the electromagnetic wave component of the signal, and measure only the acoustic component. This time-domain conversion and gating can be seen in Figure 2.9(a). Finally, the signal is then converted back into the frequency domain, where a much clearer SAW peak (and much reduced broadband signal level) can be observed, as shown in Figure 2.9)(c). A measurement of the same device as in Figure 2.7 with time gating applied is shown in Figure 2.10. A clear reduction of the broadband background signal can be observed, allowing for the measurement of the higher-order harmonic measurement peaks with transmission levels as low as -75 dB.

An alternative method for time gating of SAW delay line signals is to gate directly in the time domain by applying the excitation waveform as a short pulse (as opposed to as a continuous wave), and then measuring only during the period of time corresponding to the pulse duration + transit time.[60] We utilize this hardware method in our experiments, as it allows for much faster and less computationally intense noise rejection. A ≈700 ns pulse is applied using a function generator at a repetition rate of 500 kHz, and is measured after a 800 ns delay by a spectrum analyzer with hardware time gating capability. This allows us to take time-gated data much faster than if we were required to do a full frequency sweep and perform an IFFT and FFT on the data for each data point. An image of the time gating menu seen in the spectrum analyzer for a sample 2 GHz excitation can be seen in Figure 2.11. The electromagnetic and SAW components of the wave are clearly marked, with the

Figure 2.11: Image of spectrum analyzer screen while performing a hardware time gating measurement. The electromagnetic wave (red box) appears with a time delay of ≈ 0, while the SAW (white box) can be seen after a delay of ≈ 800 ns. The pulse width is 700 ns.

electromagnetic wave component having a substantially larger amplitude due to the high harmonic of the excitation

Optimization of SAW delay lines

In order to obtain low insertion loss (high transmission) between the interdigitated transducers, it was necessary to optimize the SAW delay lines so they would be matched to the input and output RF lines (with a characteristic impedance of 50 Ω). This was done by adjusting the width of the transducers so that they had an impedance as close as possible to 50 Ω in order to optimize the power transfer between the measurement setup and the ADFMR devices. In addition, values were calculated for series matching inductors that would eliminate the reactive component of the IDT impedance. All calculations were done by following the methods and equations in [114].

The width of the optimized finger overlap in the IDT structures (the IDT aperture) is given by:

$$W_a = \frac{1}{50\Omega}\frac{1}{2f_0 C_s N_p} Re\left(\frac{1}{4k^2 N_p + i\pi}\right) \tag{2.11}$$

Where f_0 is the center frequency, C_s is the capacitance per finger pair per meter, N_p

is the number of finger pairs, k is the piezoelectric coefficient (≈ 0.22 for YZ cut lithium niobate), and i is $\sqrt{(}-1)$.

The value for the series matching inductor is given by:

$$L = \frac{1}{(2\pi f_0)^2 * C_T} \tag{2.12}$$

Where C_T is the total IDT capacitance, and is given by:

$$C_T = N_p C_s W_a \tag{2.13}$$

The total insertion loss as a function of frequency for the devices can be calculated by:

$$IL(f) = -10\log_{10}\left[\frac{2G_a(f)50\Omega}{(1+G_a(f)50\Omega)^2 + \left[50\Omega\,(2\pi f C_T + B_a(f))^2\right]}\right] \tag{2.14}$$

Where $G_a(f)$ is the radiation conductance, and is given by:

$$G_a(f) = 8k^2 C_s W_a f_0 N_p^2 \left(\frac{\sin(2x(f)) - 2x(f)}{2x(f)^2}\right) \tag{2.15}$$

$B_a(f)$ is the acoustic susceptance, and is given by:

$$B_a(f) = G_a(f_0)\frac{\sin(2x(f)) - 2x(f)}{2x(f)^2} \tag{2.16}$$

And $x(f)$ is given by:

$$x(f) = \begin{cases} 0 & f = f_0 \\ N_p * \pi * \left(\dfrac{f - f_0}{f_0}\right) & f \neq f_0 \end{cases} \tag{2.17}$$

When the IDT width is properly optimized to approximate 50 Ω, the insertion loss of the SAW delay line structures can be substantially reduced. Figure 2.12 illustrates a comparison of the measured insertion loss of an unmatched device (500 μm aperture) versus a properly matched device (160 μm aperture) across a variety of frequencies. As can be seen, insertion loss in the properly sized device is much lower, especially at high harmonics. The nature of the impedance matching in these devices only allows for the impedance to be precisely matched at one frequency (chosen here to be the fundamental frequency), but it can clearly be seen that even optimizing only the fundamental response shows great improvement across the entire range of harmonics. It is also important to keep in mind that since all of the interdigitated transducers used in this work are bidirectional, the minimum possible insertion loss (regardless of matching, IDT spacing, or material properties) is 6 dB.

The reduction of insertion loss could be further enhanced by including series inductors to reduce the reactive part of the IDT impedance. This was not done in these experiments as the ability to measure across a broad range of frequencies was desired, and adding a series

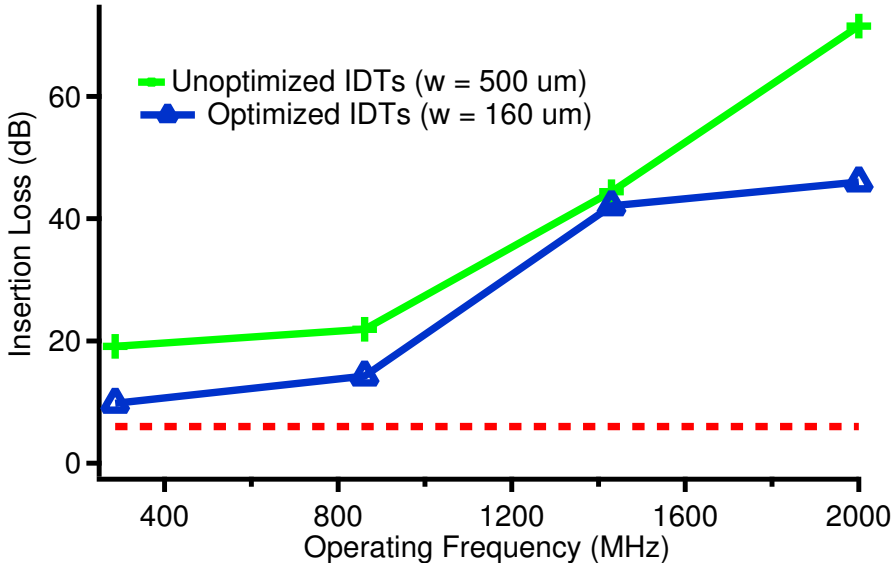

Figure 2.12: Comparison of optimized (blue) and unoptimized (green) IDTs operating across a range of frequencies. The optimized transducers show a clearly reduced insertion loss compared to the unoptimized devices, especially at high frequencies. Horizontal red line indicates the minimum possible insertion loss (6 dB) for a delay line using bidirectional transducers.

inductor would necessarily reduce the bandwidth of the delay lines, impeding our ability to measure across the range of the 1st to 9th harmonic.

Chapter 3

Power dependence of acoustically driven ferromagnetic resonance

As interest in leveraging Acoustically Driven Ferromagnetic Resonance for applications develops within the research community, it is important to quantitatively examine how the effect can be tuned to fit the need of a variety of potential devices. Toward this goal, we have examined how changes in excitation power, excitation frequency, and lateral ferromagnet dimensions effect the absorption in these devices. We find that ADFMR behaves much like traditionally excited FMR with regards to excitation power and frequency: absorption is entirely linear with power, and absorption increases with increased frequency. A study of the length dependence of these films shows an exponential dependence of power absorption on film length.

Section 3.1 describes the sample fabrication techniques used to create the ADFMR devices considered in this thesis. Section 3.2 describes the measurement setup used to take all measurements shown later in this chapter. Finally, section 3.3 compiles the experimental data collected on the measured ADFMR devices as a function of excitation frequency, excitation power, element length, and element thickness.

3.1 Sample fabrication

ADFMR devices were fabricated using multi-step optical lithography on Y-cut lithium niobate substrates. For these devices, a double-electrode IDT design was chosen due to its ability to effectively excite SAWs even at high harmonics of the fundamental frequency.[71] The double-electrode design reduces destructive interference caused by reflections within the IDT when operating at higher-order modes by replacing a structure of alternating signal and ground electrodes with one where each signal (and ground) electrode is replaced by a pair of electrodes with a gap between them. The IDTs were aligned so that the direction of propagation of the SAWs would be along the Z axis of the lithium niobate samples which allowed for all devices to operate the same fundamental frequency and with a consistent

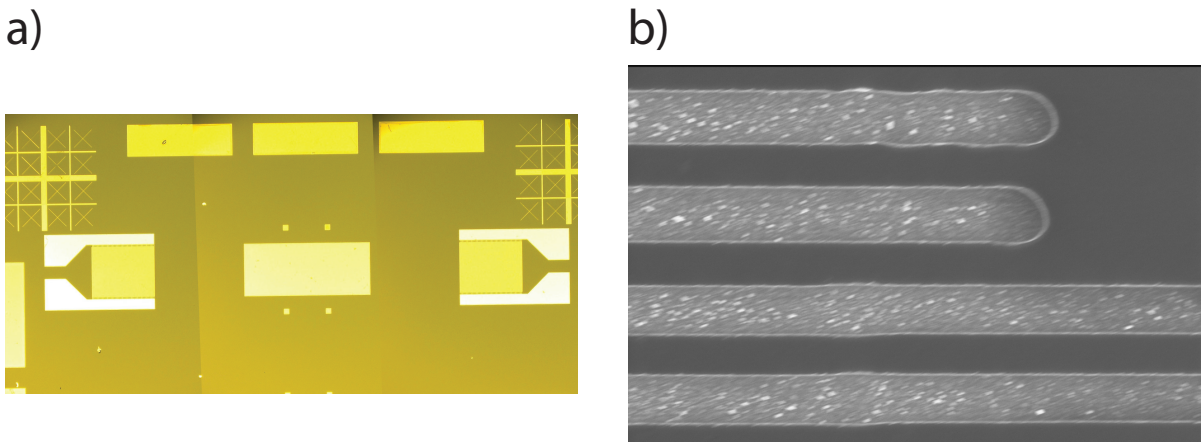

Figure 3.1: (a) Optical micrograph of a device. The center magnetic element has dimensions of 1.2 x 0.5 mm, and the two IDTs have a center-to-center spacing of 3.5 mm. (b) SEM image showing a zoomed in region of one of the double-electrode IDTs pictured in (a). The IDTs used in these devices have a finger width of approximately 1.6 μm, and a finger spacing of approximately 1.4 μm, which aligns closely with the nominal metalization ratio of 50%. The periodicity of the structure is 12 μm, which results in a fundamental frequency of $\approx$290 MHz. The width of the IDTs is 500 μm.

SAW mode.

After IDT patterning was performed, 70 nm of aluminum was deposited via thermal evaporation, and liftoff was performed to create the contacts. A second photolithography step (with alignment) was performed to define the nickel regions, which had a constant width of 500 μm and a length of 100, 300, 600, or 1200 μm. The nickel was then deposited via electron beam evaporation and lifted off, with a thicknesses between 10 and 50 nm (depending on the device) and with a thin gold capping layer (deposited in-situ on top of the nickel with electron beam evaporation). Optical and SEM images of a sample device can be found in Figure 3.1. Multiple such devices were deposited on each substrate, allowing for a comparison of the effects of magnetic element size while ensuring that the properties of the evaporated nickel film were consistent across all measured devices for a given nickel thickness.

3.2 Experimental setup

Once fabricated, these devices were wirebonded to a custom-built PCB sample holder that was designed to allow for easy SMA connections to be made to the IDTs. An image of such a sample holder with a mounted device can be found in the leftmost panel of Figure 3.2. The sample holder was then connected to a custom rotation stage with an attached shaft

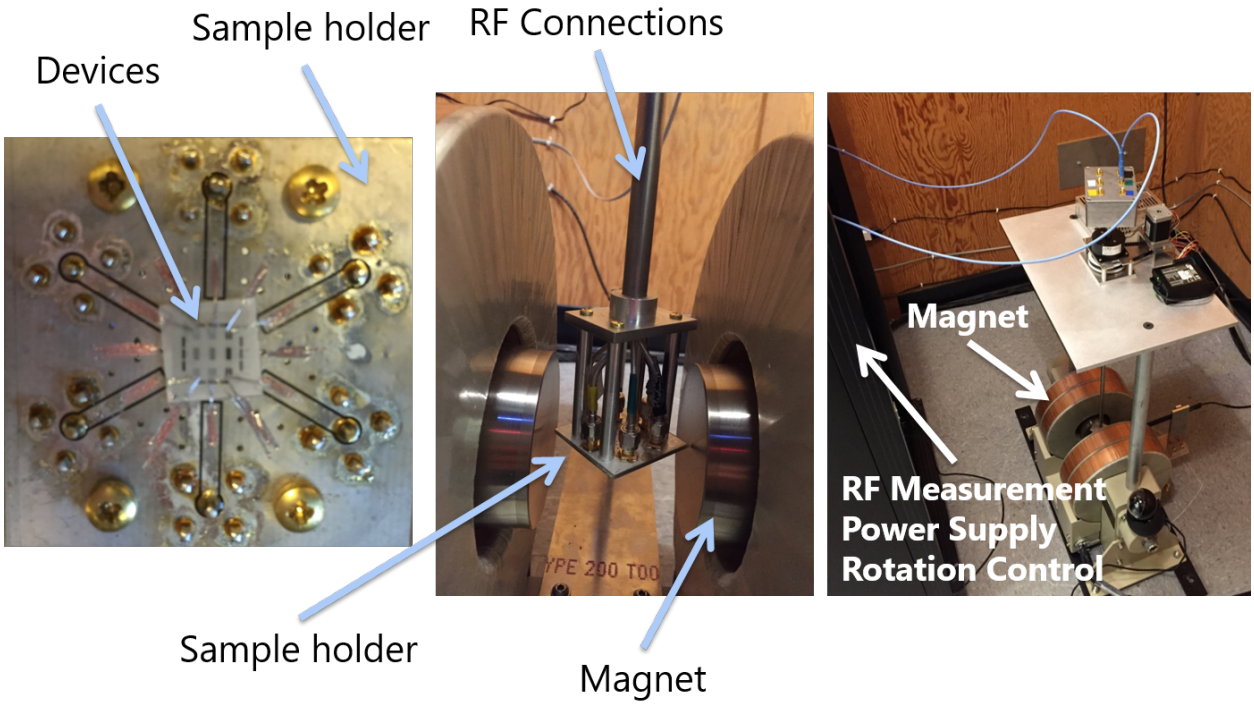

Figure 3.2: Labeled pictures of the ADFMR measurement setup. (Left) Custom-built PCB sample holder used for ADFMR measurement, with a sample mounted and bonded in the center. Each of the six traces on the sample holder leads to the signal line of an SMA connector, allowing for the simultaneous connection of three ADFMR devices. (Center) Sample holder mounted within the electromagnet showing the support pole that contains the SMA lines used to connect the sample to the RF characterization equipment (function generator and spectrum analyzer). (Right) A zoomed-out view of the setup showing the full electromagnet, the stepper motor and shaft encoder, and the rack that contains the RF measurement equipment, magnet power supply, and control computer.

encoder, allowing for precise ($< 1°$) control of the in-plane rotation of the devices and then placed within an electromagnet. A mounted sample holder can be seen in the center panel of Figure 3.2, and the full measurement setup can be seen in the right panel.

The output IDT of the devices was similarly wirebonded, with the signal being routed to the spectrum analyzer. The spectrum analyzer trigger (gate) was linked to the video out port of the signal source, and was used to synchronize the measurements. A time delay of $\approx$ 800 ns was manually input into the trigger configuration of the spectrum analyzer to account for the delay time required for the SAWs to propagate between IDTs. A schematic drawing of this portion of the measurement setup can be seen in Figure 3.3.

In contrast to the vector network analyzer used to characterize the SAW delay lines, for ADFMR measurements the samples were connected to an Agilent E8257D signal generator

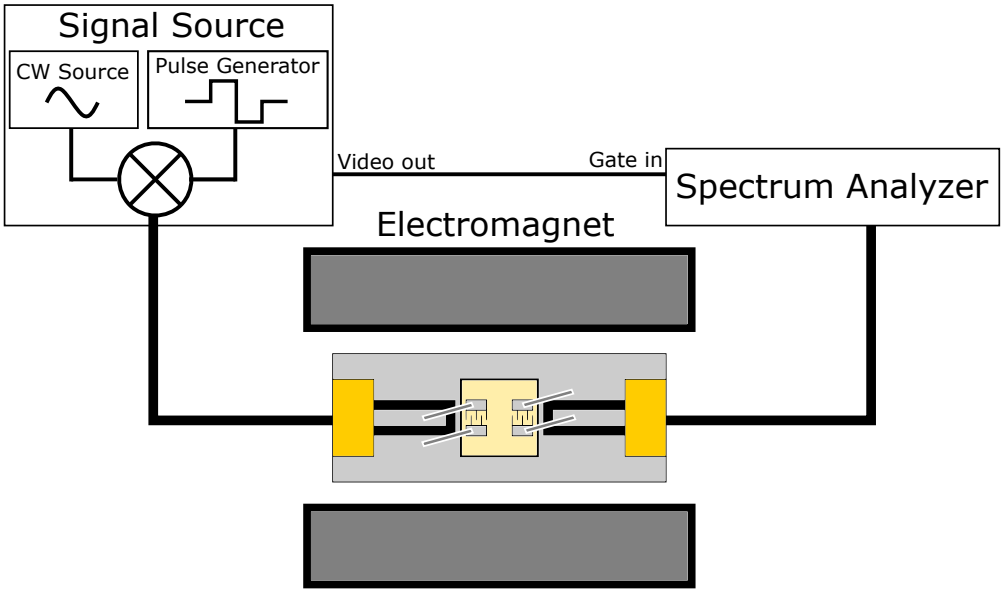

Figure 3.3: Schematic of experimental measurement setup, illustrating connections between the signal source, function analyzer, and measured device. The devices were placed on a rotation stage (not pictured) within an electromagnet to allow for control of the magnitude and direction of the applied magnetic field.

and an Agilent CXA 9000A spectrum analyzer with hardware time-gating capability. The ability to time gate in hardware as opposed to software (through physical time-domain gating of the signal as opposed to doing transformations on a frequency-domain sweep) allowed for faster data collection and lower noise levels. The function generator was used to output pulses at the specified measurement frequencies with pulse widths of 700 ns and a repetition rate of 500 kHz. The output power level was varied in order to measure the effect of input power level on absorption. The spectrum analyzer input was time gated to ensure that spurious electromagnetic signals from the IDTs would not interfere with the measured SAW transmission power. The electromagnet used to apply a bias field was a GMW 5403 driven by a Kepco BOM 20-20 (which was controlled by an analog voltage produced by an NI PCIe-6341 DAQ). A schematic of the full setup can be seen in Figure 3.4.

3.3 Experimental results

Once samples were fabricated and mounted, the field-dependent attenuation of the ADFMR was measured as a function of applied field angle. These measurements were made at the 3rd, 5th, 7th, and 9th harmonics of the IDTs, and at input power levels from 10 dBm to -60 dBm. For all test cases, samples with magnetic elements of 300, 600, and 1200 μm were measured in order to establish the dependence of ADFMR absorption on element length.

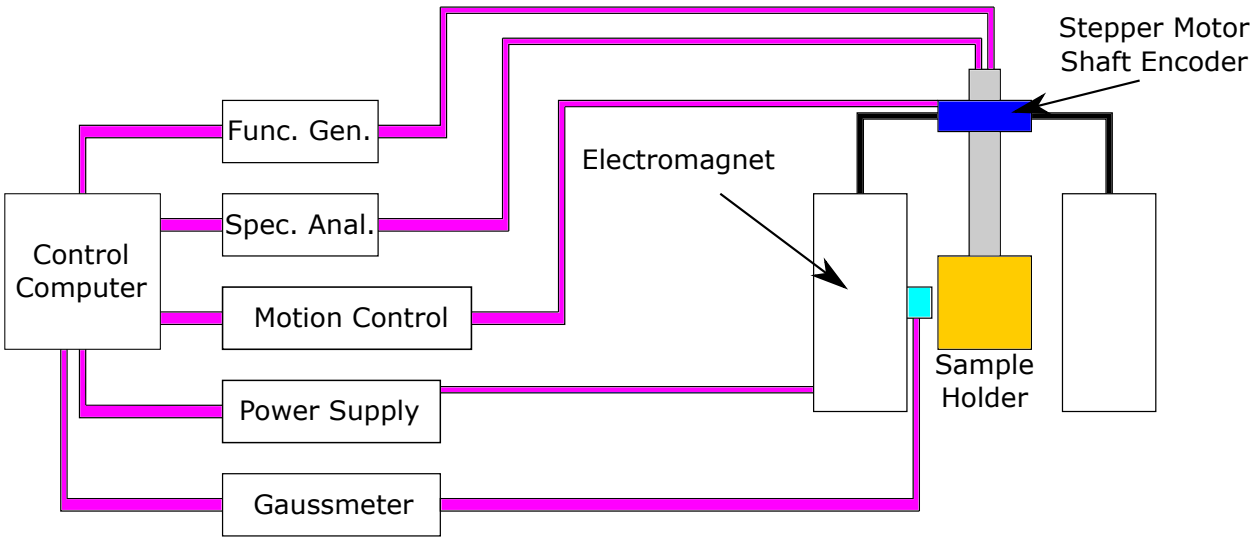

Figure 3.4: Schematic of the measurement setup. Magenta lines lines indicate signal connections. Control of all instruments is unified through a set of LabVIEW programs.

All discussion of absorption in this section is done with respect to a high field (B = 3.5 kG) measurement of IDT transmission. An un-normalized absorption scan can be seem in Figure 3.5. As can be seen, despite a large input power of 10 dBm, the transmission saturates at approximately -61.5 dBm due to the high insertion loss of the SAW delay line structures used in this work. The observed insertion loss is especially high due to the fact that the IDTs are driven at high harmonics of their fundamental frequency.

For each measurement presented in this section, the insertion loss is removed using the following procedure. First, a high magnetic field (B = 3.5 kG) is applied along the direction of the field sweep. The transmitted power through the device at this field (which pushes the ferromagnetic resonance frequency far from the excitation frequency) is then measured. Afterwards, a sweep of the magnetic field for smaller field values (B=0-500 G) is performed, with a measurement of the transmission being performed at each field point.

These transmission values are then normalized using the high-field value taking earlier, resulting in plots where the absorption goes to 0 dB at high fields (as opposed to saturating at a value equal to the device insertion loss). A negative absorption value, therefore, indicates that the transmitted power is below this high-field value. This same method has been utilized to remove insertion loss in previous work on ADFMR devices[58, 35, 111, 27].

Figure 3.6(a) shows a plot of absorbed power as a function of the angle of the in-plane magnetic field for a 25 nm thick Ni magnet sitting at the middle of the IDTs at 1992 MHz. The peak of the absorption appears at $\approx 40^\circ$ which is very close to what has been predicted theoretically ($\approx 45^\circ$)[27]. Note that anisotropy in the magnet could lead to an angle that is significantly different from this ideal value [111]. We now choose one of this angles of highest absorption (shown by the arrow in Fig. 3.6(a) and plot it as a function of frequency in Fig

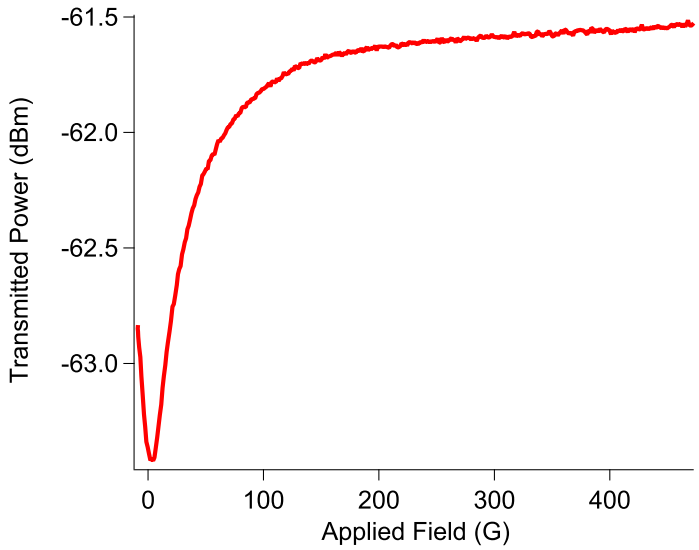

Figure 3.5: Plot of raw transmitted power in an 20 nm nickel ADFMR device at 2000 MHz. Input power to this device was 10 dBm, and a maximum transmitted power level of ≈ -61.5 dBm can be observed, corresponding to a minimum insertion loss of ≈ 71.5 dB. This extremely high insertion loss is attributed to the excitation of the IDTs at high harmonics of their fundamental frequency, as well as poor RF impedance matching.

3.6(b). Note that from the transmission far from resonance, it is possible to estimate the loss in the system. Therefore, by knowing the input power and S_{21}, one can calculate the power going into the SAW. These estimates were used at various frequencies to ensure that the input power going into the SAW at each frequency is roughly 1 μW. Note that significant field-tunable attenuation is observed in Fig. 3.6(b) even at this very low input power.

Importantly, by normalizing the input power and thereby accounting for the varying amount of loss at different input frequencies, we are able to demonstrate that the relative magnitude of ADFMR absorption increases with increased frequency. This result confirms that the power absorption trend seen in ADFMR matches that of conventional FMR in thin films.[54]

One can compare the shape of the 2D plot (as seen in Figure 3.6(a) above) as a function of frequency and film thickness to get an idea of the impact of film anisotropy (and various spin-wave contributions) on deviations from the expected shape proposed by Dreher et. al.[27]. The deviation is caused by the changing shape of the imaginary part of the permeability, which is fit using the equations discussed in Section 7.2. A comparison of measurements taken on the same film at different frequencies can be seen in Figure 3.7, showing an increasing divergence from the expected 45 ° maxima offsets as frequency increases. An extremely thin film, such as the one depicted in Figure 3.8, shows minimal deviation from the predicted shape, but as one increases the film thickness deviations become apparent, as shown in Figure

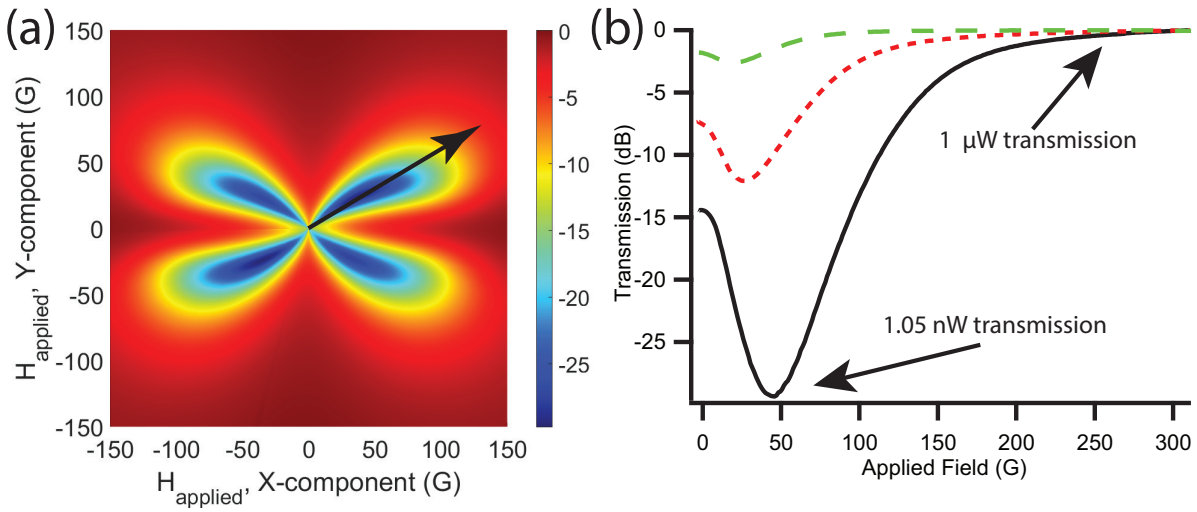

Figure 3.6: (a) Plot of the absorption of SAW power by the magnetic element (in dB) as a function of applied x and y magnetic field at a SAW frequency of 1992 MHz. The x-directed field is taken to be along the direction of SAW propagation, while the y-directed field is in-plane and perpendicular to the SAW travel. The characteristic 4-lobed signature of ADFMR is clearly visible. The absorption maxima can be seen when the applied bias field is $\approx 40°$ from the SAW propagation direction. (b) Line cut along the direction indicated by the black line in (a) at SAW excitation frequencies of 857 MHz (green long dash), 1424 MHz (red short dash), and 1992 MHz (black solid). All data was collected at the same absolute SAW power of 1 μW, and shows that ADFMR follows the expected FMR relationship with frequency.

3.9.

As can be seen from these figures, experimental measurements diverge significantly from the proposed lineshapes of Dreher et. al. [27], especially as one moves to higher frequencies and in thicker films. A more complex fit, like that proposed by Gowtham et. al.[35] is required to capture additional effects that become important as the spin-wave contributions play an increasing role in determining the permeability of the material. By applying this more accurate fit to our experimental data, we are able to extract film damping and magnetoelastic coefficient, as discussed in more detail in Section 7.2.

Absorption dependence on input power

In order to evaluate the behavior of this effect at different power levels, data was taken along the angle of maximum absorption (as depicted in Figure 3.6) over a wide range of input powers by inserting a variable attenuator into the system. A plot of series of such line cuts taken at successively decreasing power levels can be found in Figure 3.10. As can be seen, beyond a change in the high-field insertion loss, the absorption curves are not only qualitatively, but also quantitatively, similar.

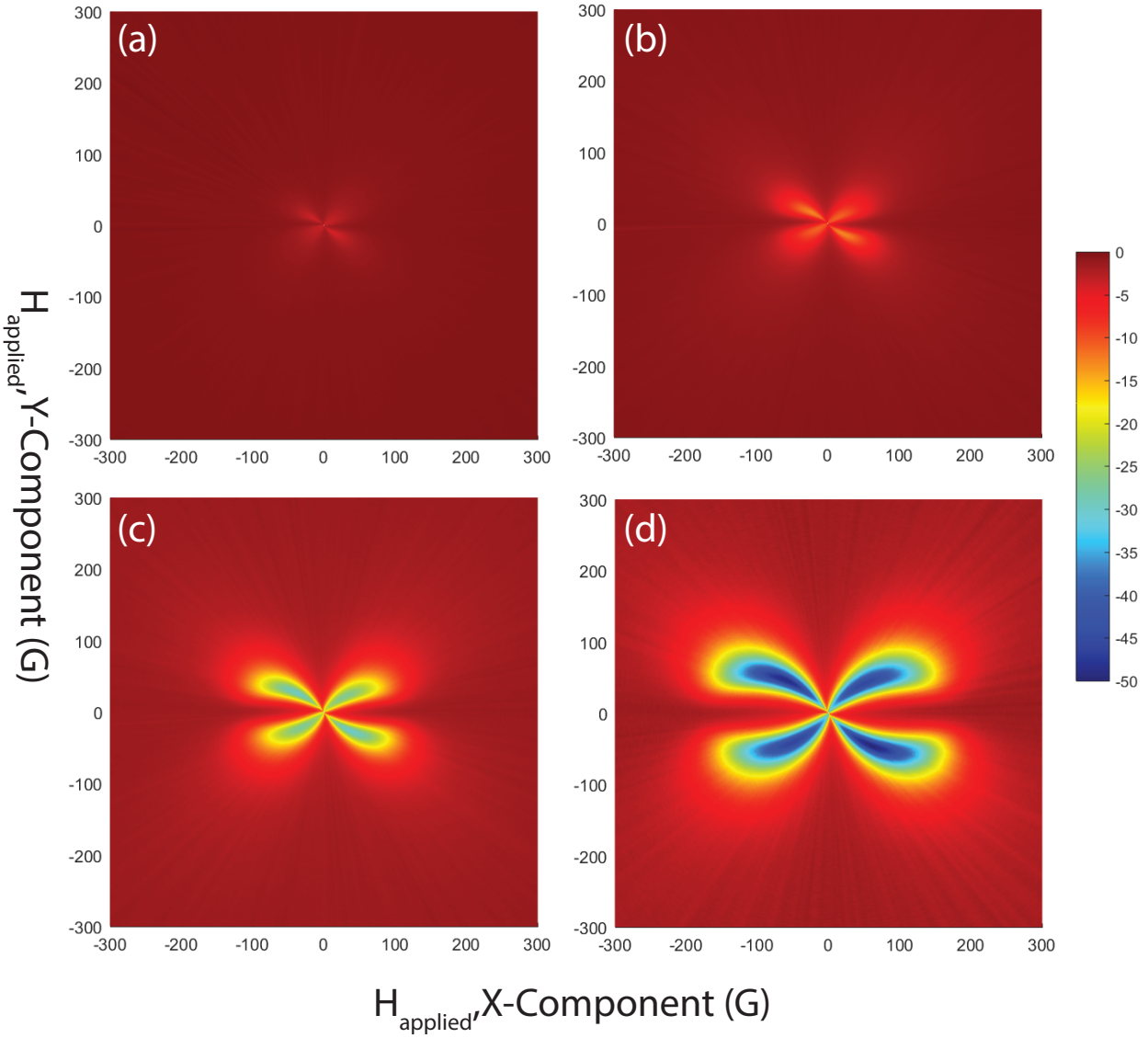

Figure 3.7: Plots of the absorption of SAW power by the magnetic element as a function of applied x and y magnetic field at SAW frequencies of 861 (a), 1430 (b), 2000 (c), and 2565 MHz (d). All measurements were performed on a 20 nm Ni film with a 5 nm Au capping layer. All plots share the same color bar (right) in dB/mm.

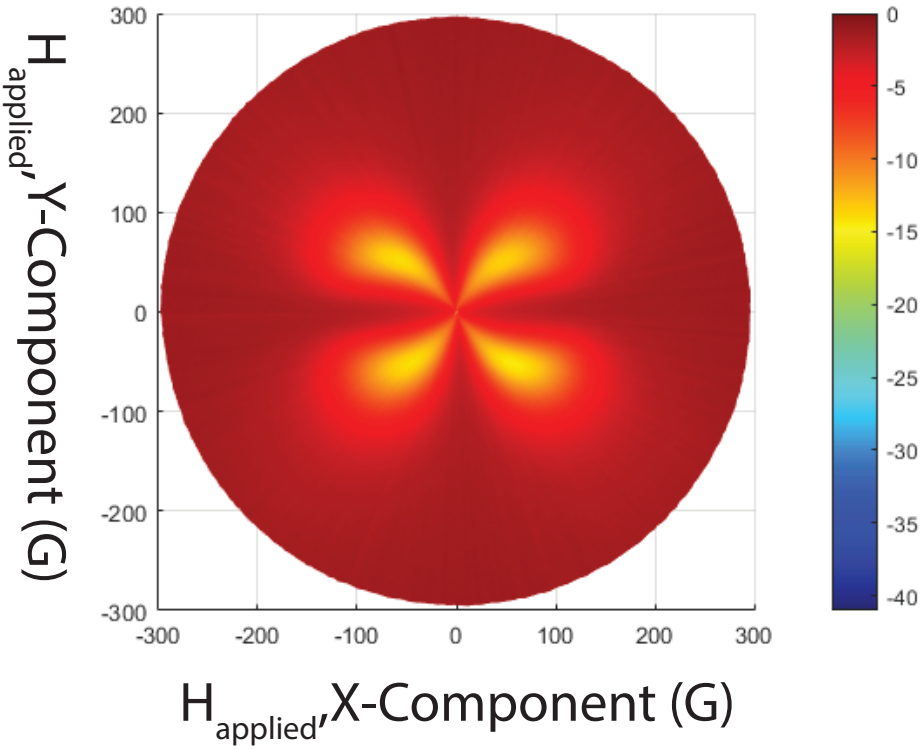

Figure 3.8: Plot of the absorption of SAW power by the magnetic element as a function of applied x and y magnetic field at Ni thicknesses of 10 nm, capped with 5 nm of gold. The measurement was performed at 2000 MHz, and the scale bar indicates absorption in dB/mm.

This similarity can be better observed by plotting the magnitude of the absorption dip for a variety of input powers and frequencies as can be seen in Figure 3.11 below. Since the system should be nearly symmetric (barring fabrication errors), the power at the magnetic element was taken by dividing the device insertion loss by two and applying that halved insertion loss figure to the input power. As is evident from the plot, the absorption at a given frequency (in dB) is entirely independent of input power across the range tested.

The characterization of this power dependence is critical from an application perspective, as a strong dependence on applied signal amplitude would likely disqualify these devices from any realistic use case. Linear (or at least linearizable) components form the backbone of system design. Without linear components, some of the most fundamental signal processing techniques (such as amplitude modulation) become untenable, severely restricting the usefulness of any device. By confirming the linearity of the ADFMR system (at least in the mW and below regime), we are able to make a substantially more convincing case for its usefulness in commercial systems.

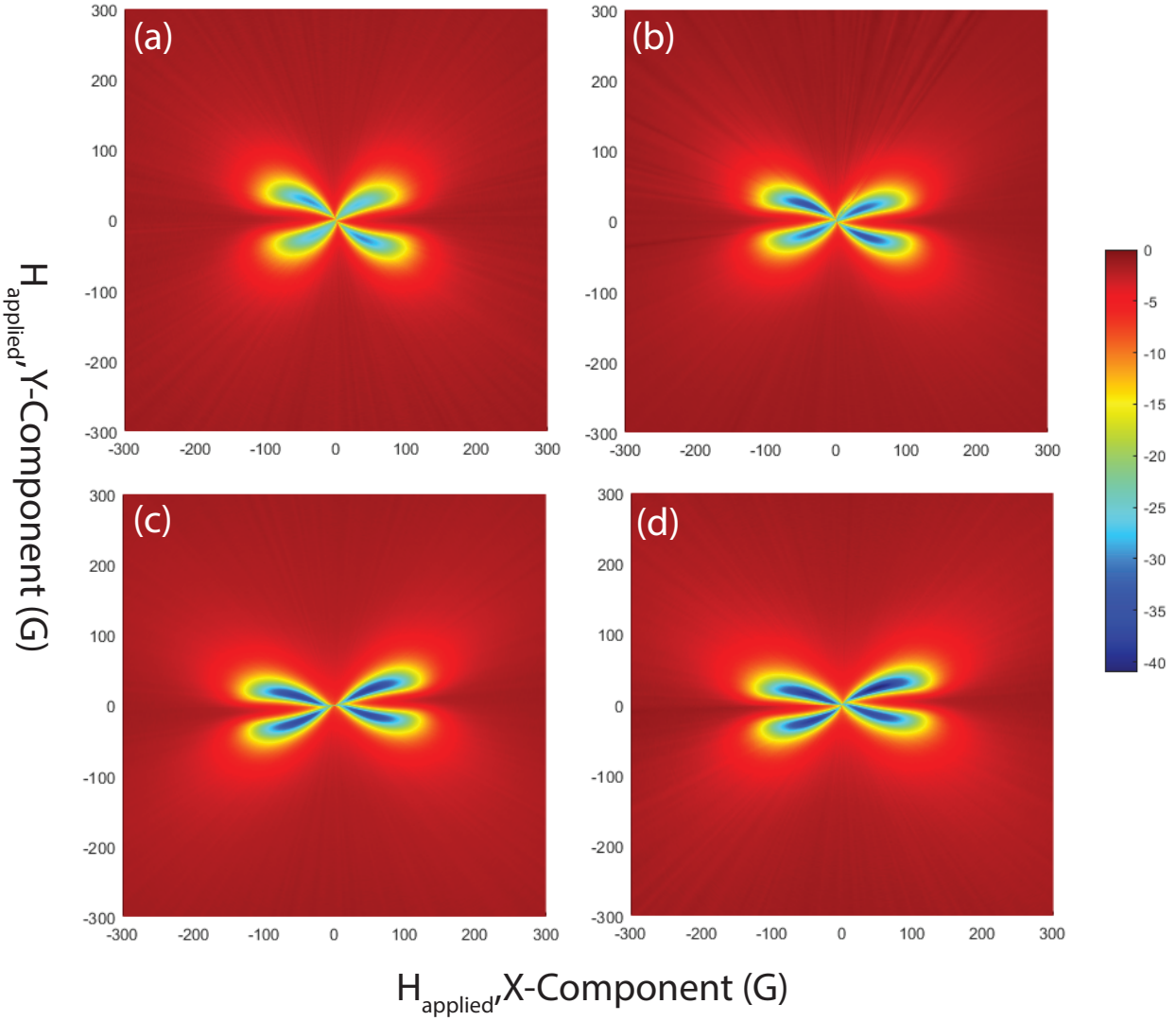

Figure 3.9: Plots of the absorption of SAW power by the magnetic element as a function of applied x and y magnetic field at Ni thicknesses of 20 (a), 30 (b), 40 (c), and 50 nm (d). All samples had a 5 nm Au capping layer, and all measurements were performed at 2000 MHz. All plots share the same color bar (right) in dB/mm.

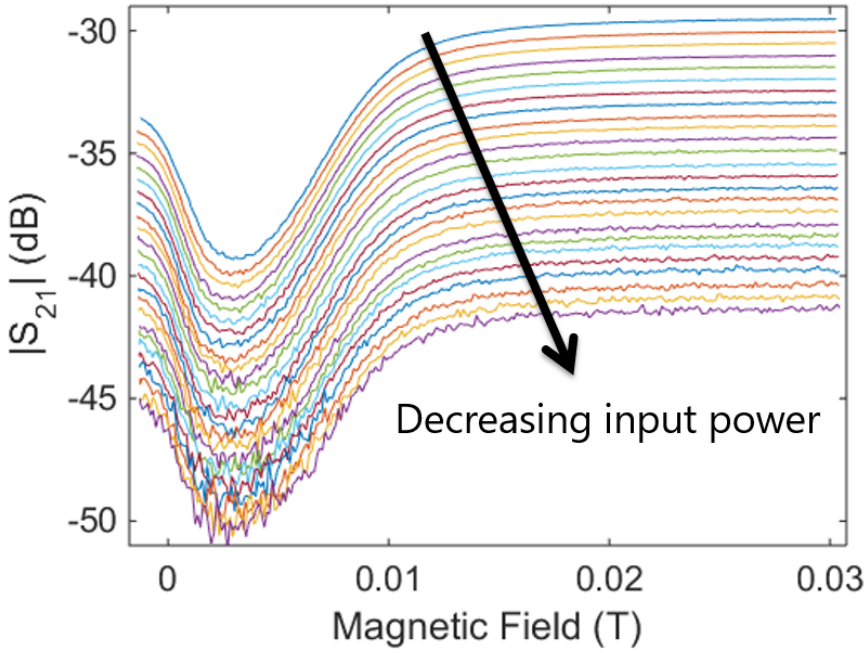

Figure 3.10: Power absorption as a function of applied field for an example sample over a range of input power values. As can be seen, the curves are largely identical as power decreases except for the increased high-field insertion loss (as would be expected with an increasing series attenuation) and increased noise.

Absorption dependence on element length and thickness

Beyond linearity in power, it is also important to determine how various scaling factors can affect ADFMR. In previous sections of this chapter, absorption dependence on frequency has been explored and characterized. Here we consider the dependence of device absorption on film length and thickness, and how these variables can be tuned to control the absorption depth to optimize for different applications (ie. the desired $\approx$ 6 dB absorption dip for magnetic sensing as described in Section 4.3).

Magnetic element size was varied along the length dimension (along the direction of SAW travel). A compilation of these measurements can be found in Figure 3.12. For both 25 and 50 nm thick samples, the absorption of the traveling SAW scales exponentially with length. The rate of this scaling is determined by the thickness, with the thicker film attenuating the signal at a faster rate. The exponential variation in absorption with element length is in agreement with established theory, which predicts an exponential increase in absorption with magnetoelastic film volume.

The absorption maxima of these scans were then plotted as a function of film thickness, as can be seen in Figure 3.13. At each film thickness, the expected trend of increased absorption with increased drive frequency can be observed. In addition, the absorption

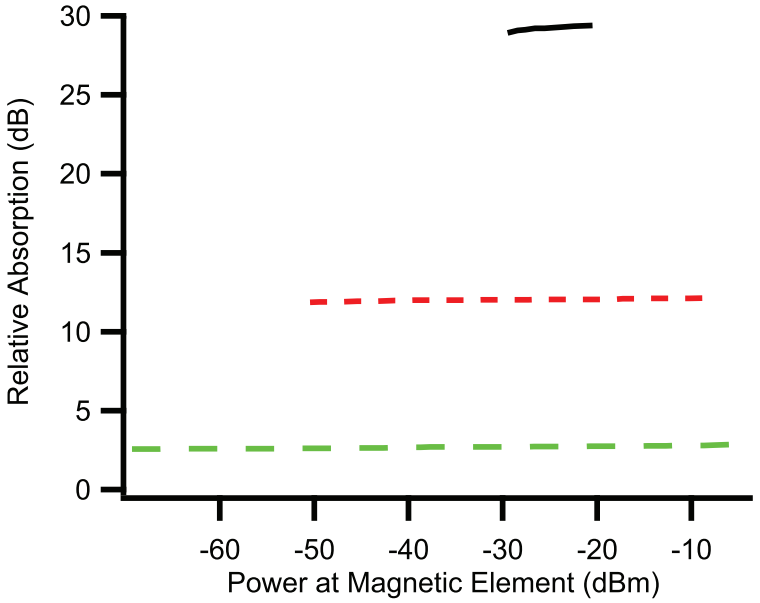

Figure 3.11: Plot of power absorption as a function of input power for three different SAW frequencies: 857 MHz (green long dash), 1424 MHz (red, short dash), and 1992 MHz (black solid). The absorption (in dB) at each frequency remains constant across all input powers tested.

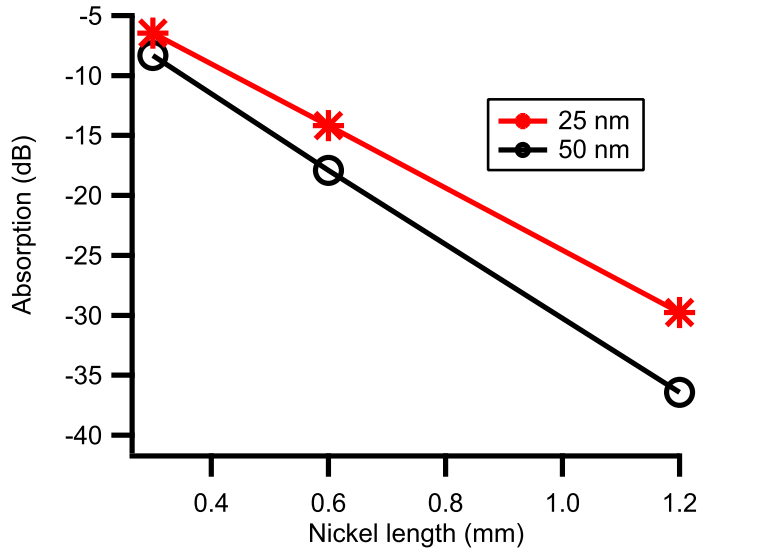

Figure 3.12: Absorption as a function of device length for both 25 and 50 nm thick devices. Absorption scales exponentially with the length of the magnetic element at a rate of -25.9 dB/mm for the 25 nm samples, and -31.2 dB/mm for the 50 nm samples. All absorption data was collected at 1992 MHz.

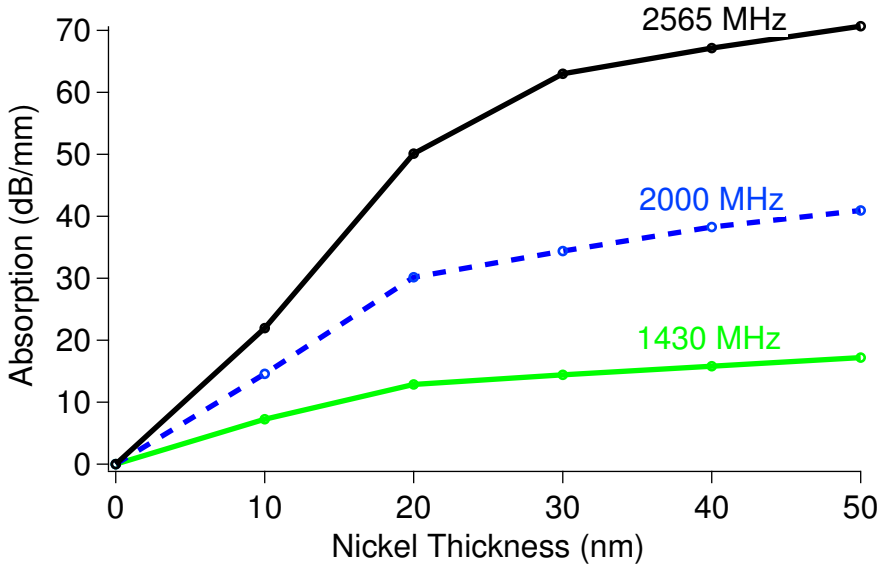

Figure 3.13: Maximum absorption as a function of film thickness at 1430 (green solid), 2000 (blue dashed), and 2565 (black solid) MHz. A saturating behavior can be observed with increasing film thickness, indicating that vertical scaling of ADFMR devices for enhanced absorption is less effective than lateral scaling once film thicknesses exceed $\approx$ 20 nm.

at each frequency seems to follow a saturating behavior as the film thickness is increased, which indicates diminishing returns with regards to enhancing absorption by increasing film thickness. When compared to the study on length dependence, this indicates that lateral (rather than vertical) scaling is a more efficient method for enhancing absorption in ADFMR systems beyond the ultrathin regime ($<$ 20 nm). Given that the magnetoelastic coupling coefficient for these films extracted from the fit is independent of film thickness and frequency, we attribute this saturation of the absorption to the increased damping observed in thicker Ni films. The extraction of this damping and its correlation with the absorption saturation can be found in Section 7.2.

Chapter 4

Acoustically driven ferromagnetic resonance for magnetic sensing

One potential application of the acoustically driven ferromagnetic resonance technique is for use in precision magnetic sensors. The large absorption efficiency in these films results in a very steep slope as the magnetic film enters resonance. By biasing the device in this region of operation, the slope of transmitted power as a function of externally applied magnetic field can be extremely steep (on the order of 1 W/T). In addition, since the resonances we study occur at relatively high frequencies ($\approx$ GHz), we are able to limit the influence of low-frequency noise on the system. This combination of factors results in a device capable of achieving comparable sensitivity to the best sensors today (fT / $\sqrt{\text{Hz}}$) in a room-temperature, solid state package that can be produced for minimal cost.

Section 4.1 describes applications for high sensitivity magnetometry. Section 4.2 then discusses existing technologies that are attempting to fill these needs, and compares them to the devices proposed by the authors of this thesis. The following sections then dive deeper into the characteristics of the proposed device, with section 4.3 focusing on the sensitivity and linearity of the sensor, section 4.4 providing fabrication details, and section 4.5 discussing the sources of noise present in the current system.

4.1 Applications for high-sensitivity magnetometry

Magnetic sensing finds use in a variety of applications as diverse as automotive, resource exploration, and medical imaging. While some applications are able to utilize cheap, rugged, solid-state sensors, tasks that require high-sensitivity magnetometry have thus far relied on expensive and bulky tools like SQUID and SERF magnetometers that require cooling and heating (respectively) to temperatures far from ambient conditions. ADFMR-based magnetic sensors should enable this high-sensitivity measurement at a price, and in a form factor, that is more amenable to widespread adoption.

One critical application of this sort of magnetic sensing is in a clinical environment. A

number of medical imaging techniques, for example magnetoretinography[105, 4, 49], magnetocardiography[80, 55, 32], and magnetoencephalograpy[19, 18, 38], require the measurement of extremely small (< 1 pT) magnetic fields generated by processes in the human body. Due to the small fields involved, and the desire for high spatial resolution, all instruments for such measurements require the use of cryogenic Superconducting Quantum Interference Device (SQUID) magnetometers. The cooling requirements for these sensors result in measurement equipment that is large, bulky, and expensive to operate. Also, due to the fact that these sensors are fundamentally absolute field sensors (and any gradiometry is done in post-processing), large shielded enclosures are required to eliminate the effect of environmental noise, which could easily overwhelm the actual signal.

Beyond clinical uses, wearable devices have also recently gained substantial popularity both as a consumer health device and as a medical diagnostic tool that enables constant monitoring. Current medical wearables are commonly used to monitor health indicators such as blood pressure and heart rate[66, 47, 76]. These devices, however, must rely on either unreliable optical sensors (which have issues with perspiration, variable skin tones, and motion) or uncomfortable ECG leads. By measuring these factors magnetically (which has thus far been impossible to do in a wearable form factor), it would be possible to resolve a number of the issues patients have identified as most pressing[75].

A radically different application for magnetic sensing presents itself in navigation in GPS-denied environments. A number of techniques have been proposed to direct aircraft and other airborne craft in environments where GPS is either unavailable or unreliable, but each comes with a variety of downsides that has made them untenable for realistic applications. For example, terrain-sensing radar cannot be used over water, and is sensitive to changes in surface features, such as deforestation or construction. Recently, sensing of the Earth's magnetic anomaly field has emerged as an alternative that should be much more robust with respect to terrain variation on the relevant timescales (years)[8, 9]. Implementation of this technology has been slow, however, as magnetometers with sufficient sensitivity and stability (ie. SQUID magnetometers) do not have form factors that can be easily integrated into aircraft. ADFMR magnetometers, with their small size and capability for room-temperature operation, could enable magnetic navigation in real-world systems.

4.2 Existing magnetic sensors

In order to properly evaluate the performance of ADFMR devices for magnetic sensing applications, it is first necessary to discuss competing technologies. Table 4.1 provides a concise summary of commercially available sensing technologies in the modern market in comparison to the devices tested in this thesis.

As can be seen by in Table 4.1, the best high-sensitivity (≈ 1 fT$/\sqrt{\text{Hz}}$) magnetometers that are currently available require substantial deviations from room temperature to operate, and are often very expensive to purchase. They also have difficulties performing precise measurements in high fields. SERF magnetometers, for example, show an enhancement of

Table 4.1: Summary of commercial magnetic sensing technologies (and ADFMR sensors)

Name	Magnetic Noise	Volume	Operating Temperature	Cost
SERF	0.5 fT/$\sqrt{\text{Hz}}$[56]	3 cm^3 [77]	180 °C[56]	10's k$
SQUID	1 fT/$\sqrt{\text{Hz}}$[89]	1 cm^3[77]	Cryogenic	10's k$[77]
ADFMR	5 fT/$\sqrt{\text{Hz}}$	1 mm^3	Room Temp	1-10 $
Fluxgate	2 pT/$\sqrt{\text{Hz}}$[83]	1 cm^3[77]	Room Temp	1 k$[77]
Proton	10 pT/$\sqrt{\text{Hz}}$[77]	1 cm^3[77]	Room Temp °C [77]	5 k$[77]
Magnetoresistive	200 pT/$\sqrt{\text{Hz}}$[11]	1 μm^3[77]	Room Temp	1 $[77]
Hall	77 nT/$\sqrt{\text{Hz}}$[87]	1 μm^3[77]	Room Temp	0.1-1 $[77]

Table 4.2: Figure of merit for commercial magnetic sensors (and ADFMR sensors)

Name	Figure of Merit ($\sqrt{\text{Hz}}$/fT*m)
ADFMR	200
SERF	138.5
SQUID	100
Magnetoresistive	5
Fluxgate	0.05
Hall	0.013
Proton	0.005

measurement noise to $\approx$ 1 pT/$\sqrt{\text{Hz}}$ when exposed to fields above a few nT[91] - for reference, the earth's magnetic field is on the order of 100 μT. Alternatives to these SQUID and SERF magnetometers all show maximum sensitivities in the pT/$\sqrt{\text{Hz}}$ range, disqualifying them for use in a number of critical applications, such as magnetoencephalography [38] and magnetocardiography [55].

An important figure of merit in the comparison of these magnetic sensors is the inverse of the sensitivity*$\sqrt{\text{area}}$ ($\sqrt{\text{Hz}}$ / fT*m). As the signals from multiple small magnetometers can be averaged together to reduce the overall system noise, it may be possible for a large array of small, noisy magnetometers to actually become competitive with some intrinsically higher sensitivity devices. In this figure, the square root of the sensor area acts as a density factor to indicate this averaging potential (the square root is necessary as noise is reduced by a factor of number of devices squared). The area is estimated by calculating the footprint of the enclosing cube for the volumes cited in Table 4.1. For some sensors (like SERF magnetometers) this is an overly optimistic estimate, as these volumes only include the field-sensitive element and do not include the optical and electronics components, which can easily double the total size of such systems. Table 4.2 shows the magnetometers from Table 4.1 listed in order of this figure of merit. As can be seen, in this scale the miniaturized solid-state magnetometers appear much more competitive with SQUID and SERF systems.

In the remainder of this chapter, an outline will be provided for how a room-temperature

ADFMR magnetometer can achieve the same sensitivities seen in SERF and SQUID systems, while functioning over a much wider range of applied field biases. These magnetometers would be able to leverage the extremely low costs seen in other solid-state sensors (magnetoresistive, Hall, etc.), while achieving sensitivities usually reserved for much more expensive and much less environmentally robust devices. Successful deployment of such devices has the potential to disrupt a number of industries that rely on high-sensitivity magnetometry, such as medical imaging and resource exploration.

In addition to standard absolute field magnetometry, the case of gradient magnetometry is also explored in this chapter. Gradient magnetometry is extremely useful for many of the same applications as absolute field magnetometry - for example, magnetoencephalography equipment often leverages gradiometers.[108] Such gradiometric techniques have the advantage of (a) being able to reject environmental noise and (b) have lower requirements on the dynamic range of the circuitry involved, as the comparatively large offset caused by the influence of earth's magnetic field can be removed. Given that many magnetic sensing applications rely on precise measurements of the change in magnetic field (as opposed to its absolute value), the advantages of gradiometry can be leveraged in these systems to reduce noise and reduce component costs.

4.3 Sensitivity and linearity

In developing a high-sensitivity magnetometer, it is critical to optimize sensitivity - the change in the device's output (be it voltage, frequency, power, etc.) as a function of applied magnetic field. If the sensor has an insufficient sensitivity, it may become difficult (if not impossible) to measure the desired signals above the noise sources in the system. In general, it is optimal to have a linear dependence of the output variable on magnetic field in the desired operation region to ease readout.

The simplest way to calculate the sensitivities of ADFMR devices to magnetic field would be to compute the field derivative of experimental power measurements (such as those shown in Figure 3.6). Such an analysis, however, would substantially underestimate the capabilities of these devices, as our current device design uses a high insertion loss harmonic excitation method to allow us to operate at many different frequencies on a single device. Thus, all analysis in this chapter is performed on scaled data that assumes an insertion loss of 4 dB (a pessimistic estimate, as SAW delay lines have been fabricated with insertion losses as low as 1 dB[118]). In addition, analytical calculations indicate that the optimal sensitivity is found when the absorption depth of these devices is 6 dB. Given that this is very achievable and easy to tune [58], our analysis scales the experimental absorption data to reach this optimal value.

A plot of the sensitivity extracted with this procedure for a 1 mW input power, 4 dB insertion loss device can be found in Figure 4.1. As can be seen, the sensitivity peaks in two distinct locations: one with a bias field of $\approx$10 Oe, and one with a bias field of $\approx$60 Oe. The low-field sensitivity peak remains within 5% of its peak value over a range of approximately

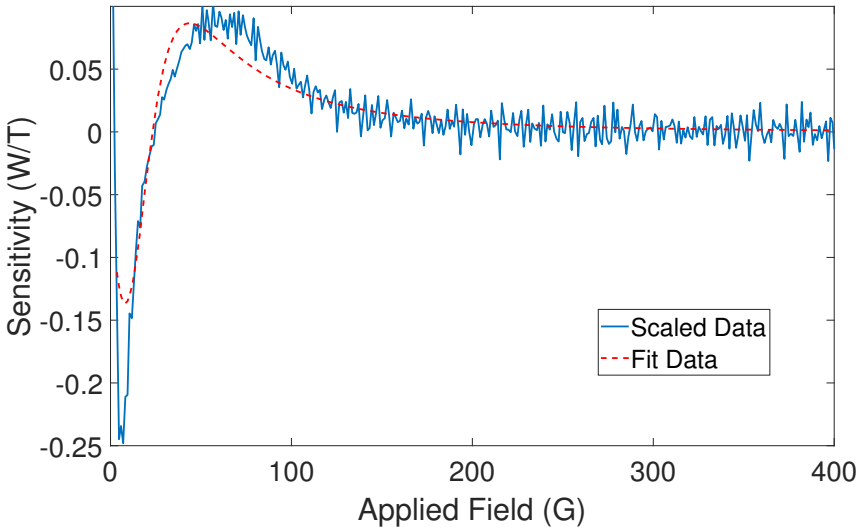

Figure 4.1: Sensitivity as a function of bias field for a device with 4 dB insertion loss and 1 mW input power and a 6 dB absorption dip. The solid blue line is scaled experimental data, while the dashed red line is an analytical fit to the data.

Table 4.3: Scaled experimental sensitivities for measured devices (W/T)

	861 MHz	1430 MHz	2000 MHz	2565 MHz
10 nm	0.415	0.357	0.197	0.393
20 nm	0.234	0.170	0.263	0.210
30 nm	0.337	0.907	0.358	0.187
40 nm	0.182	0.164	0.148	0.193
50 nm	0.147	0.169	0.188	0.300

5 Oe, while the high-field peak remains within 5% of its peak value over approximately 12 Oe, which should allow for a large range of operation for the final magnetometer. A table of the extracted peak sensitivity values for devices with a wide range of operating frequencies and film thicknesses can be found in Table 4.3. As can be seen from the table, sensitivity appears independent of film thickness and excitation frequency (as long as the absorption peak remains fixed at 6 dB). The average sensitivity extracted for all devices is 0.276 W/T.

From these sensitivity values, when the external field is 1 femtoTesla, the dV/dB for the proposed sensor comes to be $\approx 4 * 10^7$ V/T. For calibration, the current best integrated magnetic field sensors that use a magnetic element are magnetic tunneling junction (MTJ) sensors with a sensitivity of $\approx$ 100 V/T for a single sensor [65, 24] and a maximum of $\approx$ 500 V/T for arrays of several hundred MTJs[24]. Considering these values, the proposed sensor has $\approx 10^5$ times higher sensitivity compared to MTJ sensors. This large sensitivity allows us to detect extremely small magnetic fields (and gradients) previously inaccessible

to solid-state sensors.

4.4 Sensor construction

A schematic diagram of the proposed sensor element can be seen in Figure 4.2. The critical elements of this design are:

1. A large volume magnetic film to minimize thermal magnetic noise
2. Two independent sets of IDTs (essentially two ADFMR devices) to enable gradiometric measurements to reject common-mode noise
3. A backside heater to precisely control the temperature of the system and minimize the effects of thermal drift on the magnitude of the signal absorption
4. Suspensions for thermal isolation to improve the stability of the temperature control and to reduce the power required to run the heater.

To fabricate the devices, we first start with a six inch lithium niobate substrate. First, the backside heater structures will be patterned with photolithography. These patterns will then be metalized via a liftoff process with the deposited metal being very thin (< 10 nm) to prevent spurious magnetic signals due to thermal currents. Afterwards, the backside will be protected with a PDMS coating.

The interdigitated transducers will then be patterned on the front side of the wafer with fundamental frequencies between 1 GHz (feature size 870 nm) and 3 GHz (feature size 300 nm) via deep UV photolithography using an ASML 5500/300 DUV stepper. Aluminum electrodes will be deposited using a liftoff process. Once the electrodes are defined, a third lithography step is done to define the ferromagnetic regions. These ferromagnets are deposited using an ultra-high vacuum sputtering machine. Because of the large size and very small thickness of the magnets, and room temperature synthesis, liftoff can be done using sputtering (our current devices are made in this way). Finally, a further lithography step will be performed to pattern the suspended arms of $LiNbO_3$ used for thermal isolation.

The proposed process flow for this sensor element can be found in Figure 4.3. The detailed process is as follows:

(a) Start with double side polished lithium niobate substrate

(b) Spin photoresist

(c) Expose and develop photoresist to define backside resistive heater

(d) Deposit thin metal layer (< 10 nm) via e-beam evaporation

(e) Strip photoresist

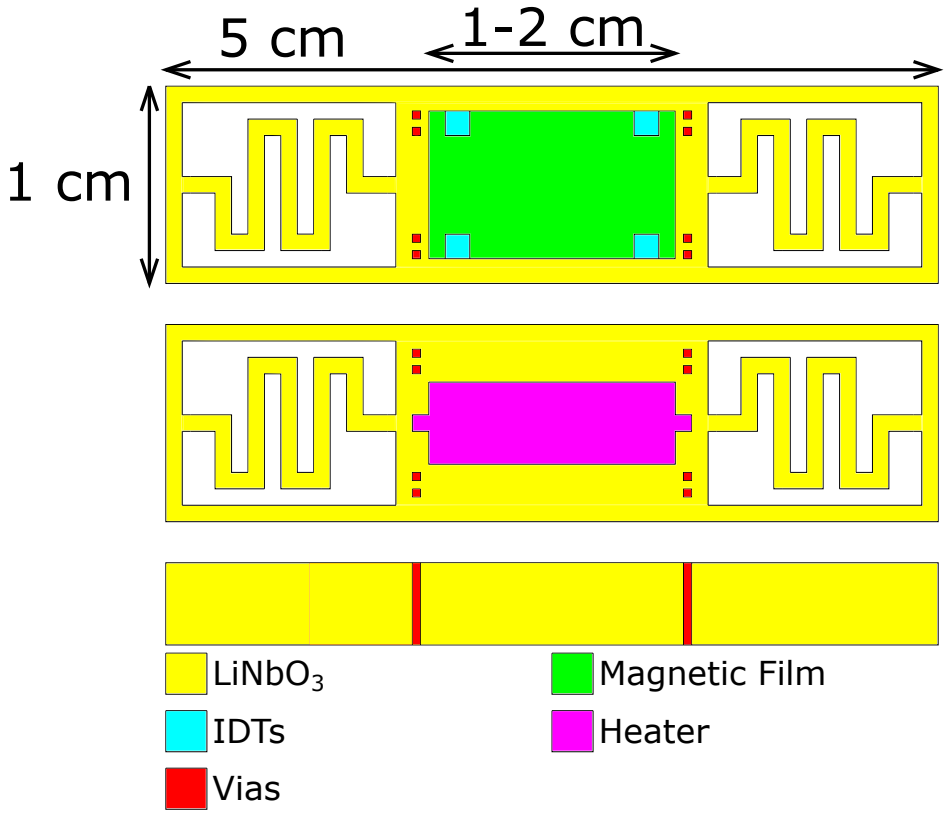

Figure 4.2: 2D views of the top and bottom sides of the $LiNbO_3$ substrate showing the ADFMR structure and heater in the sensor structure. Also shown are suspensions for thermal isolation. Note the presence of two independent ADFMR systems that share a single large magnetic film (to minimize the effect of intrinsic magnetic noise). These two sensors allow for the device to be run in a gradiometric configuration to reject common-mode noise sources and further improve measurement sensitivity.

(f) Spin on PDMS coating to protect wafer backside during subsequent processing steps

(g) Flip wafer and spin photoresist

(h) Expose and develop photoresist to define interdigitated transducers

(i) Deposit 70 nm aluminum via e-beam evaporation

(j) Strip photoresist

(k) Spin photoresist

(l) Expose and develop photoresist to define magnetic film region

(m) Deposit magnetic film via sputtering

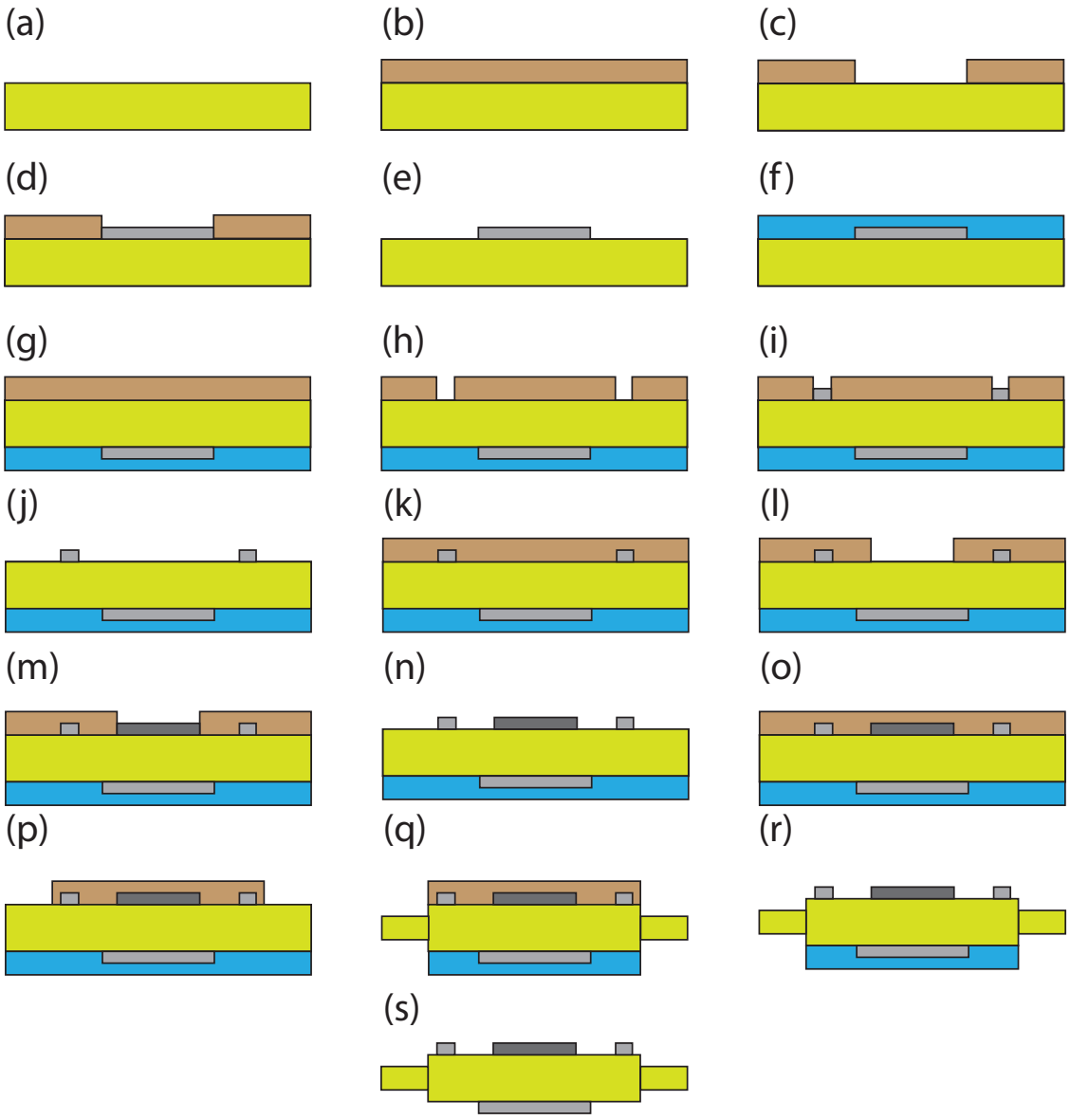

Figure 4.3: Graphical process flow for the proposed ADFMR magnetic sensor.

(n) Strip photoresist

(o) Spin photoresist

(p) Expose and develop photoresist to define suspensions for thermal isolation

(q) Etch suspensions

(r) Strip photoresist

Table 4.4: Summary of noise sources in ADFMR magnetometers

Noise source	Common mode?	Noise level
Thermal (electrical)	no	27 aT / $\sqrt{\text{Hz}}$
Thermal (magnetic)	no	4.32 fT / $\sqrt{\text{Hz}}$
1/f (electrical)	no	≈ 0
1/f (magnetic)	yes	≈ 0
Power line	yes	≈ 0
Oven control current	yes	0.54 fT / $\sqrt{\text{Hz}}$

(s) Strip PDMS

4.5 Noise

A summary of assorted noise sources in ADFMR-based magnetic sensors can be found in Table 4.4 assuming a 1 cm x 1 cm x 100 nm nickel film and an applied field in the fT range. As can be seen from the table, a number of factors that dominate the noise in other solid-state sensors (ie. magnetic and electrical 1/f noise) are minimized in this system. The table also indicates which noise sources are common-mode and could be easily filtered out in a gradiometric configuration. All table entries will be discussed in more detail in this section.

Thermal noise (electrical)

Thermal noise (or Johnson-Nyquist noise) is electrical noise caused by the thermal motion of electrons (or other charge carriers) within a conductor. This noise is universal in electronic systems, and can only be reduced by lowering the temperature of the device. The temperature dependence of this noise power is well characterized[51] and can be expressed as:

$$P_{noise} = 4k_bT\Delta f \tag{4.1}$$

Where k_b is the Boltzmann constant, T is the temperature, and Δf is the system bandwidth. For our system operating at 55 °C (328.2 K), this thermal noise power evaluates to 1.7 * 10^{-20} W / Hz. Given a 50 Ω system and a linearized sensitivity of $\approx 4 * 10^7$ V/T around 1 fT, this corresponds to a noise power of 27 aT / $\sqrt{\text{Hz}}$. This extremely small noise contribution (on the order of 20x less than the noise floor of the best modern magnetometers) is not expected to be the limiting noise factor in our system.

Thermal noise (magnetic)

Thermal magnetic noise in this system has the same origin as the thermal electrical noise: fluctuations of subatomic particles at finite temperatures. The magnetic noise in this system

can be analyzed by considering the fluctuation dissipation theorem, which describes the statistical fluctuations of a state from equilibrium.[10]

In order to analyze the magnetic noise resulting from such fluctuations, we use the formalism of [107] and replace ΔH / M_s by α (the Gilbert damping parameter) to arrive at the equation:

$$H_n = \sqrt{\frac{k_b T \alpha}{2\pi\gamma M_s V}} \tag{4.2}$$

Where k_b is the Boltzmann constant, T is the temperature in Kelvin, α is the Gilbert damping parameter, γ is the gyromagnetic ratio, V is the film volume, and M_s is the saturation magnetization. Evaluating this equation using extracted values for our films (M_s = 400 emu / cc, α = 0.02), and assuming a film volume of 1 cm x 1 cm x 100 nm, the field noise at 55 °C comes out to be 4.32 fT / $\sqrt{\text{Hz}}$.

This thermal magnetic noise is the dominant source of noise in this system, and will restrict it's ultimate sensitivity. Due to the local nature of the fluctuation, this thermal noise likely cannot be considered as common mode, and thus gradiometric techniques would not be able to substantially reduce this figure. It is possible, however, that for a saturated magnet in a bias field, some degree of correlation among the fluctuations could develop due to the exchange interaction within the material. Such a correlation would allow for this noise to be compatible with the common-mode rejection of a gradiometer geometry, and could further push down the noise floor of the system.

Several other avenues are available to reduce this noise floor, as can be determined by a cursory look at Equation 4.2. These include increasing volume, increasing M_s, or decreasing α. Of these, increasing volume is the least attractive due to its corresponding negative effects on the figure of merit shown in Table 4.4. As such, increasing M_s and decreasing α seem to be the best approaches to reduce this noise figure.

The noise figure thus be substantially improved by using a sputtered $Co_{25}Fe_{75}$ film as the magnetoelastic layer instead of nickel. Room-temperature sputtered $Co_{25}Fe_{75}$ thin films have shown Gilbert damping of α = 0.002 (with the theoretical minimum approaching α = 0.0001) and saturation magnetizations of M_s = 1900 emu / cc.[90] Using these experimental values for $Co_{25}Fe_{75}$ instead of the values for nickel in Equation 4.2, we obtain a value of 0.63 fT / $\sqrt{\text{Hz}}$ for a film of the same volume, bringing the ADFMR magnetometer's sensitivity in line with the best available SERF and SQUID magnetometers.

1/f noise (electrical)

A significant source of noise in existing solid-state magnetometers is electrical 1/f noise (that is, noise that increases in amplitude at low frequencies). In many competing sensor technologies, the need for charge transport (a current) to read out the state variable of the sensor can contribute substantially to the overall noise profile. For example, trapping in the tunnelling oxide in MTJ-based sensors is a large contributor to this 1/f noise.[30]

As this system does not require any low-frequency excitation or bias, the impact of this 1/f noise is greatly diminished. In MTJ sensors, for example, the 1/f noise contribution falls below the thermal noise above operating frequencies in the range of 100's of kHz.[3] All excitation in the ADFMR system occurs at the resonant frequency of the sensor (GHz) and thus there should be no observable contribution from 1/f noise to the overall noise of the system.

1/f noise (magnetic)

The root of magnetic 1/f noise (or Barkhausen noise) is the random flipping of magnetic domains within the magnetic elements of solid-state magnetometers. Such noise is present in MTJ sensors[68] and other similar sensor configurations where the magnetic sensitivity requires a switching of a magnetic free layer. Barkhausen noise is one of the major limiting factors of the sensitivity of magnetoresistive sensors.

One advantage of our system in this respect is that no switching event is required in order to provide magnetic sensitivity. As such, it is possible to excite FMR and perform our readout when the magnet is in a saturated state. This results in the FMR precession being largely coherent, with no domain flipping. This eliminates the source of Barkhausen noise from our sensor, and therefore the effect of 1/f magnetic noise should be very small in these devices.

Power line noise

Power line noise can be a significant contributor to electrical noise in a system. In some cases, the signal at this frequency is large enough to use for energy harvesting to power devices.[100]. Such a strong signal would normally preclude sensing near the power line frequency of 60 Hz.

As our system operates in the GHz range, it is estimated that only very high harmonics of this power line signal would have the ability to couple into our electrical system. Due to the design of the SAW devices used for ADFMR, anything outside of a relatively narrow bandwidth around our designed excitation frequency is rejected. As a result, we expect noise due to power line interference to be minimal in these devices. In addition, since such noise would be common to both sensors in a gradiometric configuration, we expect that it could be easily filtered out for such applications.

Oven control current noise

Using Equation 4.1, we can determine the thermal current noise present in the heating element used to maintain a system temperature of 55 °C. This noise current comes to ≈ 1.35 pA / $\sqrt{\text{Hz}}$ for a 10 kΩ resistive heating element. Assuming this element is located on the other side of the lithium niobate substrate from the magnetic thin film (as shown in Figure 4.2) 500 μm from the magnetic sensing element, this noise current translates to a magnetic

field noise of 0.54 fT / $\sqrt{\text{Hz}}$. Since this noise field should affect both gradiometric elements symmetrically, it should be amenable to common-mode rejection techniques.

Temperature effects on ADFMR magnetometry

The goal of the oven control circuit used in the ADFMR system is to keep the sensor package at 55°C±0.1°C and to maintain a temperature gradient over the sample below 0.01°C. It was shown in section 4.3 that the sensitivity of 0.1 W/T remains within ±5% of this value for a applied bias range of ≈ 5-10 Oe which is equivalent to a frequency range of 14-28 MHz ($\frac{\gamma}{2\pi}$B).

The temperature variation will affect both the piezoelectric and the ferromagnet. Assuming a typical SAW frequency shift of 70 ppm/°C (as is observed in lithium niobate devices [104], the frequency shift in the piezoelectric for a 0.1°C temperature change is ≈ 7 kHz for a resonance frequency of 1 GHz, well within the range where the sensor linearity is retained.

The main effect of temperature on the magnet comes through the change in saturation magnetization M_s. It is possible to express the shift in frequency due to variations in M_s as:

$$\Delta f = \frac{1}{4\pi}\omega_0 \left| \left[1 - \frac{M(T_1 = 55 \pm 0.1)}{M(T_2 = 55)} \right] \right| \tag{4.3}$$

Where Δf is the frequency shift and ω_0 is the unperturbed resonance frequency (assumed to be 1 GHz in this case). When $T/T_c < 0.3$ (T_c is the Curie temperature of the magnet), M(T1)/M(T2) can be simply described by $(T_1/T_2)^{3/2}$.[53] From here, Δf comes out to be ≈100kHz. Therefore, with oven control, changes in temperature should not create any issues in terms of loss of sensitivity due to shift in piezoelectric or ferromagnetic resonance frequency.

Chapter 5

Acoustically driven ferromagnetic resonance for antenna applications

One exciting application of acoustically driven ferromagnetic resonance is to use it to generate far field radiation. Previous work[6, 86, 70, 82, 23] has shown that ferromagnets undergoing resonance produce electromagnetic radiation as a damping mechanism. Traditionally, however, using FMR as an antenna has been untenable due to the extremely low efficiency (<1%) of existing FMR excitation methods. By leveraging the extremely large absorption seen in ADFMR devices, however, it may be possible to create antennas that are much smaller than what can be achieved using existing technology.

Section 5.1 of this chapter discusses the problems with creating efficient electrically small antennas. Section 5.2 discusses the mechanism of operation of ADFMR-based (or more generally, magnetic) antenna technologies - the oscillation of magnetic dipoles. Some examples of such magnetic antenna technology are discussed in Section 5.3. Finally, section 5.4 will discuss the complications caused by using a spatially inhomogeneous driving field (as is the case in our SAW geometry).

5.1 Electrically small antennas

Conventional antennas (like those found in your car, cell phone, or radio) are fundamentally resonant structures tuned to the free space wavelength of the electromagnetic radiation they seek to emit. As technology and understanding of the field has improved over the last $\approx$ 100 years, antenna designs have moved from simple wire structures to more complex horns, helixes, and apertures, but the primary operating principle has remained the same.[5]

Due to their resonant nature, it becomes difficult to design antenna structures that are substantially smaller than their operating wavelength. This is a problem of substantial technological significance, as antenna miniaturization has near-countless applications in commercial, industrial, and military fields (ie. shrinking cell phones, drone and missile communications, GPS integration, etc.). The difficulties of such miniaturization have been

investigated in detail by Lan Jen Chu[15], who originated the performance bound of the Q factor (stored power / radiated power) of such small antennas. Combined with the work done by Wheeler[113] and Harrington[39], this led to the development of the Chu-Harrington lower limit for radiation Q in a small, lossless antenna:

$$Q \geq \frac{1}{k^3 a^3} + \frac{1}{ka} \tag{5.1}$$

Where Q is the antenna Q-factor, $k = 2\pi/\lambda$ is the free-space wavevector of the radiation at the antenna operating frequency, and a is the radius of the smallest sphere than can enclose the antenna structure. For the purposes of this relation, an antenna is considered sufficiently small if $a < \lambda/2\pi$. This Q-factor is critical as it determines the maximum bandwidth for such an antenna by the relation:

$$\Delta f_{3dB} = \frac{f_0}{Q} \tag{5.2}$$

Where δf_{3dB} is the 3 dB bandwidth of the antenna, and f_0 is the antenna center frequency. This relation has held extremely well even into the modern era - conventional (that is - resonant, current driven) antennas have not been able to surpass the Chu-Harrington limit. An assortment antennas benchmarked against the Chu-Harrington limit can be found in Figure 5.1, showing that while some antennas have gotten close (excepting the one outlier value), as of 2010 no resonant antennas have been capable of surpassing this theoretical limit. Interestingly, as one approaches smaller values for the k*a product, the bandwidth*efficiency figure of merit falls ever further from the limit.

A further complication in real systems is encountered when one considers that antennas (and their corresponding matching networks) have some degree of Ohmic loss. Thus, for any antenna to be an efficient radiator, it needs to possess a radiation resistance (a conversion factor between radiated power and squared input current) substantially larger than its Ohmic resistance. In order to better realize the problem this poses for electrically small antennas, it is instructive to examine the radiation resistance of a short dipole.

In all electrically driven, resonant antenna structures, the radiated power is quantified by the Larmor formula,[61] which relates the acceleration of charged particles to their radiated power.

$$P_{rad} = \frac{q^2 a^2}{\epsilon_0 6\pi c^3} \tag{5.3}$$

Where P_{rad} is the radiated power, q is the particle charge, a is the particle acceleration, and c is the speed of light.

And the radiation resistance is defined as below:

$$P_{rad} = I^2 R_{rad} \tag{5.4}$$

Where I is the drive current of the antenna. This relationship can be simply derived for a dipole antenna using Equation 5.3 and the relation $qa = Il\omega$ when I takes the form

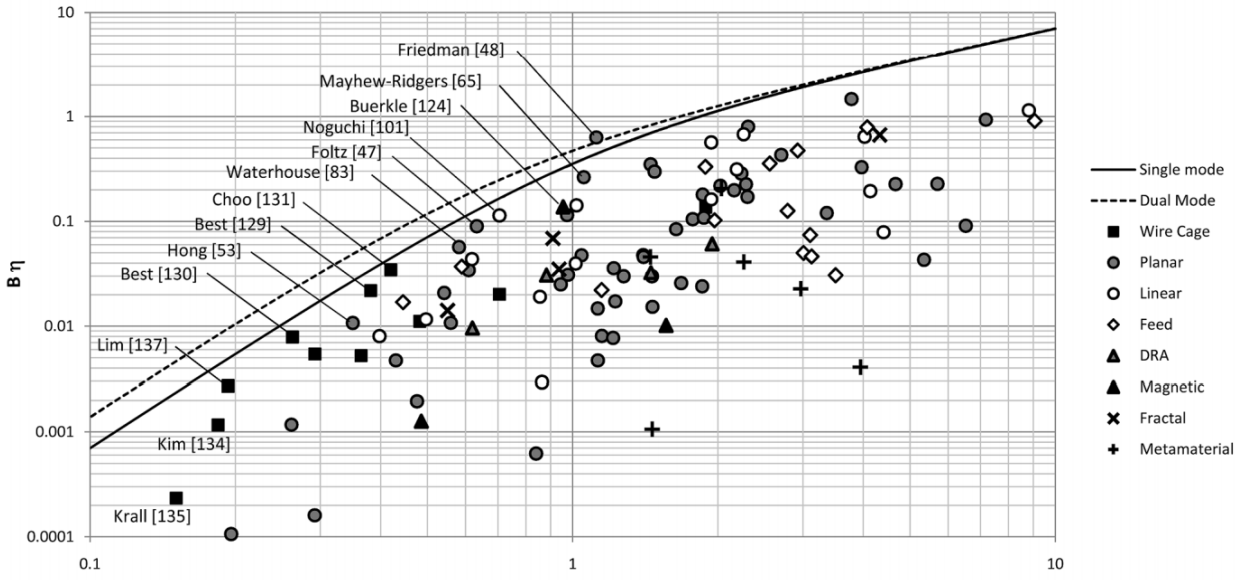

Figure 5.1: Bandwidth * Efficiency product as a function of k*a product for a wide variety of antenna geometries including results up to the year 2010. The additional restriction was made of limiting the antenna impedance such that the standing wave ratio (SWR) of a 50 Ω input feed did not rise above 2. As can be seen, aside from one published outlier value, conventional electrically small antennas have been unable to exceed the limitations proposed by Chu, Harrington, and Wheeler around the middle of the 20th century. This figure was reproduced from [92].

$I = I_0(1 - |x|/(l))cos(\omega t)$ and $2l$ is the length of the dipole. The current is estimated to decrease linearly as a function of position towards the ends of the antenna as the conductivity there goes to zero, and thus constrains that the current goes to zero. To simplify this linear dependence on position, we can simply replace the current by its average value as a function of position $I_a = I/2$. Plugging these values in gives:

$$P_{rad} = \frac{(I_a l\omega)^2}{6\pi\epsilon_0 c^3} = \frac{(Il\omega)^2}{24\pi\epsilon_0 c^3} = \frac{\omega^2 l^2}{24\pi\epsilon_0 c^3} I^2 = \frac{\pi}{6\epsilon_0 c}\left(\frac{l}{\lambda}\right)^2 I^2 \tag{5.5}$$

And consequently:

$$R_{rad} = \frac{\pi}{6\epsilon_0 c}\left(\frac{l}{\lambda}\right)^2 = \frac{\pi}{6}\eta\left(\frac{l}{\lambda}\right)^2 \tag{5.6}$$

Where $\eta \approx 377\Omega$ is the impedance of free space.

From this formula, it is then clear that when the antenna size is small compared to the signal wavelength that the radiation resistance can be dwarfed by ohmic losses in the antenna and its matching network. As an example, for a dipole with $l = \lambda/100$, we observe a

radiation resistance that is only $\approx 0.02\Omega$. As a result of these fundamental issues with regards to scaling of traditional antennas, a number of alternative systems have gained interest as potential replacements.

5.2 Radiation from an oscillating magnetic dipole

One mechanism that has been recently considered to overcome some of the fundamental issues inherent in traditional antennas is the use of magnetic materials. In these novel antenna structures, the oscillation of a magnetic dipole, as opposed to the oscillation of a charge current, is responsible for generating electromagnetic radiation. The time-invariant field created by a magnetic dipole is entirely magnetic in nature and can be written as:[73]

$$\mathbf{H_{dip}}(\mathbf{r}) = \frac{3\hat{\mathbf{r}}(\hat{\mathbf{r}} \cdot \mathbf{m}) - \mathbf{m}}{4\pi r^3} \tag{5.7}$$

Where $\mathbf{r}$ is the position vector of interest and $\mathbf{m}$ is the dipole vector. By using the relationship between the magnetic field and the magnetic vector potential ($\mathbf{B} = \nabla \times \mathbf{A}$)[73] we can establish a form for the magnetic vector potential that satisfies this relation. In addition, we can now incorporate a periodic oscillation of the dipole amplitude in order to obtain:

$$\mathbf{A_{dip}}(\mathbf{r}) = \mu_0 \nabla G(\mathbf{r}) \times \mathbf{m} \tag{5.8}$$

Where $G(\mathbf{r})$ is the Green's function:

$$G(\mathbf{r}) = \frac{e^{-jkr}}{4\pi r} \tag{5.9}$$

Where j is the imaginary number, k is the free-space wavevector of excitation frequency, and $r = \mathbf{r}|$. In this case, we also observe that the macroscopic scalar potential for this system can be set to zero, as the system does not necessarily have a net electric charge:

$$\phi = \frac{e^{-jkr}}{4\pi\epsilon r} \int_V \rho(\mathbf{r}) e^{jkr} d^3\mathbf{r} = 0 \tag{5.10}$$

Using the expressions for electric and magnetic fields from such potentials:

$$\mathbf{E} = -\nabla\phi - j\omega\mathbf{A} \tag{5.11}$$

$$\mathbf{H} = \frac{1}{\mu}\nabla \times \mathbf{A} \tag{5.12}$$

We can then plug in the expressions for ϕ and $\mathbf{A}$ from Equations 5.8 and 5.10 into Equations 5.11 and 5.12 to obtain:

$$\mathbf{E} = j\omega\mu_0 \nabla G(\mathbf{r}) \times \mathbf{m} \tag{5.13}$$

$$\mathbf{H} = \nabla \times [\nabla G(\mathbf{r}) \times \mathbf{m}] \tag{5.14}$$

Or more explicitly:

$$\mathbf{E} = j\omega\mu_0 \left(jk + \frac{1}{r}\right) (\hat{\mathbf{r}} \times \mathbf{m})\, G(\mathbf{r}) \tag{5.15}$$

$$\mathbf{H} = \left(jk + \frac{1}{r}\right) \left[\frac{3\hat{\mathbf{r}}(\hat{\mathbf{r}} \cdot \mathbf{m}) - \mathbf{m}}{r}\right] G(\mathbf{r}) + k^2 \hat{\mathbf{r}} \times (\mathbf{m} \times \hat{\mathbf{r}})\, G(\mathbf{r}) \tag{5.16}$$

Since we are then only interested in the radiation (or far-field) components of these fields, we eliminate all components that have a spatial attenuation greater than $1/r$ to obtain:

$$\mathbf{E}_{rad} = \eta_0 k^2 (\mathbf{m} \times \hat{\mathbf{r}}) \frac{e^{-jkr}}{4\pi r} \tag{5.17}$$

$$\mathbf{H}_{rad} = k^2 \hat{\mathbf{r}} \times (\mathbf{m} \times \hat{\mathbf{r}}) \frac{e^{-jkr}}{4\pi r} \tag{5.18}$$

Where $\eta_0 \approx 377\Omega$ is the impedance of free space.

We can thus observe that a time-varying magnetic dipole radiates electromagnetic fields into the far-field. Given that a rotating dipole can be represented by a combination of static and time-harmonic components, and that the static component has no far-field elements (as shown in Equation 5.7), a rotating dipole is then expected to be well-described by the above equations. This is the crux of the usage of magnetic dipoles for antennas, as rotating a magnetic dipole is often much simpler and more energy efficient than modulating its amplitude. As an example, magnets undergoing ferromagnetic resonance (as discussed in Section 2.1) fulfill the conditions described above and could be good candidates for magnetic antennas if an efficient driving mechanism (such as ADFMR) were to be utilized.

5.3 Multiferroic antennas

As we have seen in previous chapters, a strain field can generate effective magnetic fields within a magnetoelastic ferromagnet that are several orders of magnitude higher than if a similar amount of power were used to generate a magnetic field by flowing current through a stripline. Multiferroic antennas seek to leverage this efficient control of magnetism in order to rotate the magnetization of a ferromagnetic film. Through the mechanisms discussed in the previous section, such a rotation should allow for the generation of electromagnetic waves that propagate into the far-field.

Another circuit-level advantage of using such acoustically driven devices is that it is much simpler to obtain good impedance matching to a 50 Ω input feed with devices in the sub-mm size range. The effective 'radiation' (in this case acoustic, rather than electromagnetic)

resistance of such a device is dependent on the acoustic wavelength, rather than the electromagnetic wavelength for both surface[99] and bulk[29] acoustic wave geometries. Due to the fact that the speed sound in common piezoelectric materials is approximately 5 orders of magnitude lower than the speed of light in vacuum, a sufficiently large radiation resistance can be achieved in devices that are similarly 5 orders of magnitude smaller. This ability to match the resistance of the input feed without the need for a potentially complex (and lossy) matching network, in conjunction with the efficiency of the strain-based control of magnetism, makes such systems extremely attractive for antenna applications.

Substantial work has been done on modeling the behavior of such multiferroic antennas. The performance of such antennas has been rigorously modeled[119, 120] and has been found to be many orders of magnitude superior to traditional electrically-resonant antennas of a similar size. Recent experimental results[1] have also verified the accuracy of these models, not only showing that such structures emit measurable radiation, but that the measured radiation amplitude is many orders of magnitude greater than the radiation from a similarly sized electrically-resonant antenna.

All work on such multiferroic antennas, however, sidesteps the issue of magnetic resonance. The BAW antennas that have been experimentally fabricated (and that are the focus of modeling work) are all made to be mechanically resonant at the desired operation frequency in order to have a sufficiently large radiation resistance and to efficiently couple power into the antenna element. The energy transfer into the magnetic element, however, is non-resonant. The magnetic films are never driven into a resonance - they are simply driven into a forced oscillation at the mechanically resonant frequency, resulting in an inefficient conversion of mechanical power into magnetic precession. By developing structures that are both mechanically and magnetically resonant in overlapping conditions, it should be possible to further enhance the coupling between the magnetic and mechanical degrees of freedom - increasing radiation from the combined system.

5.4 Radiation from SAW devices

In order to model such a combined magneto-mechanical antenna system for realistic conditions (ie. magnetic films undergoing spin-wave resonance), one can no longer assume the film to behave as a single coherently oscillating dipole. Instead, the film must be broken into a set of many interacting dipoles distributed throughout space in order to capture the inhomogeneity of the system.

A simulation was performed to better understand radiation from such complex films - focusing specifically on the effects of periodic phase variation as a function of spatial position within the film. The film for all simulated cases has the following parameters: 100 dipoles along the x-direction, 20 dipoles along the y-direction, a dipole spacing of 1 nm, a precession frequency of 1 GHz, and a magnetization direction of 45 degrees from the x-axis, in-plane.

A slice of the radiated power taken in the z-plane 1 meter above the antenna can be found in Figure 5.2(a). Figure 5.2(a) shows the same film, but this time with a spatial phase

variation of λ=20 nm along the x-axis. There is a qualitative change in the appearance of the radiation patterns in these two cases from a single-lobed to a double-lobed pattern. In addition, it can be seen that the amplitude of the radiated power in the case with phase variation drops by many orders of magnitude compared to the uniform excitation mode. This drop in radiated power can be explained by the fact that two dipoles (viewed from the far field), when out of phase by 180 degrees, effectively cancel. In contrast, two dipoles that are entirely in phase will add.

This intuitive explanation can be regarded more rigorously by examining the full expression for far-field radiation for an oscillating magnetic dipole. First, consider the far-field equations for the E and H fields of an oscillating magnetic dipole from above, reproduced below:

$$E_{rad}(\mathbf{R}) = \eta_0 m_0 k^2 (\hat{\mathbf{m}} \times \hat{\mathbf{R}}) \frac{e^{-j(kR+\phi)}}{4\pi R} \tag{5.19}$$

$$H_{rad}(\mathbf{R}) = m_0 k^2 \hat{\mathbf{R}} \times (\hat{\mathbf{m}} \times \hat{\mathbf{R}}) \frac{e^{-j(kR+\phi)}}{4\pi R} \tag{5.20}$$

Where $\mathbf{R}$ is the vector represented by $\mathbf{R} = \mathbf{r} - \mathbf{r_0}$, where $\mathbf{r_0}$ is the dipole location, $\eta_0 \approx 377\Omega$ is the impedance of free space, k is the free-space wavevector of the radiation, ϕ is the initial phase of the dipole, $\mathbf{m_0}$ is the dipole strength, and $\hat{\mathbf{m}}$ is a unit vector in the direction of the dipole.

These equations can be used to calculate the Poynting vector $S = E \times H$ to obtain the power density from a rotating dipole, as shown in Equation 5.21.

$$P_{rad}(\mathbf{R}) = \eta_0 m_0^2 k^4 \frac{e^{-2j(kR+\phi)}}{16\pi^2 R^2} (\hat{\mathbf{m}} \times \hat{\mathbf{R}}) \times \hat{\mathbf{R}} \times (\hat{\mathbf{m}} \times \hat{\mathbf{R}}) \tag{5.21}$$

For the rest of this chapter, we will make the following substitutions for ease of comprehension:

$$A = \eta_0 m_0^2 k^4 \tag{5.22}$$

$$\hat{\mathbf{u}}(\mathbf{R}) = (\hat{\mathbf{m}} \times \hat{\mathbf{R}}) \times \hat{\mathbf{R}} \times (\hat{\mathbf{m}} \times \hat{\mathbf{R}}) \tag{5.23}$$

So that Equation 5.21 can be rewritten more simply as:

$$P_{rad}(\mathbf{R}) = A \frac{e^{-2j(kR+\phi)}}{16\pi^2 R^2} \hat{\mathbf{u}}(\mathbf{R}) \tag{5.24}$$

The simulated film, then, can be described by a summation of such dipoles, assuming all dipole amplitudes are identical:

$$P_{rad,total} = A \sum n \frac{e^{-2j(kR_n+\phi_n)}}{16\pi^2 R_n^2} \hat{\mathbf{u}}(\mathbf{R}) \tag{5.25}$$

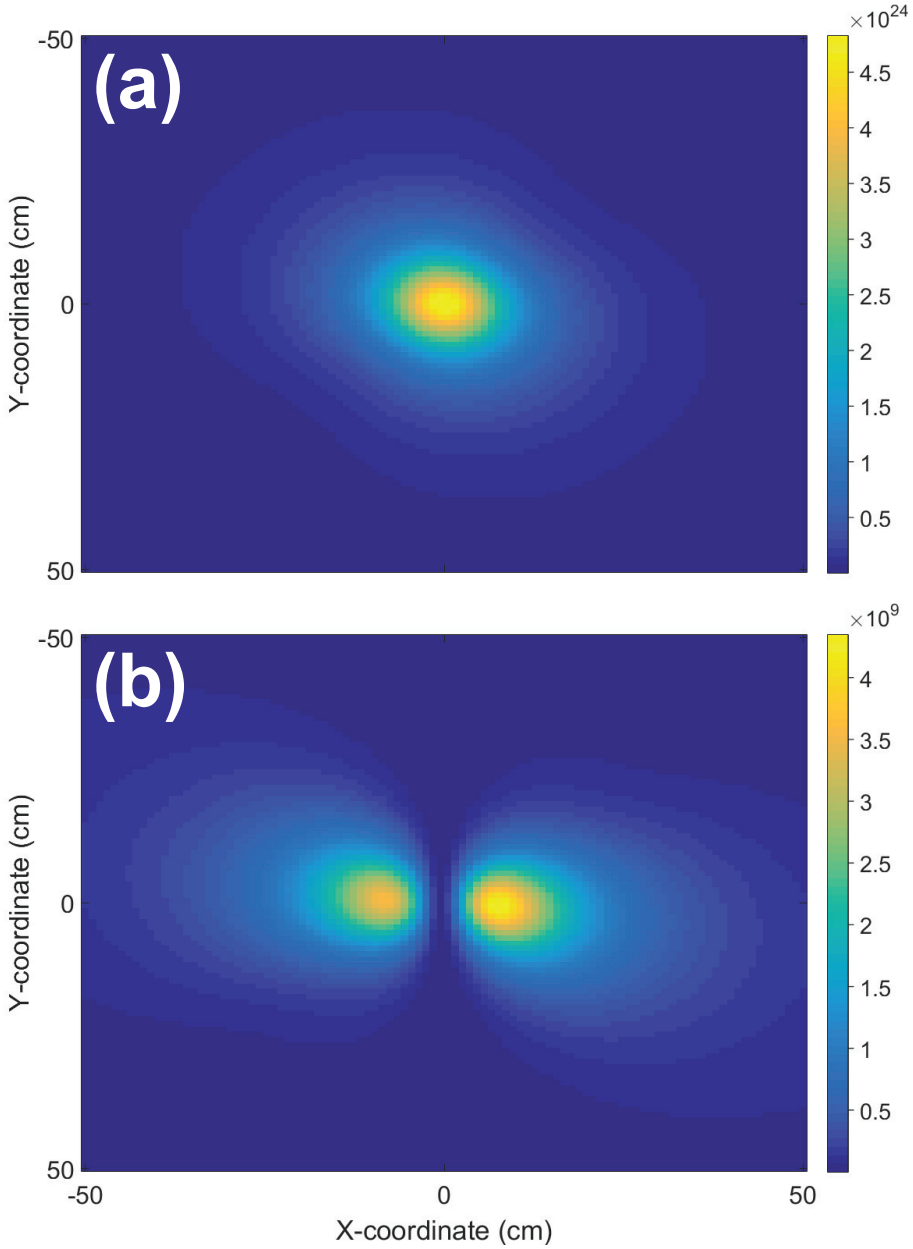

Figure 5.2: (a) Uniform-mode excitation of magnetic film. Cut taken along z-plane 1 meter from film. Color scale is radiated power density in arbitrary units. (b) Radiation pattern from spatially inhomogeneous magnetic film having a periodic phase shift with a period of 20 nm. Note both drastically reduced amplitude of radiation as well as qualitative shape change of radiation pattern. Cut taken along z-plane 1 meter from film. Color scale is radiated power density in arbitrary units. Unit scale is consistent across (a) and (b).

This expression can be simplified by restricting ourselves to the case where the maximum spacing between dipoles is much smaller than the radiation wavelength and we restrict ourselves to examining the far-field case. This corresponds well to the actual case of interest, as any proposed ADFMR antennas would be in the size range of 100 μm to 1 mm, and would operate at frequencies around 1 GHz (corresponding to a free-space wavelength of $\approx$ 30 cm). By doing so we can set $\hat{\mathbf{u}}(\mathbf{R}) \approx \hat{\mathbf{u}}$ and $R_n \approx r$ both inside and outside of the exponential.

$$P_{rad,total} = A\frac{e^{-2jkr}}{16\pi^2 r^2}\hat{\mathbf{u}}\sum ne^{-2j\phi_n} \tag{5.26}$$

It can be observed from the above equation the critical aspect to consider in maximizing the radiation amplitude is the summation of the dipole phases. Any periodic phase variation effectively eliminates all radiation from the device. This substantially restricts the usefulness of SAW-generated ADFMR as a method of generating far-field radiation, at least in the case of a continuous magnetic film.

In an effort to minimize this effect, which effectively reduces the film radiation power to zero, the magnetic film was patterned in order to reduce the destructive interference effect. Half of the film was removed such that only dipoles which had an initial phase of $-\pi/2$ to $\pi/2$ degrees were kept, while those dipoles that added destructively to the radiated signal were eliminated. This corresponds to physically cutting the film into equally sized and spaced strips along the direction of the spatial variation. The radiated power from this film can be seen in Figure 5.3, and, while the radiation pattern does not quite match the initial uniform-mode case, it is much closer both in magnitude and shape than the unpatterned case. Further work is underway to explore more complex patterns and their effects on the radiation pattern of the magnetic film.

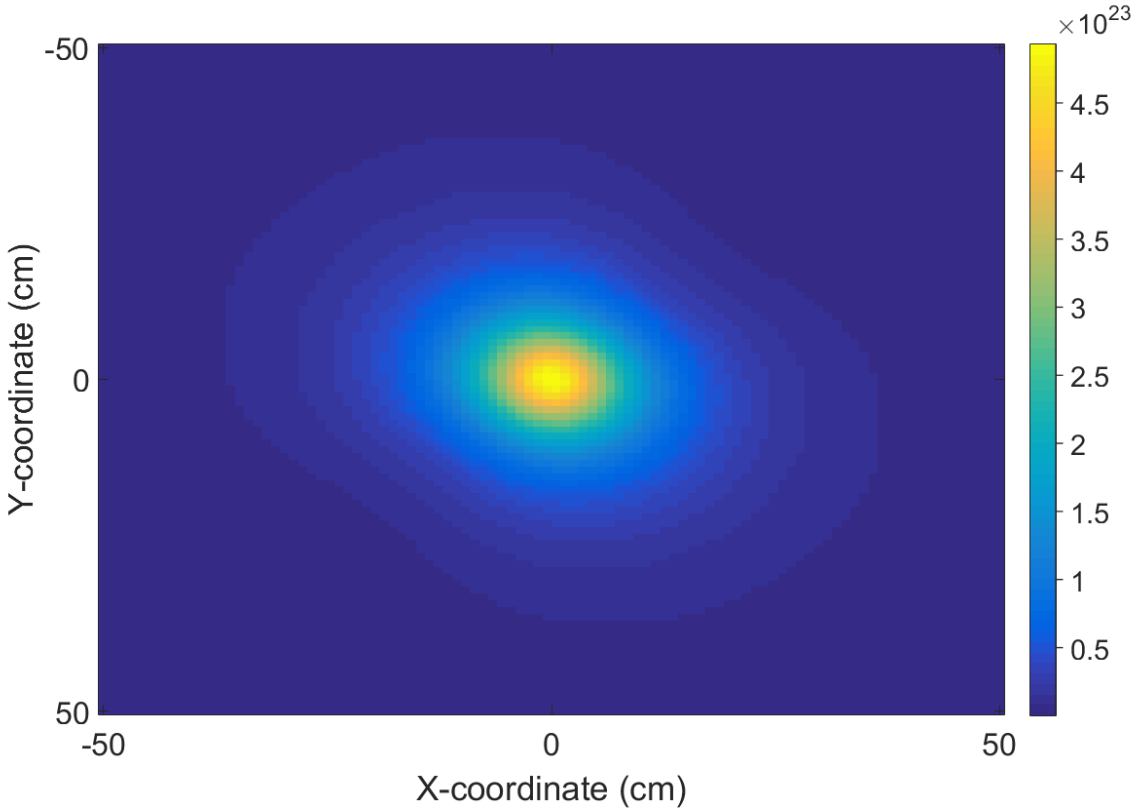

Figure 5.3: Film with the same spatial phase variation as shown in Figure 5.2(b), but with the film patterned such that only constructively interfering dipoles contribute to the final radiation pattern. Note similarity to Figure 5.2(a) in both shape and amplitude. Cut taken along z-plane 1 meter from film. Color scale is radiated power density in arbitrary units. Unit scale is consistent with Figure 5.2.

Chapter 6

Coupling acoustically driven ferromagnetic resonance with diamond nitrogen-vacancy centers

This chapter focuses on the work done in collaboration with researchers in the Hammel group at The Ohio State University in Columbus, Ohio. This work was inspired by two factors (1) the recent discovery of off-resonant coupling to nitrogen-vacancy (NV) centers in diamond via a proximal resonating ferromagnet[115, 116, 74, 28, 106] (2) the highly efficient coupling between SAWs and magnetic films that we have observed experimentally. The goal of this work was to show a coupling between the ADFMR and NV systems in the hope of using ADFMR as a driving (and potentially readout) mechanism for NV-center based devices. The rest of this chapter shows the results of our proof-of-concept work showing strong, off-resonant coupling in the NV centers when the ADFMR devices were undergoing resonance, in both nickel and cobalt films. We surprisingly observe similar NV coupling in both Ni and Co systems, despite the fact that the ADFMR absorption amplitude seen in Co is much smaller.

6.1 Nitrogen vacancy centers in diamond

Nitrogen vacancy (NV) centers in diamond have gained attention for a number of promising applications, especially for high sensitivity and high resolution magnetic sensing[85, 43]. They have also shown promise as temperature sensors[57], single photon sources[2], and quantum computers[117]. Beyond these quantities, NV centers have also been proposed as strain[67] and pressure[25] sensors. This wide range of applications is at heart due to their ability to exist as a quantum defect at room temperatures, with observed dephasing times as long as 2 ms[50]. The intrinsically narrow linewidth of the NV center makes it extremely effective as a sensor of various external factors.

The widespread use and study of NV centers is in large part due to the ease of initialization

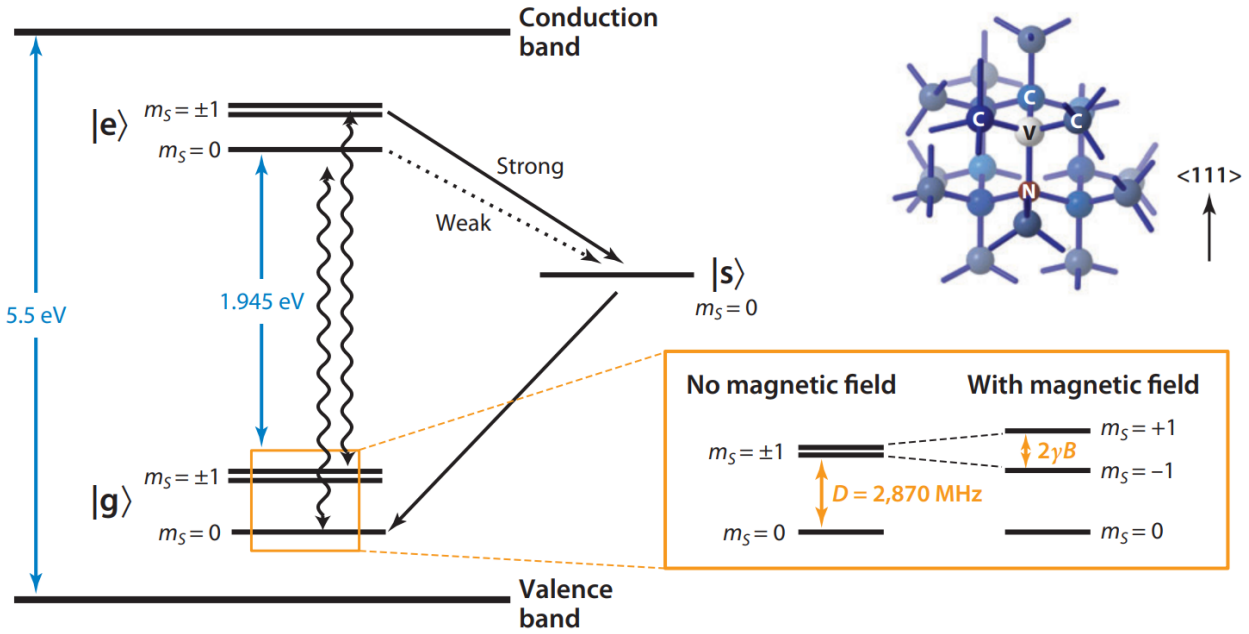

Figure 6.1: Schematic of the energy levels in a nitrogen vacancy defect center in diamond. Microwave photons at 2.87 GHz are capable of switching the defect spin state between $m_s = 0$ and $m_s = \pm 1$, with the frequency splitting between the magnetic states set by the amplitude of an applie external magnetic field. Figure adapted from [88].

/ readout of such defect centers using optical techniques. Figure 6.1 shows an energy level diagram of an NV center in a diamond lattice. An photon with an energy greater than 1.945 eV is capable of exciting an electron into the NV excited state. For the $m_s = 0$ state, relaxation is direct through the emission of a single photon. For the $m_s = \pm 1$ state, however, there is a strong coupling to an intermediate state such that the relaxation process emits two photons. Thus, by looking at the florescence intensity at ≈ 1.945 eV, it is possible to differentiate the two spin states of this system.[88]

The optical preparation of an NV center is similarly straightforward. The application of an off-resonance optical pulse (that is, one with a larger energy than that between the excited and ground state) is able to set the spin state via optical spin polarization.[40, 26] The simplicity of this combined initialization / readout scheme, along with the sensitivity of the defect to a variety of different parameters, has made this system extremely attractive to study.

One particularly fascinating development with regards to the study of nitrogen vacancy centers in diamond has been the discovery of off-resonant coupling between NV centers and a ferromagnet undergoing resonance.[115, 116, 74, 28, 106] This coupling between FMR and NV centers opens the path for coupling these extremely sensitive and scientifically interesting defects to our ADFMR system. By leveraging the strong coupling observed between these systems, and the high efficiency of ADFMR excitation, we hope to be able to enable an

on-chip, low-power method for efficiently controlling the NV center spin state electrically. Such a coupling could also potentially be used for readout, thus serving as an all-electrical means of manipulating and interrogating NV centers in diamond.

6.2 Experimental observation of coupling to diamond nitrogen vacancy centers

As the development of device applications for diamond NV centers progresses, it becomes increasingly important to enable the miniaturization and precise control of NV centers in order to allow for the fabrication of systems within the size and power constraints required for widespread adoption. We combine off-resonant coupling to nitrogen vacancy centers via a proximal resonating ferromagnet with acoustically driven ferromagnetic resonance (ADFMR). This combination allows for not only an increase in the fundamental understanding of both systems, but also enables the off-resonant drive of NV centers with zero applied field in an on-chip environment.

Nitrogen vacancy centers have been successfully used to probe local magnetic fields with nanoscale resolution[85, 43]. In this combined system, NV centers can serve as sub-micron probes of the acoustic-ferromagnetic coupling that lies at the heart of ADFMR (which, as an electrical transmission measurement, lacks local readout capability). We leverage this ability to measure local power intensity in our ADFMR systems and observe a similar absorption dependence as seen in previous work[58] and as predicted by existing theory[35, 112]. Such a spatially-resolved measurement scheme may allow for a better understanding of currently unexplained phenomena in ADFMR devices, such as the reduced absorption observed in cobalt compared to nickel (despite the fact that existing formulas for power absorption in these systems indicate that the opposite should be true[34, 111]).

Acoustically driven ferromagnetic resonance can also serve as a useful platform on which to study off-resonant excitation of diamond NV centers. Previous work has shown a coupling between the precessing magnetization of a ferromagnet in resonance and a proximal nitrogen vacancy center[115, 116, 74, 28, 106]. It has been proposed that the optical excitation of the NV centers is caused by spin waves that decay from the uniform FMR mode[74]. Due to the nature of the strain-based excitation mechanism, the spin waves generated in ADFMR match the wave vector of the traveling surface acoustic waves (SAWs), allowing for precise and tunable control of the wave vector in these systems[35]. This control allows for the generation of precise spin wave vectors that can be used to study the nature of the NV-FMR coupling.

We have used the sensitivity of nitrogen vacancy centers in diamond to dynamic magnetization changes in order to detect acoustically driven ferromagnetic resonance. We have observed comparable NV florescence signals from both cobalt and nickel films, despite the large variations observed in the SAW absorption amplitudes. The optical signal was measured at different spatial locations at a variety of excitation frequencies, and the values obtained from

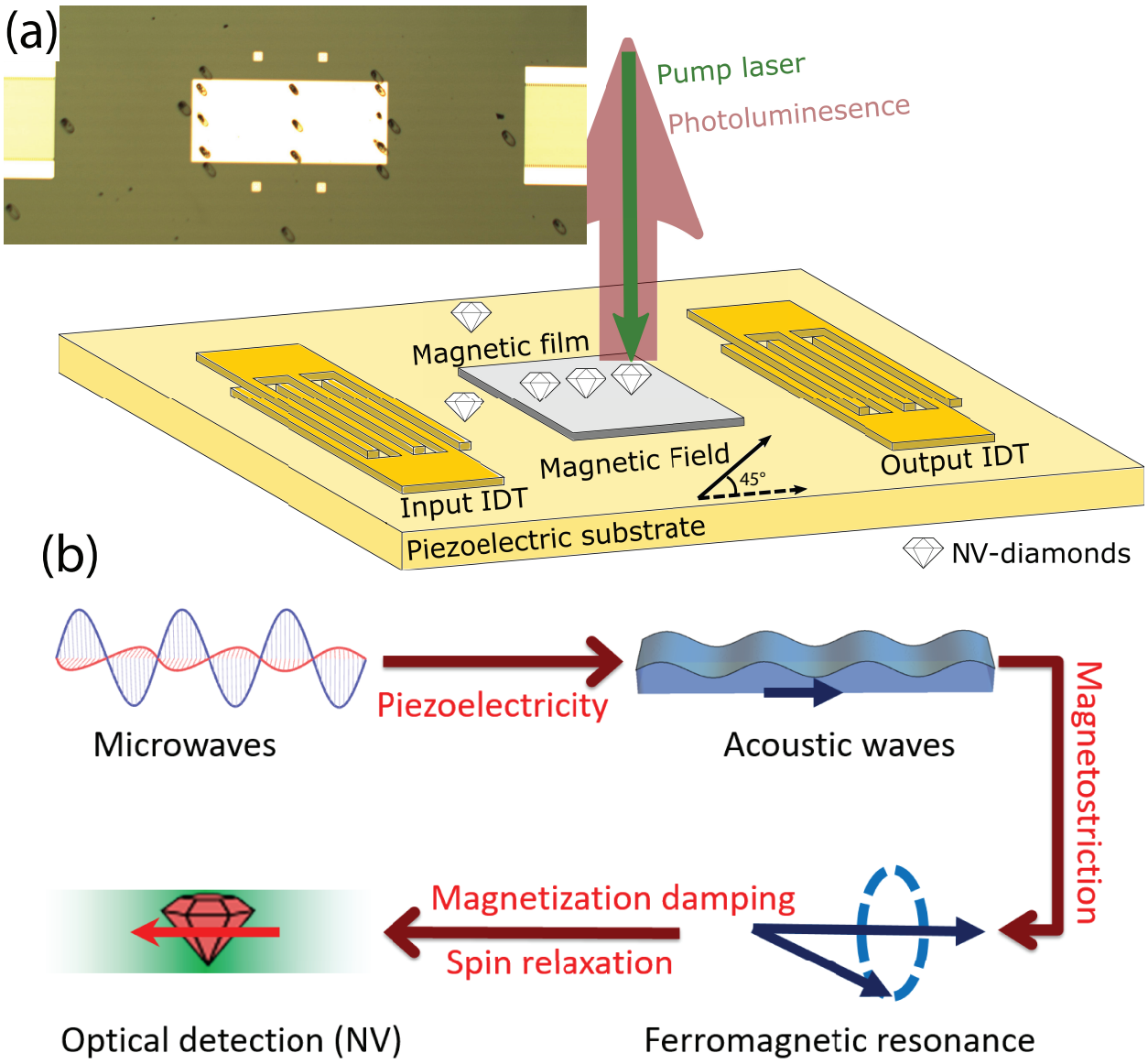

Figure 6.2: (a) Schematic diagram of experimental sample and optical excitation / detection scheme. Inset photograph of measured device shows interdigitated transducers (IDTs) and the magnetoelastic film. Dark spots on pad and substrate are clusters of nanodiamonds. The magnetic field was applied at 45° in-plane from the SAW propagation direction for all measurements. (b) Diagram of energy flow in the system, showing transduction methods between the different components of the sample.

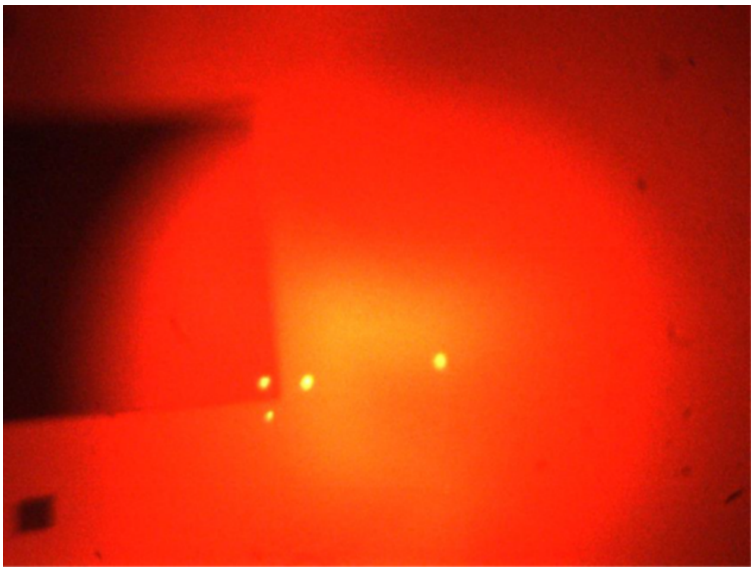

Figure 6.3: Photolumiescence image of nanodiamond dots deposited on an ADFMR device. The dark rectangle on the left side of the image is the nickel pad shown in the center of the inset in Figure 6.2 above. The bright spots are clusters of nanodiamonds containing NV centers.

these measurements are in agreement with previous ADFMR absorption studies[].

A schematic diagram of the ADFMR sample with deposited nanodiamonds can be found in Figure 6.2(a). Acoustically driven ferromagnetic resonance operates on the principle that a time-varying strain wave can alter the magnetocrystalline anisotropy of a magnetoelastic ferromagnet to generate an effective magnetic field internal to the magnet. This effective field is capable of driving the system into FMR. The effect is quantified by measuring the attenuation of the traveling acoustic wave. A more detailed explanation of this phenomenon can be found in existing literature[58, 112, 35, 27].

Commercial nanodiamonds containing NV centers (Adámas Nanotechnologies) were deposited on an ADFMR device using a micropipette. Nanodiamonds were deposited in a variety of locations on the sample in order to determine the spatial dependence of the off-resonant coupling in the ADFMR-NV system. A photoluminescence image of the nanodiamonds on the ADFMR sample can be seen in Figure 6.3. A confocal microscopy setup was utilized to excite the NV centers and read out the photoluminescence (PL) intensity. All measurements in this work were performed with the external bias field oriented at 45° in-plane from the SAW propagation direction.

Figure 6.2(b) shows the various steps of energy transduction with the ADFMR-NV system. An incident microwave voltage is first applied to the IDT electrodes where it is converted into a surface acoustic wave via the piezoelectric effect. This time-varying strain is then converted into a magnetization perturbation by the Villari effect, driving the magnetoelastic film into ferromagnetic resonance[111]. This oscillating magnetization then couples

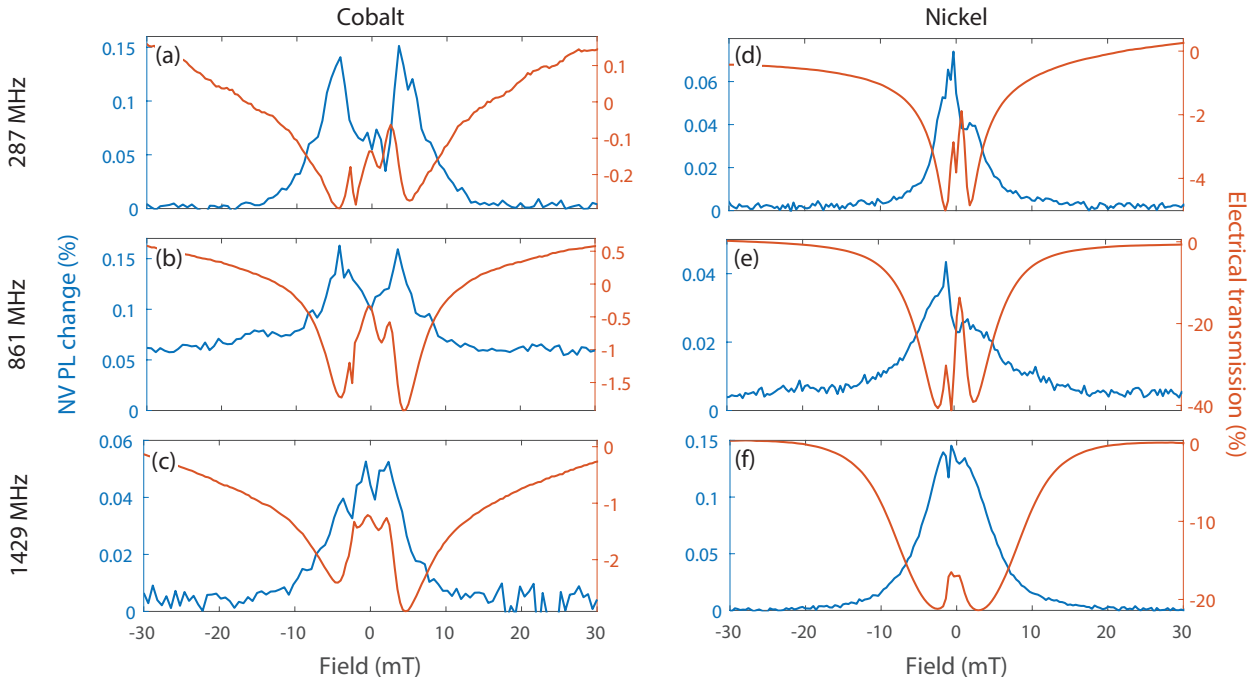

Figure 6.4: Microwave power absorption and NV PL change as a function of magnetic field in nickel and cobalt samples. The drive frequency for the ADFMR devices was set to the first, third, and fifth harmonics of the IDTs for these measurements. A clear correlation between power absorption and NV PL change can be observed. This figure was adapted from the work of Nicole Guo[37].

into the nitrogen-vacancy defect centers in the deposited nanodiamonds, altering their photoluminescence intensity. Finally, this change in photoluminescence intensity is measured to quantify the effect.

Measurements of the power absorption by the ferromagnetic film and the nitrogen vacancy center PL change (with respect to the photoluminescence intensity with the microwave excitation switched off) can be found in Figure 6.4. These measurements were carried out for both nickel and cobalt films, and were performed at the 1st, 3rd, and 5th harmonics of the IDTs. A strong correlation between the power absorption and NV PL change can be observed, with the NV center PL change peaking when the RF power absorption by the RF element is highest. While the absorption is lower for the cobalt films when compared to nickel, the change in NV PL is higher. This unexpected result emphasizes the usefulness of the study of this coupled system in understanding the underlying physics behind ADFMR. In addition, a strong photoluminescence intensity change at zero applied field can be seen in both cobalt and nickel at all tested frequencies. This observation reinforces the effectiveness of using ADFMR as a driving mechanism for NV device applications, as it allows for broadband coupling into the NV center without the need for an external field source.

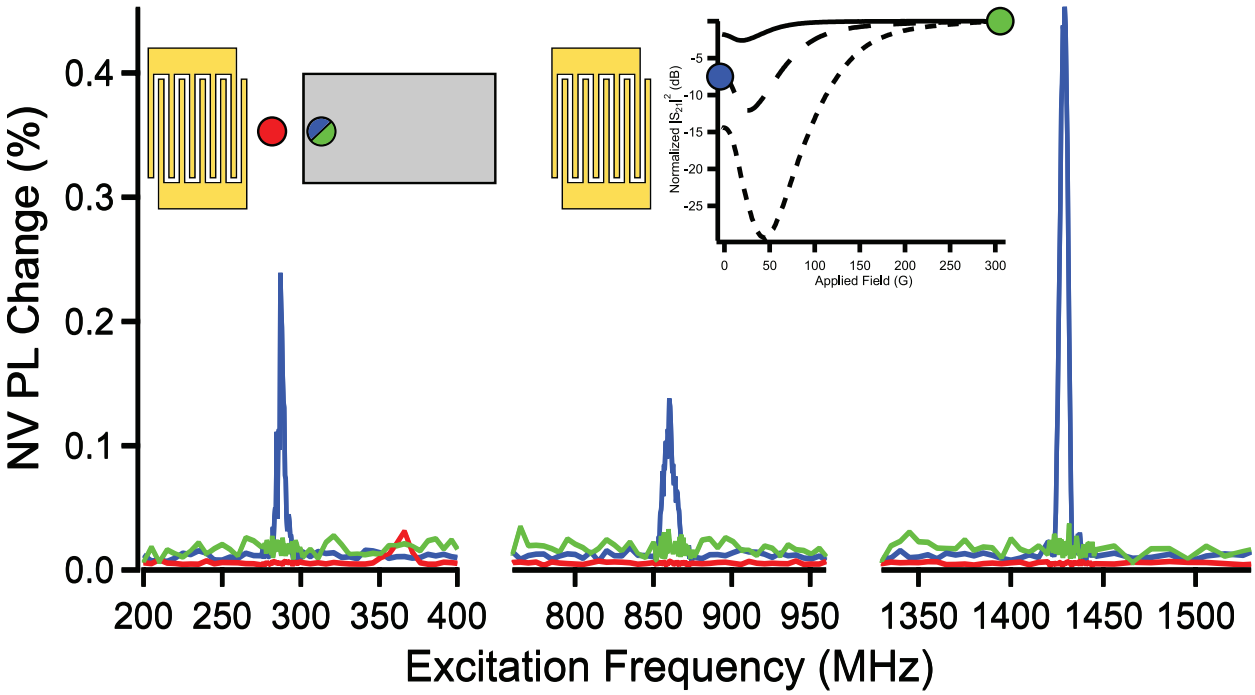

Figure 6.5: Change in NV center photoluminescence normalized to the DC level for nanodiamonds both on and off the ferromagnetic pad. NV centers located off the ferromagnetic pad (red) and NV centers on the pad with a high (35.8 mT) applied bias field (green) show no change in PL. Only NV centers on the pad with 0 applied bias field (blue) show a notable photoluminescence change. The peaks in the NV center signal align with the first, third and fifth harmonics of the IDTs. All measured NV PL change outside of the shown frequency range is below 0.03%. Left inset shows a schematic of the color / position of the NV centers, while the right inset shows the field-dependence of the ADFMR absorption.

In order to verify that the observed PL change is due to off-resonant coupling with the ferromagnetic film, the photoluminescence is measured as a function of excitation frequency and location. Figure 6.5 shows the change in NV center PL as a function of excitation frequency for three sets of conditions: NV centers on the ferromagnetic pad at 0 bias field (blue), on the ferromagnetic pad at 35.8mT bias field (green), and off the ferromagnetic pad at 0 bias field (red). As can be seen, a change in the NV enter photoluminescence is only observed at the resonant frequencies of the IDT (287, 861, and 1429 MHz), on the ferromagnetic pad, and with 0 applied bias field (as seen in Figure 6.4 and in the inset, ADFMR absorption and NV PL change both approach 0 at high applied fields). This measurement serves to verify that the observed excitation of the nitrogen vacancy centers in indeed due to off-resonant coupling via the ferromagnetic film and not due to spurious electromagnetic signals from the IDTs.

We are able to measure this power absorption in a spatially resolved manner via the NV

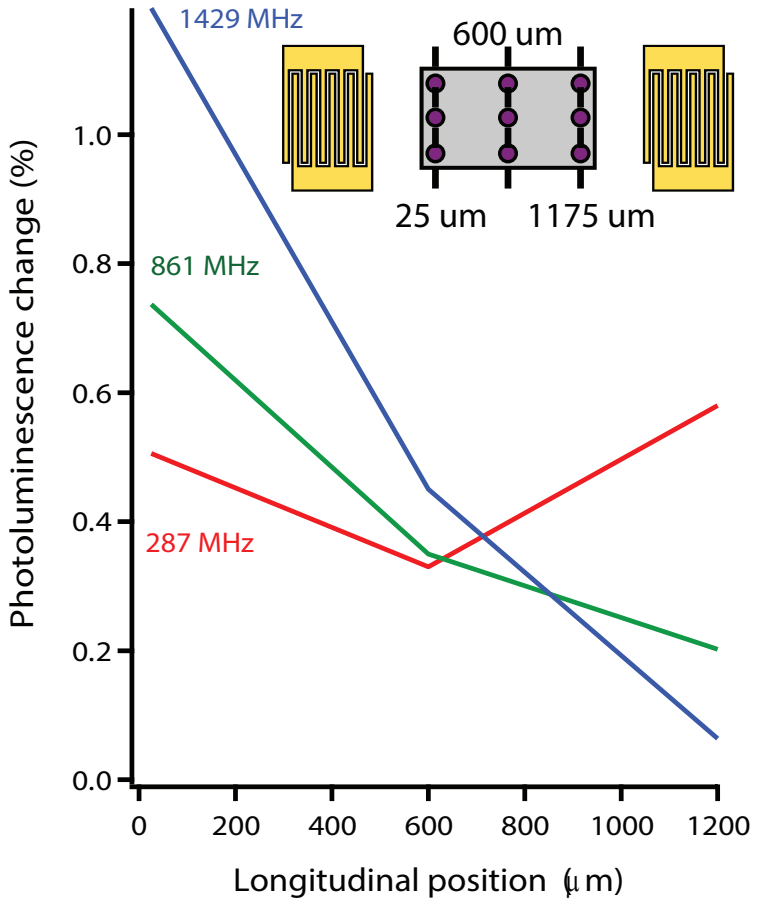

Figure 6.6: NV PL change as a function of spatial position in a 20 nm nickel sample. The drive frequency for the ADFMR devices was set to the 1st, 3rd, and 5th harmonics of the IDTs for these measurements. The dependence of the signal amplitude on frequency and position is corroborated by previous absorption measurements on ADFMR devices.

center photoluminesence. Figure 6.6 shows NV PL change as a function of spatial position along the nickel element at zero applied magnetic field. All distance values are measured from the pad edge closest to the excitation IDT (see inset). The plotted data is an average of three spots that are the same distance from the edge of the nickel pad in an effor to help reduce the effect of inhomogeneity between the different nanodiamond spots. These direct spatial measurements performed via coupling to NV centers are corroborated by previous ADFMR studies that show the same position[58] and frequency[58, 112, 35, 27] dependence.

This work has demonstrated the off-resonant coupling between acoustically driven ferromagnetic resonance and nitrogen vacancy centers in diamond. We observe this coupling at variety of excitation frequencies at zero applied field in both cobalt and nickel samples. NV centers are used to obtain spatially-resolved optical readout of the local properties of ADFMR devices, which can be leveraged to better understand the conversion of the time-

varying strain into ferromagnetic precession. The use of an acoustic driving field, on the other hand, allows for the excitation of specific spin wave vectors in ferromagnetic films[35], allowing for a more precise determination of the effect of wave vector on off-resonant coupling between diamond NV centers and ferromagnets undergoing resonance. Further study of this combined system will allow for a deeper understanding of both underlying elements, enabling the miniaturization of NV-center based systems for applications in sensing and quantum computation.

Chapter 7

Extraction of film damping and magnetoelastic coupling coefficient

Analysis of the experimentally collected data from Chapter 3 allows for the extraction of a number of device-relevant parameters. Section 7.1 describes how relevant material properties (saturation magnetization, effective magnetization, and in-plane anisotropy) were extracted for the films used in ADFMR experiments. These quantities were critical for accurately fitting the data using the formalism developed by Gowtham et. al. [35] A discussion of this fitting and the extraction of the film damping parameter can be found in Section 7.2. In conjunction with the damping parameter, a careful characterization of input power and film properties allowed us to extract a quantitative value for the magnetoelastic coupling coefficient in these films as discussed in Section 7.3.

7.1 Measurement of magnetic properties

In order to perform the coefficient extractions shown later in this chapter, it was necessary to carefully measure several material properties for the nickel films used. These properties were measured at each sample thickness, and the parameter extraction samples were deposited at the same time as the ADFMR samples in order to ensure that the film properties were as similar as possible. All parameter extraction samples were also deposited on the same Y-cut lithium niobate substrates as the ADFMR devices in order to further ensure similarity.

Multiple techniques were needed in order to extract the parameters required to use the coefficient extraction techniques described below. In-plane vibrating sample magnetometer (VSM) scans were performed in order to obtain the saturation magnetization of the nickel films (as the films have an easy plane in-plane). Out-of-plane VSM scans were then performed in order to extract the effective magnetization of the films. Finally, Anisotropic Magnetoresistance (AMR) scans were performed on resistor structures integrated into the ADFMR devices in order to extract the in-plane anisotropy energy and thus determine the effective in-plane anisotropy field.

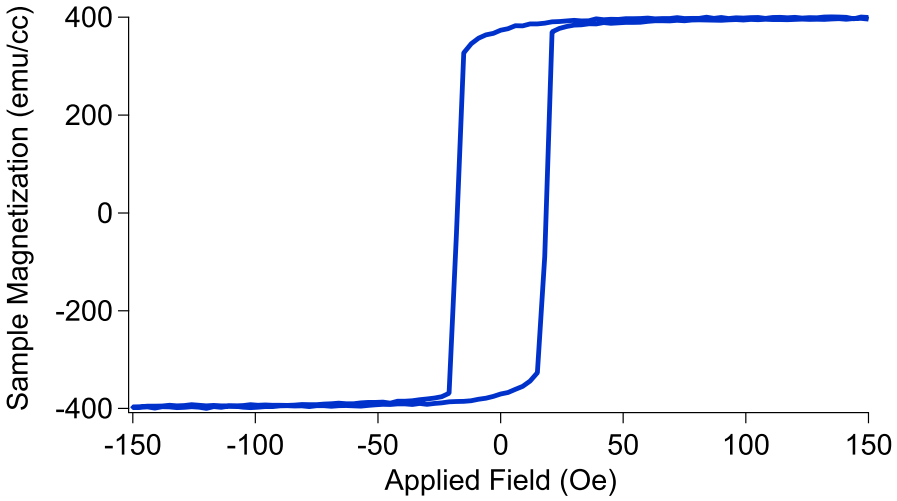

Figure 7.1: In-plane VSM scan plotted as an M-H curve for a 40 nm thick Ni film on lithium niobate with a 5 nm gold capping layer with sample magnetization in emu/cc on the y-axis and applied magnetic field in Oerstead on the x-axis. The saturating value seen at high positive and negative fields (above $\approx$ 25 Oe) is the saturation magnetization of the film - approximately 400 emu / cc for this sample.

Saturation magnetization

Saturation magnetization of the nickel films used in these experiments was performed by measuring M-H (magnetization vs. field) curves in an in-plane configuration by using a VSM. M_s was extracted in-plane as nickel films in this thickness range naturally assume an in-plane easy plane. A plot of an exemplary M-H curve for a 40 nm thick nickel film can be found in Fig. 7.1. The saturation value of the magnetization at high field is taken to be the saturation magnetization of the film.

Effective magnetization

Effective magnetization of the nickel films is a measure of the anisotropy energy forcing the film in-plane. The equation relating effective magnetization and perpendicular anisotropy energy can be found in Eq. 7.1. The effective magnetization can be extracted from an out-of-plane M-H curve from a VSM scan by measuring the location of the inflection point as the sample magnetization approaches saturation. An exemplary out-of-plane M-H curve for a 40 nm nickel sample can be found in Figure 7.2.

$$M_{eff} = 4\pi M_s - \frac{2K_\perp}{M_s} \tag{7.1}$$

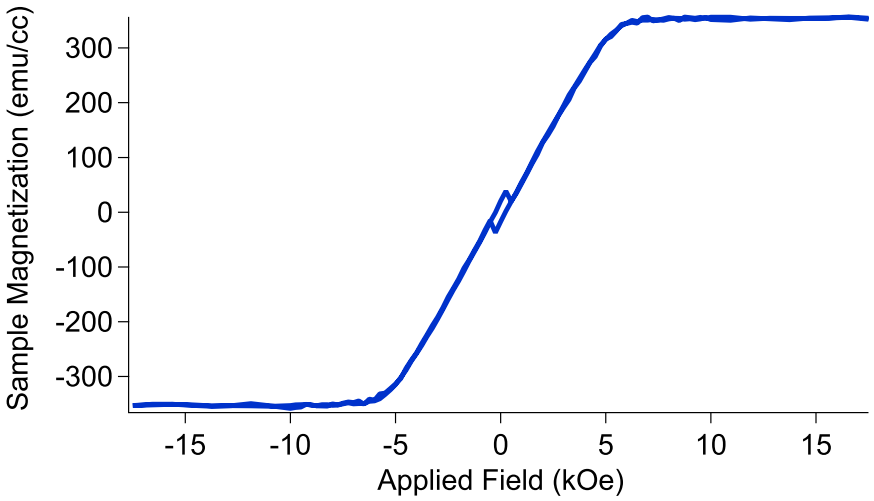

Figure 7.2: Out-of-plane VSM scan plotted as an M-H curve for a 40 nm thick Ni film on lithium niobate with a 5 nm gold capping layer with sample magnetization in emu/cc on the y-axis and applied magnetic field in Oerstead on the x-axis. The effective magnetization is extracted by measuring the field required to saturate the magnet out of plane as indicated by the inflection point as the sample nears saturation. The extracted value $4\pi M_{eff} \approx 6$ kOe for this sample.

In-plane magnetic anisotropy

The in-plane magnetic anisotropy of the nickel films used in these studies was characterized by performing anisotropic magnetoresistance measurements on resistor structures designed into the mask layer used to define the magnetic regions on the sample. An optical micrograph showing a wirebonded AMR structure on a sample device can be found in Figure 7.3. While any method of measuring the field-dependence of magnetization as a function of in-plane bias field angle (such as VSM measurements) could be used to extract the in-plane anisotropy, AMR was chosen due to its ease of implementation in the available measurement setup. The VSM facilities available for these measurements did not have a programmable rotation stage, while the setup built for ADFMR did, thus motivating the use of a transport-based measurement method such as AMR.

A sample plot of the data obtained from an AMR scan at 90 degrees from the SAW propagation direction in a 40 nm nickel film can be found in Figure 7.4. The resistance of this structure varied as a function of film thickness, but remained between 30 and 150 Ohms for all device configurations. As can be seen in the plot, an AMR ratio of ≈ 0.3 % can be observed. This relatively low AMR ratio is attributed to the use of a 5 nm gold capping layer, which effectively shunts much of the current out of the nickel film and thus reduces the strength of the signal.

Once the AMR data was taken, the direction of maximum resistance change was deter-

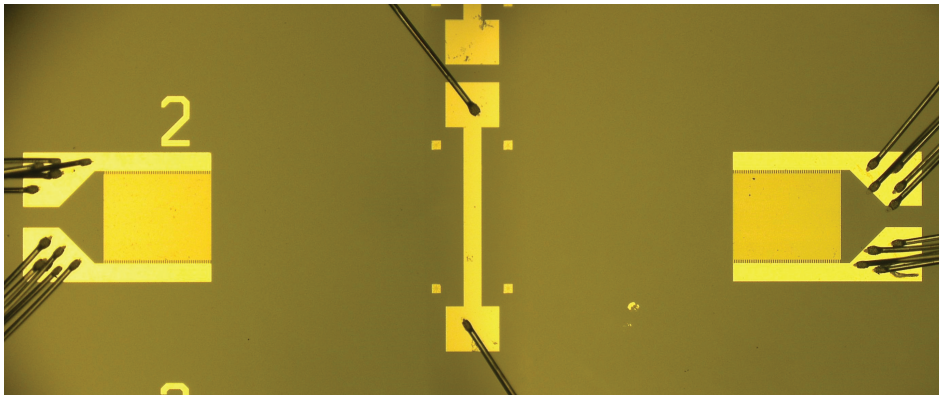

Figure 7.3: Picture of an exemplary device taken using optical microscopy. The AMR structure in the center of the sample has dimensions 0.1 x 1 mm, and the two IDTs have a center-to-center spacing of 3.5 mm. The AMR structure was wirebonded to the custom-built PCB sample holder to allow for measurements of AMR as a function of applied magnetic field and field angle.

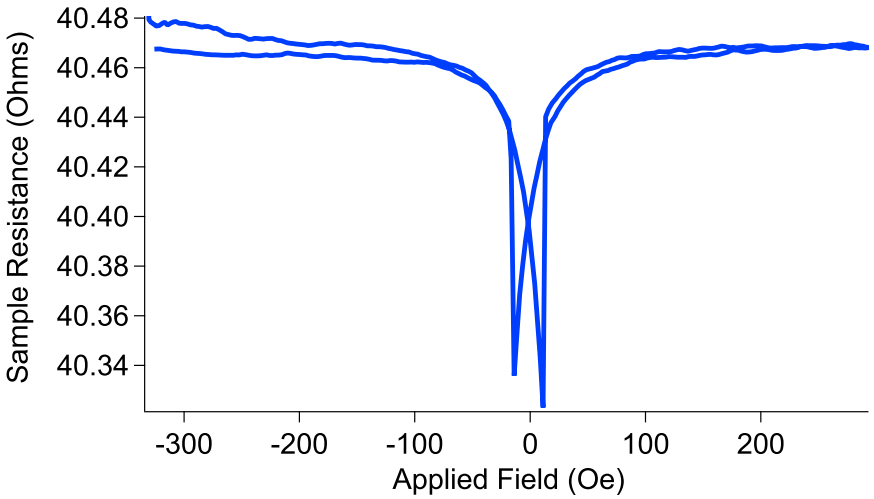

Figure 7.4: Plot of data taken from a typical AMR scan at a single angular point. Measured device resistance is on the y-axis, and applied magnetic field is on the x-axis. The change in resistance as a function of field is indicative of the magnetization of the sample.

mined. This angle was taken to indicate the orientation of the in-plane anisotropy. As the resistance in these AMR scans can be taken as an analogue of magnetization, the resistance vs. applied field curve shown in Figure 7.4 was converted into a normalized magnetization vs. applied field curve as seen in Figure 7.5.

In order to obtain the anisotropy energy from these magnetization vs. field plots, the region between the x-axis and the curve was integrated as shown by the green area in Figure

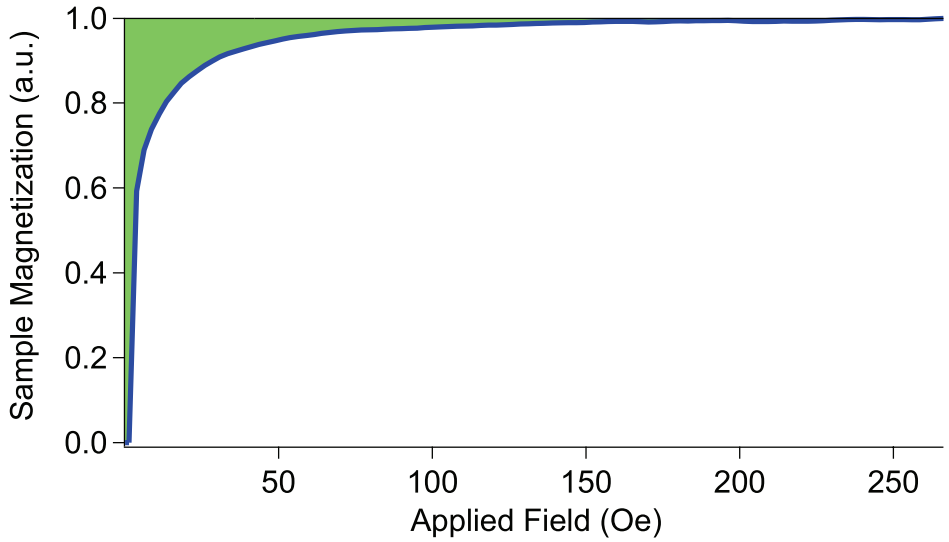

Figure 7.5: Plot of magnetization vs field extracted from the AMR scan shown in Fig. 7.4. The y-axis shows normalized magnetization along the direction of the applied field, with 0 indicating no magnetization component in that direction and 1 indicating that the magnet is saturated in that direction. The in-plane anisotropy energy of the film along the measured direction can be extracted by integrating the green shaded area.

Table 7.1: Film parameters used for extraction of film damping and magnetoelastic coupling coefficient

	H_k (Oe)	M_s (emu/cc)	M_{eff} (emu/cc)
10 nm	29.30	302.2	363.5
20 nm	19.58	340.9	437.9
30 nm	19.81	373.9	432.2
40 nm	33.58	405.7	465.4
50 nm	23.11	408.7	461.2

7.5. This value (given that the x-axis were in actual units of magnetization as opposed to being normalized) is the uniaxial anisotropy energy of the film K_u. In order to convert this energy into the anisotropy field value necessary to perform the calculations, it is divided by the sample magnetization and then multiplied by a factor of two.

A compilation of the extracted film parameters for each tested thickness can be found in Table 7.1 below. The only value not extracted directly is the exchange stiffness constant, A_{ex}, which was taken from literature.[72]

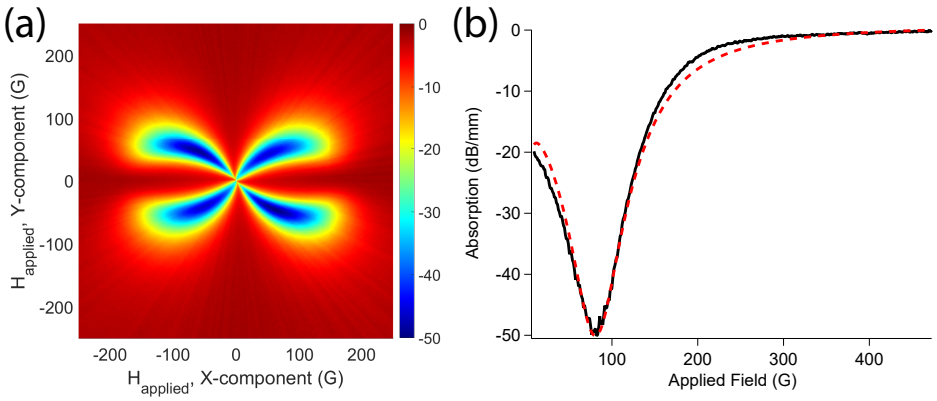

Figure 7.6: (a) Angular rotation scan collected on a 20 nm nickel film at 2565 MHz. The color bar indicates the power absorption in dB/mm. The x-component of the applied magnetic field is taken to be parallel to the direction of SAW propagation, and the y-component is in-plane and perpendicular to the direction of SAW propagation. (b) Line cut along the angle of highest absorption (35°) showing very good agreement between experimental data (black solid) and the analytical fit (red dashed).

7.2 Fitting of of damping coefficient

Scans of angular and field dependence were performed at a variety of frequencies over film thicknesses ranging from 10 nm to 50 nm. An example of such a scan can be found in Fig. 7.6(a). The four-fold symmetry that is a hallmark of the magnetoelastic drive is clearly visible. The extremely large magnetically-tunable absorption in these systems at relatively low frequencies ($>$ 70 dB/mm in a 50 nm thick Ni film at 2565 MHz) also distinguishes acoustically-driven ferromagnetic resonance from other ferromagnetic resonance measurement techniques where the absorption in these frequency ranges is several orders of magnitude lower.

The experimental data was fit using the formalism devised by Gowtham et. al [35] with the film damping Γ as a free parameter. Γ was extracted using a normalized absorption curve in order to remove any amplitude-related considerations from the fit, as the damping should be predominantly reflected by the shape of the curve as opposed to its amplitude. A comparison of the experimental data and the fit can be found in Fig. 7.6(b), showing extremely close agreement. The relevant equations for the fitting can be found below in Equations 7.2, 7.3, 7.4, and 7.5.

$$P_{abs} = \frac{\omega_p}{2M_s} Im\left\{\chi_{xx}\right\} \left(2B_{eff}\varepsilon_{xx}\right)^2 \cos(\phi_0)^2 \sin(\phi_0)^2 \tag{7.2}$$

$$Im\left\{\chi_{xx}\right\} = \frac{\frac{\omega_p}{\gamma}\Gamma\left(\mathbf{q}_{||},\mathbf{m_0}\right)\left(\Upsilon^2+\left(\frac{\omega_p}{\gamma}\right)^2\right)}{\left(\left(\frac{\omega_{res}}{\gamma}\right)^2+\left(\frac{\omega_p}{\gamma}\right)^2\right)^2+\left(\frac{\omega_p\Gamma\left(\mathbf{q}_{||},\mathbf{m_0}\right)\left(\Psi+\Upsilon\right)}{\gamma}\right)^2} \tag{7.3}$$

$$\Psi = H_k\cos(2\phi_0)+H_{app}\sin(\phi_0+\upsilon_H)+\frac{2A_{ex}}{M_s}|q_{||}|^2+2\pi M_s|q_{||}|d\cos(2\phi_0)^2 \tag{7.4}$$

$$\Upsilon = H_k\cos(\phi_0)^2+H_{app}\sin(\phi_0+\upsilon_H)+\frac{2A_{ex}}{M_s}|q_{||}|^2+\left(4\pi M_s-\frac{2K_\perp}{M_s}\right)-4\pi M_s\left(\frac{|q_{||}|d}{2}\right) \tag{7.5}$$

Where ω_p is the IDT excitation frequency, B_{eff} is the magnetoelastic coupling coefficient, ε_{xx} is the strain along the SAW propagation direction, M_s is the saturation magnetization of the film, ϕ_0 is the magnetization angle with respect to the axis in plane and perpendicular to the SAW propagation direction, γ is the gyromagnetic ratio, Γ is the film damping (a function of the SAW wave vector $q_{||}$ and the sample magnetization m_0), ω_{res} is the FMR frequency of the film, H_k is the effective in-plane anisotropy field, H_{app} is the applied magnetic field, υ_H is the applied field angle, A_ex is the exchange stiffness constant of the film, d is the film thickness, and $M_{eff} = 4\pi M_s - \frac{2K_\perp}{M_s}$.

The extracted values for damping in these films can be seen in Fig 7.7. These values are substantially larger than literature values for nickel damping in films of these thicknesses. [109] This increased damping agrees well with previous work on acoustically driven ferromagnetic resonance.[27, 35] This damping enhancement has been attributed to the inhomogeneity of the induced RF tickle field [27], and simulation has shown that this damping can be accounted for by introducing a spatially-varying spin pumping term.[62] A general trend of increasing damping with film thickness above $\approx$ 20 nm is observed in the data. We attribute this enhanced damping to the development of inhomogenieties and shear components within the magnet strain profile as the thickness is increased.

7.3 Extraction of magnetoelastic coupling coefficient

Derivation of relevant equations

Energy in magnetic fields

In order to calculate the magnetoelastic coefficient of the films used in the ADFMR experiments, it is first necessary to calculate the power of a magnetic field. To do this, we examine work done when charging an inductor.

$$\frac{dW}{dt} = -\varepsilon I \tag{7.6}$$

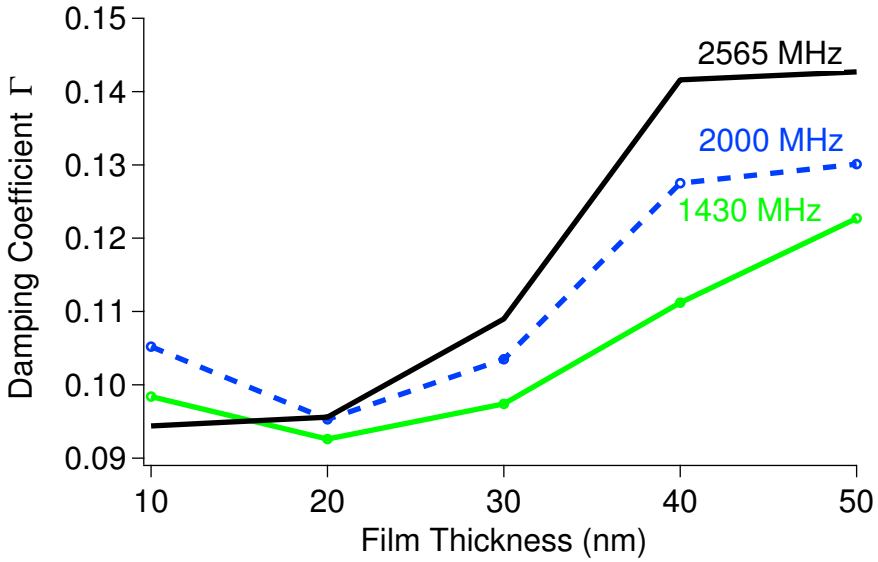

Figure 7.7: Extracted damping coefficient Γ as a function of film thickness for devices excited at 1430 (green solid), 2000 (blue dashed), and 2565 (black solid) MHz. A general trend of increased damping with increased film thickness can be observed. Substantially enhanced damping is observed at all frequencies, as has been noted in similar work. [27, 35]

Where W is work, I is current through the inductor, and ε is the work done on a unit charge due to back emf. As we know that in an inductor:

$$\varepsilon = L\frac{dI}{dt} \tag{7.7}$$

Where L is inductance, we can rewrite the above equation as:

$$\frac{dW}{dt} = LI\frac{dI}{dt} \tag{7.8}$$

Integrating from I=0 to I_0, we obtain:

$$W = \frac{1}{2}LI_0^2 \tag{7.9}$$

As we know magnetic flux through a loop (Φ) can be written as LI, we can use the fact that this flux can be written in the form of a surface integral of B (the magnetic field):

$$\Phi = \iint_S B \cdot dA \tag{7.10}$$

Combined with the fact that $B = \nabla \times A$ (where A is the magnetic vector potential), and Stokes theorem, we can then write:

$$W = \frac{1}{2} I \oint_c A \cdot dl = \frac{1}{2} \oint_c (A \cdot I) dl = \iiint_V A \cdot J dv \tag{7.11}$$

Where the rightmost expression allows us to generalize this work to the case of volume currents, and J is current density. To simplify notation going forward, the remainder of this derivation will be put in terms of the per unit volume quantity (the expression within the integral).

$$\partial_V W = \frac{1}{2} A \cdot J \tag{7.12}$$

We then apply Ampere's law (assuming $\frac{\partial D}{\partial t} = 0$) and the identity $A \cdot (\nabla \times H) = \nabla \cdot (H \times A) + H \cdot (\nabla \times A)$ to get:

$$\partial_V W = \frac{1}{2} [\nabla \cdot (H \times A) + H \cdot (\nabla \times A)] \tag{7.13}$$

Assuming a localized field, the first term in this expression is 0, and the second term is simply $H \cdot B$ (as $\nabla \times A = B$) so:

$$\partial_V W = \frac{1}{2} H \cdot B \tag{7.14}$$

To get power per unit volume (the power density, or P_d), we simply take the time derivative of this expression:

$$\frac{\partial(\partial_V W)}{\partial t} = P_d = \frac{1}{2} \frac{\partial}{\partial t} H \cdot B = \frac{1}{2} \left(\frac{\partial H}{\partial t} \cdot B + H \cdot \frac{\partial B}{\partial t} \right) \tag{7.15}$$

Assuming the material is linear, such that $B = \mu_0 \chi H$ (where $\mu_0 \chi$ is a complex permeability tensor):

$$P_d = H \cdot \frac{\partial B}{\partial t} \tag{7.16}$$

Magnetic power absorption

Using 7.16 from the previous section, we can then derive the magnetic power absorption. Assuming a plane wave ansatz for H and B ($H = H_0 e^{j\omega t}$), P_d can be rewritten simply as:

$$P_d = H \cdot \frac{\partial B}{\partial t} = H \cdot j\omega B \tag{7.17}$$

Since we are interested in the time-averaged case, we can take the time average and apply the time average theorem to obtain:

$$\langle P_d \rangle = \langle H \cdot j\omega B \rangle = \frac{1}{2} Re \{ H_0^* j\omega B_0 \} \tag{7.18}$$

Rewriting $B_0 = \mu_0 \chi H_0$, and pulling the real scalar ω outside the braces:

$$\langle P_d \rangle = \frac{1}{2} Re\left\{H_0^* j\omega\mu_0\chi H_0\right\} = \frac{\omega}{2} Re\left\{H_0^* j\mu_0\chi H_0\right\} \tag{7.19}$$

Then we can use $Re\{jA\} = -Im\{A\}$, and integrate over the volume to get the total absorbed power:

$$\langle P_{abs} \rangle = -\frac{\omega\mu_0}{2} \iiint_V Im\left\{H_0^* \chi H_0\right\} dV \tag{7.20}$$

For the applied magnetic field H_0 in Eq. 7.20 we insert the calculated magnetoelastic drive field calculated in section 2.2. For clarity, the equations for magnetoelastic driving field as a function of film strain (Eq. 2.9 and 2.10) have been reproduced below.

$$\begin{aligned} \mu_0 H^d_{eff,1} = -\frac{\partial G^d}{\partial m_1}|_{m_0} = \\ 2b_1 \cos(\theta_0)\sin(\theta_0)[\cos(\phi_0)^2\varepsilon_{xx} + \sin(\phi_0)^2\varepsilon_{yy} - \varepsilon_{zz}] \\ +2b_2[\cos(\theta_0)^2(\cos(\phi_0)\varepsilon_{xz} + \sin(\phi_0)\varepsilon_{yz}) \\ -\sin(\theta_0)^2(\cos(\phi_0)\varepsilon_{xz} + \sin(\phi_0)\varepsilon_{yz}) \\ +\cos(\theta_0)\sin(\theta_0)\sin(2\phi_0)\varepsilon_{xy}] \end{aligned} \tag{7.21}$$

$$\begin{aligned} \mu_0 H^d_{eff,2} = -\frac{\partial G^d}{\partial m_2}|_{m_0} = \\ 2b_1 \cos(\phi_0)\sin(\phi_0)\sin(\theta_0)[\varepsilon_{yy} - \varepsilon_{xx}] \\ +2b_2[\cos(\theta_0)(\cos(\phi_0)\varepsilon_{yz} - \sin(\phi_0)\varepsilon_{xz}) \\ +\sin(\theta_0)\cos(2\phi_0)\varepsilon_{xy}] \end{aligned} \tag{7.22}$$

For our case, these equations can be further simplified by applying the following: (1) we restrict our case to in-plane sweeps of the magnetization, so $\theta_0 = \frac{\pi}{2}$ (2) our magnetic films are polycrystalline, so $b_1 = b_2 = B_{eff}$ and (3) due to our use of Y-cut, Z-propagating $LiNbO_3$, we assume the propagating SAWs are Rayleigh waves, and thus have a dominant ε_{xx} component, allowing us to set all other strains components to 0. This allows us to rewrite $\mathbf{H_{eff}}$ as:

$$\mu_0 \mathbf{H^d_{eff}} = \begin{pmatrix} 0 \\ -2B_{eff}\cos(\phi_0)\sin(\phi_0)\varepsilon_{xx} \end{pmatrix} \tag{7.23}$$

Surface train due to surface acoustic waves

Next we calculate the strain in the $LiNbO_3$. Perpendicular displacement in the substrate can be written as[84]:

$$\frac{P_{SAW}}{W} = M\omega u_z^2 \tag{7.24}$$

Where P_{SAW} is the SAW power, W is the width of the beam, M is a calculated material constant, ω is 2π times the SAW frequency and u_z is the perpendicular component of the displacement. For Y-cut, Z-propagating lithium niobate, $u_x \approx \frac{2}{3}u_z$.[94] Assuming a plane-wave ansatz for u_x ($u_x \propto e^{ikx}$), and since $\varepsilon_{xx} = \frac{\partial u_x}{\partial x}$, we can write:

$$|\varepsilon_{xx}| = k|u_x| = \frac{2}{3}k\sqrt{\frac{P_{SAW}}{WM\omega}} \tag{7.25}$$

Coefficient extraction from measured data

Finally, we can combine equations 7.20, 7.23, and 7.25 to obtain an equation for the magnetoelastic coefficient (B_{eff}) of our thin film. First, we can simplify equation 7.20 by noting that $\mathbf{H_{eff}}$ only has one non-zero term, and by assuming that the strain (ε_{xx}) is uniform along the y and z directions (those perpendicular to the SAW propagation direction), since the film is very thin compared to the SAW wavelength and since we are using an IDT structure that creates a constant strain profile along its width. Since we know that power is absorbed along the x (SAW propagation) direction from the results in Section 3.3, we must integrate the driving field along this direction. This lets us write:

$$P_{abs} = \frac{\mu_0\omega}{2} Im\left\{\chi_{22}\right\} A \int_0^L |\mathbf{H_{eff}^d}(x)|^2 dx \tag{7.26}$$

Here A is the film cross-sectional area and L is its length along the x (SAW propagation) direction. We can then plug equation 7.23 into equation 7.26 and pull the constant terms out of the integral to get:

$$P_{abs} = 2B_{eff}^2\mu_0\omega\cos(\phi_0)^2\sin(\phi_0)^2 Im\left\{\chi_{22}\right\} A \int_0^L |\varepsilon_{xx}(x)|^2 dx \tag{7.27}$$

We then plug equation 7.25 into 7.27 to obtain:

$$P_{abs} = \frac{8\mu_0 k^2 B_{eff}^2\cos(\phi_0)^2\sin(\phi_0)^2}{9WM} Im\left\{\chi_{22}\right\} A \int_0^L P_{SAW}(x) dx \tag{7.28}$$

Since we know that the power absorption in these films is an exponential function of film length, we can rewrite the above integral as:

$$P_{abs} = \frac{8\mu_0 k^2 B_{eff}^2\cos(\phi_0)^2\sin(\phi_0)^2}{9WM} Im\left\{\chi_{22}\right\} P_{SAW,0} A \int_0^L e^{\frac{-x}{l_0}} dx \tag{7.29}$$

Where $P_{SAW,0}$ is the SAW power at the edge of the magnetic film nearest the input IDT, and l_0 is the characteristic decay length for the relevant film (which depends on film composition, film thickness, excitation frequency, etc. and is an experimentally determined

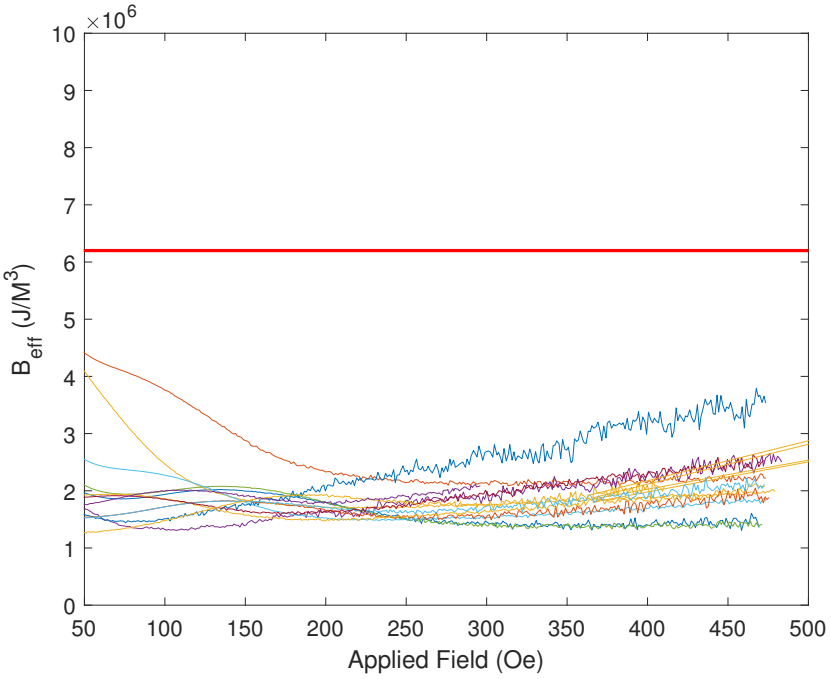

Figure 7.8: Extracted magnetoelastic coupling coefficient values showing negligible field dependence and extremely tight grouping around 1.81 MJ/m^3. The thick red line indicates the standard literature value of 6.2 MJ/m^3, which is approximately a factor of three larger than the experimentally extracted value.

quantity) over which the power decays by a factor of 1/e. Since P_{abs} / $P_{SAW} = 1 - |S_{21}|^2$, we can solve this equation for B_{eff}:

$$B_{eff} = \frac{3}{2k\cos(\phi_0)\sin(\phi_0)}\sqrt{\frac{(1-|S_{21}|^2)MW}{2Al_0\mu_0(1-e^{-L/l_0})Im\{\chi_{22}\}}} \tag{7.30}$$

Calculating magnetoelastic coefficient from experimental data

The equation from the end of the previous section was then used to extract the magnetoelastic coefficient from experimental data. Once the absorption profiles were collected, the damping coefficient was fit by using the equations from Gowtham et. al[35] as described in Section 7.2. A line cut was taken then at the angle of highest absorption (as depicted in Figure 3.6). Equation 7.30 was then evaluated at each point along that line cut. A plot of the calculated magnetoelastic coefficient for an assortment of films measured across the entire available frequency range can be seen in Figure 7.8. As can be seen, the extracted values are constant across applied magnetic field as expected.

Table 7.2: Extracted Ni Magnetoelastic coefficients (MJ/m^3)

	1430 MHz	2000 MHz	2565 MHz
10 nm	1.88	1.78	1.83
20 nm	2.05	2.04	1.75
30 nm	1.94	1.78	1.64
40 nm	1.98	1.80	1.46
50 nm	1.89	1.81	1.46

A compilation of the values determined from the fitting can be found in Table 7.2. The extracted values for magnetoelastic coupling coefficient were extremely well grouped, with the standard deviation of the values being only 0.17 MJ/m^3. The average value extracted from this data is ≈ 1.81 MJ/m^3, which is roughly a factor of 3 lower than the value observed for nickel's magnetoelastic coupling coefficient ($\approx 6.2 MJ/m^3$).[21, 97] Further studies will have to focus on various combinations of piezoelectric/ferromagnet heterostructure to understand the underlying physics of reduced coupling coefficient.

Chapter 8

Summary and outlook

In this work, we have investigated the phenomenon of acoustically driven ferromagnetic resonance and have considered a number of potential device applications for the technology. Here we conclude with a brief summary of the major results and give an outlook for future work in the field. With a continuation of this research, it should be possible to not only further understand the ADFMR effect itself, but to also leverage it as a tool for gaining insight into other fields and systems.

Summary of this thesis

Chapter two of this thesis was largely a summary of the existing techniques and knowledge that combine to make our investigations into ADFMR possible. In this chapter, we first consider the generic phenomenon of ferromagnetic resonance - its characteristics, its usefulness, and its driving physics. We then discuss how a time-varying strain in a magnetoelastic ferromagnet is capable of generating an RF 'tickle' field, as is required to drive FMR. This magneto-acoustic coupling is at the heart of ADFMR, and is responsible for the majority of its unique characteristics. The third section of this chapter then integrates this thus-far theoretical concept with industry-standard surface acoustic wave devices. A number of well-known optimization techniques for designing (impedance-matching) and measuring (time-gating) such devices are then discussed, with the goal of enabling the reader to easily design and test efficient ADFMR devices as easily as possible.

The next chapter of this thesis discusses our work in characterizing the behavior of the field-dependent power absorption when a number of different device parameters are changed. Chapter 3 details of the sample fabrication (including IDT design parameters) are laid out. Next, the measurement system is described in detail in order to ease the design of a similar system in the future. In addition, a description is included of how the field-independent insertion loss of our IDTs (which run at high harmonics and thus have a high insertion loss) is removed. A brief summary of the general shape and properties of ADFMR absorption patterns follows. The remainder of the chapter focuses on experimental results when different device variables are modified. First, it was determined that over a large range of input powers

($>$ 65 dB) the device performance was verified to remain linear. Further work then showed an exponential dependence (linear in dB) of absorption on magnetic element length in the direction of the SAW propagation. The dependence of absorption on thickness, however, was found to show a saturating behavior outside of the ultrathin ($<$ 20 nm) regime. This examination provides us with a number of now well-understood design variables that can be modified to tailor the device absorption properties to better suit a variety of device applications.

Magnetic sensing as a potential device application for ADFMR is explored in detail in Chapter 4. First a summary of current state of the art magnetometers is presented, and the ADFMR magnetometer is shown to be competitive, if not strictly superior, to competing state-of-the-art devices. The sensitivity of the proposed magnetometer is then discussed, and found to be at least 1000 times better than the current best solid-state sensor, the magnetic tunnel junction. Next, a fabrication process flow is outlined for a combined magnetometer / gradiometer based on this technology. Finally, the noise factors in this system are examined and found to be in the range of the best available commercial sensors.

The next chapter in this thesis discusses the potential for using ADFMR for antenna applications. Chapter 5 begins with an examination of the difficulties with conventional electrically small antennas (that is, those whose size is substantially smaller than the free space wavelength of the radiated electromagnetic waves) , and then explores the potential to use multiferroic antennas to overcome these complications. Such antennas leverage the efficiency of the magnetoelastic driving field in order to rotate magnetic dipoles and generate far-field radiation. We then consider complications induced by the small-wavelength variations in the phase of the magnetoelastic driving field and how they impact far field radiation. It is shown that patterning of the magnetic film in ADFMR devices is necessary (and effective) to obtain meaningful radiation from such a system.

Chapter 6 examines a final potential application for this technology in its ability to couple to nitrogen vacancy centers in diamond. Such coupling could enable devices as varied as room temperature quantum computers and integrated atomic clocks. A brief overview of nitrogen vacancy centers and off-resonant coupling to such defect centers via proximal resonating ferromagnet is is presented. We then show experimental results wherein we are able to observe strong coupling between diamond NV centers and ADFMR devices using both nickel and cobalt films. Surprisingly, we observe a similar magnitude of NV coupling between both nickel and cobalt systems, despite the fact that they show extremely different acoustic absorption profiles. This result reinforces the need for continued study of the combined system, as it holds the potential to enhance our understanding of both ADFMR and off-resonant NV center coupling. We demonstrate a zero-field, on-chip method to couple an AC input voltage with the NV center spin state - paving the way for meaningful device applications relying on this technology.

The final content chapter of this thesis discusses the various characterization methods used to determine the magnetic properties of the films used in the ADFMR devices. It covers the use of techniques such as vibrating sample magnetometry and anisotropic magnetoresistance to extract saturation magnetization, in-plane anisotropy, and effective magnetization

parameters. Chapter 7 also includes a description of the formalism used to extract the damping and magnetoelastic coefficients. We find that the extracted magnetoelastic coefficient for the Ni films used in this work is independent of film thickness and excitation frequency as expected. Film damping, however, is seen to increase once films exceed a thickness of $\approx$ 20 nm, corresponding to the onset of absorption saturation as discussed in Chapter 3. We are able to use existing models for ADFMR to model this absorption saturation when the damping enhancement is taken into account.

Outlook for future work

While the phenomenon of acoustically driven ferromagnetic resonance has seen substantial investigation in recent years, a number of fundamental properties remain unexplained. All experimental work on this topic, on a variety of materials systems, has seen substantial damping enhancement. A number of potential mechanisms have been proposed for the origin of this increase in damping, but as of yet, none have been experimentally verified. The observed damping is approximately an order of magnitude larger than that seen in the intrinsic magnetic films, limiting the usefulness of this technique as a technique for the generation of magnetic excitations. It is critical to determine whether this property is intrinsically tied to the magnetoelastic drive, or if it can be controlled by modifying the composition or shape of the magnetic film. If this linewidth broadening proves to be unresolvable, it would severely limit the potential device applications of this system.

Another fundamental question that remains to be answered with regards to acoustically driven FMR is an understanding of how the absorption magnitude scales with different materials systems. Measurements of cobalt and nickel films, for example, show that cobalt actually absorbs less SAW power than nickel, despite the fact that current theory predicts the opposite. Interestingly, despite the large difference in absorption magnitude, both films couple to diamond NV centers in a comparable way, showing that perhaps there is more going on than a simple relation between magnetization oscillation and absorbed power. A systematic study of a variety of materials with varying M_s and B_{eff} values would allow for a more thorough investigation of the dependence of absorption on these parameters, and could lead to the develop of a more accurate expression for power absorption and magnetization change in these films.

In our work on developing ADFMR as a potential far-field antenna mechanism, we quickly discovered that the periodic phase variation (with a period on the order of μm) inherent to the SAW drive would basically eliminate any far-field radiation from the device. This issue could be solved by using a patterning mechanism such as the one illustrated in Figure 8.1, but this turns out to not be a simple experiment to perform. For this patterning technique to work, the magnetic film must be deposited into a spatially periodic array with a period equal to the wavelength of the SAW. This is more difficult than it may seem at first glance due to the fact that SAWs are strongly reflected by any periodic conductive structure on the surface of the substrate. Thus, in order to develop an effective patterned system, a magnetic oxide must be used as the active magnetoelastic layer. Such systems are extremely sensitive

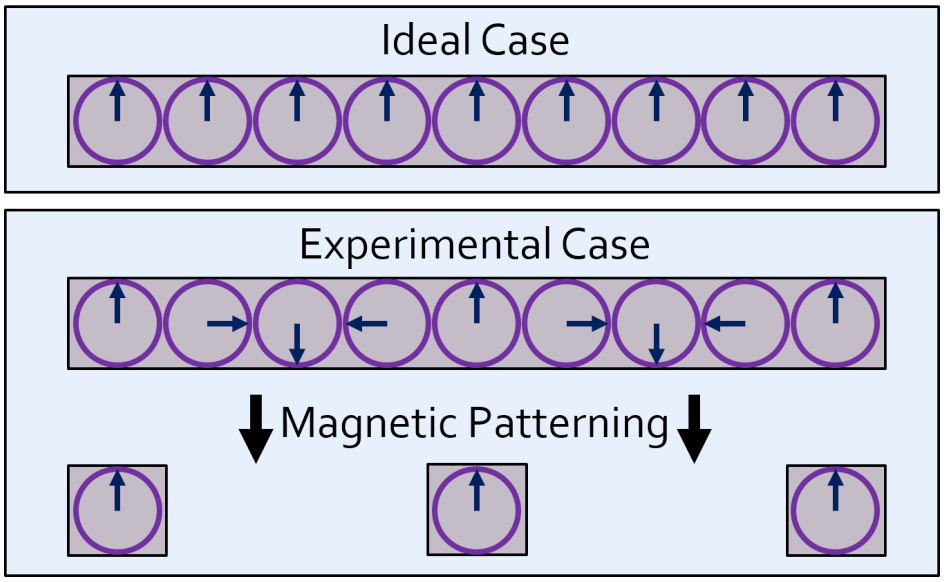

Figure 8.1: A comparison of phase as a function of locations for the ideal case for radiation (entirely coherent) and the experimental case (period phase difference). The experimental case could potentially be made to radiate similarly to the ideal case if patterning were performed to only create rotating magnetic dipoles at certain spatial positions (so that they could all be made to be in phase).

to crystallinity, and thus deposition of a high-quality magnetic oxide on our lithium niobate substrate is not a trivial task. Alternatively, if a conductive magnetoelastic film could be periodically doped or otherwise modified to reduce the magnetostriction / magnetization in certain areas without substantially altering the conductivity, this could also be an avenue to achieving the required patterning. If such a system could be fabricated, however, it would be extremely interesting to investigate the effects of such magnetic periodicity on the far-field electromagnetic radiation of the SAW-driven ADFMR system.

Our collaborative work with coupling ADFMR to diamond NV centers has also exposed an opportunity for substantial future work on the subject. We have observed clear coupling between both nickel and cobalt magnets driven by ADFMR and NV centers at power levels several orders of magnitude below those used in traditional NV experiments. This has already exposed a surprising difference in the ratio of observed power absorption to NV modulation in nickel and cobalt, and the potential to use NV centers as local field sensors would allow for the quantification of the true efficiency of the ADFMR process in exciting magnetization precession. In addition, the ability of ADFMR to generate spin waves with a wavevector locked to that of the acoustic wave provides an avenue to more precisely probe the nature of the off-resonant coupling between spin waves and NV centers in diamond. This combined system has not only the potential to be useful in quantum computing applications, but is actually capable of exposing some fascinating fundamental physics due to the unique

strengths and capabilities of each of the underlying components.

Acoustically driven ferromagnetic resonance has, in the few years since it's first experimental confirmation, shown itself to be an extremely capable system for both device applications and fundamental scientific inquiry. The ability to drastically enhance the efficiency of FMR, integrate it into an on-chip form factor, and couple magnetization precession to external systems bodes well for its adoption into commercially-relevant technologies. Meanwhile, the system shows true depth as an interesting problem from the perspective of physics, with thus-far unexplained deviations from expected ferromagnetic (and spin-wave) resonance behaviors. This thesis is but a small contribution to the overall understanding of this complex system, which I believe has the ability to not only make a meaningful impact on the scientific study of magnetism, but also to enable a variety of magnetic technologies that can benefit the world in substantial and tangible ways.

Bibliography

[1] Tianxiang Nan et. al. "Acoustically actuated ultra-compact NEMS magnetoelectric antennas". In: *Nature Communications* 8.296 (2017).

[2] Roland Albrecht et al. "Narrow-band single photon emission at room temperature based on a single nitrogen-vacancy center coupled to an all-fiber-cavity". In: *Applied Physics Letters* 105.7 (2014), p. 073113.

[3] JM Almeida et al. "1/ f noise in linearized low resistance MgO magnetic tunnel junctions". In: *Journal of applied physics* 99.8 (2006), 08B314.

[4] Richard A Armstrong and B Janday. "A brief review of magnetic fields from the human visual system". In: *Ophthalmic and Physiological Optics* 9.3 (1989), pp. 299–301.

[5] Constantine A Balanis. "Antenna theory: A review". In: *Proceedings of the IEEE* 80.1 (1992), pp. 7–23.

[6] N Bloembergen and RV Pound. "Radiation damping in magnetic resonance experiments". In: *Physical Review* 95.1 (1954), p. 8.

[7] Stephen Blundell. "Magnetism in Condensed Matter". In: (2001).

[8] Aaron Canciani and John Raquet. "Absolute positioning using the Earth's magnetic anomaly field". In: *Navigation* 63.2 (2016), pp. 111–126.

[9] Aaron Canciani and John Raquet. "Airborne magnetic anomaly navigation". In: *IEEE Transactions on Aerospace and Electronic Systems* 53.1 (2017), pp. 67–80.

[10] David Chandler. "Introduction to modern statistical mechanics". In: *Introduction to Modern Statistical Mechanics, by David Chandler, pp. 288. Foreword by David Chandler. Oxford University Press, Sep 1987. ISBN-10: 0195042778. ISBN-13: 9780195042771* (1987), p. 288.

[11] RC Chaves et al. "Low frequency picotesla field detection using hybrid MgO based tunnel sensors". In: *Applied Physics Letters* 91.10 (2007), p. 102504.

[12] C Chen et al. "Voltage induced mechanical/spin wave propagation over long distances". In: *Applied Physics Letters* 110.7 (2017), p. 072401.

[13] Sergiy Cherepov et al. "Electric-field-induced spin wave generation using multiferroic magnetoelectric cells". In: *Applied Physics Letters* 104.8 (2014), p. 082403.

[14] Soshin Chikazumi and Chad D Graham. *Physics of Ferromagnetism 2e*. 94. Oxford University Press, 2009.

[15] Lan Jen Chu. "Physical limitations of omni-directional antennas". In: *Journal of applied physics* 19.12 (1948), pp. 1163–1175.

[16] Ying-Hao Chu et al. "Electric-field control of local ferromagnetism using a magnetoelectric multiferroic". In: *Nature materials* 7.6 (2008), p. 478.

[17] Ki Chul Chun et al. "A scaling roadmap and performance evaluation of in-plane and perpendicular MTJ based STT-MRAMs for high-density cache memory". In: *IEEE Journal of Solid-State Circuits* 48.2 (2013), pp. 598–610.

[18] David Cohen. "Magnetoencephalography: detection of the brain's electrical activity with a superconducting magnetometer". In: *Science* 175.4022 (1972), pp. 664–666.

[19] David Cohen et al. "Magnetoencephalography: evidence of magnetic fields produced by alpha-rhythm currents". In: *Science* 161.3843 (1968), pp. 784–786.

[20] JH Collins et al. "Unidirectional surface wave transducer". In: *Proceedings of the IEEE* 57.5 (1969), pp. 833–835.

[21] Bernard Dennis Cullity and Chad D Graham. *Introduction to magnetic materials*. John Wiley & Sons, 2011.

[22] A D'amico, A Palma, and E Verona. "Surface acoustic wave hydrogen sensor". In: *Sensors and Actuators* 3 (1982), pp. 31–39.

[23] B Desormière, E Milot, and H Le Gall. "Transient processes in spin-wave systems with magnetic dipole radiation-II. Experimental investigations". In: *Journal of Physics and Chemistry of Solids* 30.5 (1969), pp. 1135–1146.

[24] Michał Dkabek et al. "Sensitivity and 3 dB Bandwidth in Single and Series-Connected Tunneling Magnetoresistive Sensors". In: *Sensors* 16.11 (2016), p. 1821.

[25] Marcus W Doherty et al. "Electronic properties and metrology applications of the diamond NV- center under pressure". In: *Physical review letters* 112.4 (2014), p. 047601.

[26] Marcus W Doherty et al. "The nitrogen-vacancy colour centre in diamond". In: *Physics Reports* 528.1 (2013), pp. 1–45.

[27] L. Dreher et al. "Surface acoustic wave driven ferromagnetic resonance in nickel thin films: Theory and experiment". In: *Phys. Rev. B* 86 (13 Oct. 2012), p. 134415.

[28] Chunhui Du et al. "Control and local measurement of the spin chemical potential in a magnetic insulator". In: *Science* 357.6347 (2017), pp. 195–198.

[29] Marc-Alexandre Dubois and Claude Muller. "Thin-Film Bulk Acoustic Wave Resonators". In: *MEMS-based Circuits and Systems for Wireless Communication*. Springer, 2013, pp. 3–28.

[30] WF Egelhoff et al. "Critical challenges for picoTesla magnetic-tunnel-junction sensors". In: *Sensors and Actuators A: Physical* 155.2 (2009), pp. 217–225.

[31] Michael Farle. "Ferromagnetic resonance of ultrathin metallic layers". In: *Reports on Progress in Physics* 61.7 (1998), p. 755.

[32] Riccardo Fenici, Donatella Brisinda, and Anna Maria Meloni. "Clinical application of magnetocardiography". In: *Expert review of molecular diagnostics* 5.3 (2005), pp. 291–313.

[33] Thomas L Gilbert. "A phenomenological theory of damping in ferromagnetic materials". In: *IEEE Transactions on Magnetics* 40.6 (2004), pp. 3443–3449.

[34] Praveen G Gowtham, Dominic Labanowski, and Sayeef Salahuddin. "Mechanical back-action of a spin-wave resonance in a magnetoelastic thin film on a surface acoustic wave". In: *Physical Review B* 94.1 (2016), p. 014436.

[35] Praveen G Gowtham et al. "Traveling surface spin-wave resonance spectroscopy using surface acoustic waves". In: *Journal of Applied Physics* 118.23 (2015), p. 233910.

[36] Edward Grochowski and Robert D Halem. "Technological impact of magnetic hard disk drives on storage systems". In: *IBM Systems Journal* 42.2 (2003), pp. 338–346.

[37] Qiaochu Guo. "Optical Detection of Acoustically Driven Ferromagnetic Resonance". PhD thesis. The Ohio State University, 2017.

[38] Matti Hämäläinen et al. "Magnetoencephalography theory, instrumentation, and applications to noninvasive studies of the working human brain". In: *Reviews of modern Physics* 65.2 (1993), p. 413.

[39] Roger F Harrington. "Effect of antenna size on gain, bandwidth, and efficiency". In: *J. Res. Nat. Bur. Stand* 64.1 (1960), pp. 1–12.

[40] Joanne Harrison, MJ Sellars, and NB Manson. "Measurement of the optically induced spin polarisation of NV centres in diamond". In: *Diamond and related materials* 15.4 (2006), pp. 586–588.

[41] JT Heron et al. "Electric-field-induced magnetization reversal in a ferromagnet-multiferroic heterostructure". In: *Physical review letters* 107.21 (2011), p. 217202.

[42] Melvin G Holland and Lewis T Claiborne. "Practical surface acoustic wave devices". In: *Proceedings of the IEEE* 62.5 (1974), pp. 582–611.

[43] Sungkun Hong et al. "Nanoscale magnetometry with NV centers in diamond". In: *MRS bulletin* 38.2 (2013), pp. 155–161.

[44] Jia-Mian Hu et al. "Design of a Voltage-Controlled Magnetic Random Access Memory Based on Anisotropic Magnetoresistance in a Single Magnetic Layer". In: *Advanced Materials* 24.21 (2012), pp. 2869–2873.

[45] Jia-Mian Hu et al. "Electric-field control of strain-mediated magnetoelectric random access memory". In: *Journal of Applied Physics* 107.9 (2010), p. 093912.

[46] Jia-Mian Hu et al. "High-density magnetoresistive random access memory operating at ultralow voltage at room temperature". In: *Nature communications* 2 (2011), p. 553.

[47] Kevin Hung, Yuan-Ting Zhang, and B Tai. "Wearable medical devices for tele-home healthcare". In: *Engineering in Medicine and Biology Society, 2004. IEMBS'04. 26th Annual International Conference of the IEEE*. Vol. 2. IEEE. 2004, pp. 5384–5387.

[48] S Ikeda et al. "A perpendicular-anisotropy CoFeB–MgO magnetic tunnel junction". In: *Nature materials* 9.9 (2010), pp. 721–724.

[49] K Iramina et al. "Measurements of biomagnetic fields using a high-resolution dc superconducting quantum interference device magnetometer". In: *Journal of applied physics* 83.11 (1998), pp. 6465–6467.

[50] KD Jahnke et al. "Long coherence time of spin qubits in 12C enriched polycrystalline chemical vapor deposition diamond". In: *Applied physics letters* 101.1 (2012), p. 012405.

[51] John Bertrand Johnson. "Thermal agitation of electricity in conductors". In: *Physical review* 32.1 (1928), p. 97.

[52] Sangita S Kalarickal et al. "Ferromagnetic resonance linewidth in metallic thin films: Comparison of measurement methods". In: *Journal of Applied Physics* 99.9 (2006), p. 093909.

[53] Charles Kittel. *Introduction to solid state physics*. Wiley, 2005.

[54] T. Kobayashi et al. "Ferromagnetoelastic Resonance in Thin Films. I. Formal Treatment". In: *Phys. Rev. B* 7 (7 Apr. 1973), pp. 3273–3285.

[55] Hans Koch. "Recent advances in magnetocardiography". In: *Journal of electrocardiology* 37 (2004), pp. 117–122.

[56] IK Kominis et al. "A subfemtotesla multichannel atomic magnetometer". In: *Nature* 422.6932 (2003), pp. 596–599.

[57] Georg Kucsko et al. "Nanometer scale thermometry in a living cell". In: *Nature* 500.7460 (2013), p. 54.

[58] D Labanowski, A Jung, and S Salahuddin. "Power absorption in acoustically driven ferromagnetic resonance". In: *Applied Physics Letters* 108.2 (2016), p. 022905.

[59] Kerstin Länge, Bastian E Rapp, and Michael Rapp. "Surface acoustic wave biosensors: a review". In: *Analytical and bioanalytical chemistry* 391.5 (2008), pp. 1509–1519.

[60] K Langecker and R Veith. "Automatic time domain testing of SAW devices". In: *1980 Ultrasonics Symposium*. IEEE. 1980, pp. 396–399.

[61] Joseph Larmor. "A dynamical theory of the electric and luminiferous medium". In: *Philosophical Transactions of the Royal Society of London. A* 185 (1894), pp. 719–822.

[62] Xu Li et al. "Spin wave generation by surface acoustic waves". In: *Journal of Applied Physics* 122.4 (2017), p. 043904.

[63] Cheng-Yen Liang et al. "Electrical control of a single magnetoelastic domain structure on a clamped piezoelectric thin film-analysis". In: *Journal of Applied Physics* 116.12 (2014), p. 123909.

[64] Luqiao Liu et al. "Spin-torque ferromagnetic resonance induced by the spin Hall effect". In: *Physical review letters* 106.3 (2011), p. 036601.

[65] Van-Su Luong et al. "Reduction of low-frequency noise in tunneling-magnetoresistance sensors with a modulated magnetic shielding". In: *IEEE Transactions on Magnetics* 50.11 (2014), pp. 1–4.

[66] Thomas Martin, Emil Jovanov, and Dejan Raskovic. "Issues in wearable computing for medical monitoring applications: a case study of a wearable ECG monitoring device". In: *Wearable Computers, The Fourth International Symposium on*. IEEE. 2000, pp. 43–49.

[67] JR Maze et al. "Properties of nitrogen-vacancy centers in diamond: the group theoretic approach". In: *New Journal of Physics* 13.2 (2011), p. 025025.

[68] Dipanjan Mazumdar et al. "Low frequency noise in highly sensitive magnetic tunnel junctions with (001) MgO tunnel barrier". In: *Applied Physics Letters* 91.3 (2007), p. 033507.

[69] RF Mitchell and DW Parker. "Synthesis of acoustic-surface-wave filters using double electrodes". In: *Electronics Letters* 10.24 (1974), pp. 512–512.

[70] E Montarroyos and SM Rezende. "Radiation damping of magnetostatic modes in yig". In: *Solid State Communications* 19.8 (1976), pp. 795–798.

[71] David P Morgan. *Surface-wave devices for signal processing*. North-Holland, 1991.

[72] Hiroshi Nosé. "Exchange integral in Ni and its alloy film from spin wave resonance". In: *Journal of the Physical Society of Japan* 16.12 (1961), pp. 2475–2481.

[73] Sophocles J Orfanidis. *Electromagnetic waves and antennas*. Rutgers University New Brunswick, NJ, 2002.

[74] Michael R Page et al. "Optically Detected Ferromagnetic Resonance in Metallic Ferromagnets via Nitrogen Vacancy Centers in Diamond". In: *arXiv preprint arXiv:1607.07485* (2016).

[75] Alexandros Pantelopoulos and Nikolaos Bourbakis. "A survey on wearable biosensor systems for health monitoring". In: *Engineering in Medicine and Biology Society, 2008. EMBS 2008. 30th Annual International Conference of the IEEE*. IEEE. 2008, pp. 4887–4890.

[76] Alexandros Pantelopoulos and Nikolaos G Bourbakis. "A survey on wearable sensor-based systems for health monitoring and prognosis". In: *IEEE Transactions on Systems, Man, and Cybernetics, Part C (Applications and Reviews)* 40.1 (2010), pp. 1–12.

[77] David P. Pappas. *High sensitivity magnetic field sensor technology overview*. 2007.

[78] SSP Parkin et al. "Exchange-Biased Magnetic Tunnel Junctions and Application to Nonvolatile Magnetic Random Access Memory (invited)". In: *J. Appl. Phys* 85 (), pp. 5828–5833.

[79] Matthias Pernpeinter. *Magnon-Phonon Coupling in Ferromagnetic Thin Films*. Walther-Meissner-Institute for Low Temperature Research, 2012.

[80] Robert Plonsey. "Capability and limitations of electrocardiography and magnetocardiography". In: *IEEE Transactions on Biomedical Engineering* 3 (1972), pp. 239–244.

[81] Ramaroorthy Ramesh and Nicola A Spaldin. "Multiferroics: progress and prospects in thin films". In: *Nature materials* 6.1 (2007), pp. 21–29.

[82] Sergio M Rezendet, Edmundo Soares, and Vincent Jaccarino. "Radiation induced broadening of the FMR and AFMR uniform modes". In: *AIP Conference Proceedings*. Vol. 18. 1. AIP. 1974, pp. 1083–1087.

[83] Pavel Ripka. "Advances in fluxgate sensors". In: *Sensors and Actuators A: Physical* 106.1 (2003), pp. 8–14.

[84] William P Robbins. "A Simple Method of Approximating Surface Acoustic Wave Power Densities". In: *Sonics and Ultrasonics, IEEE Transactions on* 24.5 (1977), pp. 339–339.

[85] L Rondin et al. "Magnetometry with nitrogen-vacancy defects in diamond". In: *Reports on progress in physics* 77.5 (2014), p. 056503.

[86] RW Sanders et al. "Radiation damping in magnetic resonance. II. Continuous-wave antiferromagnetic-resonance experiments". In: *Physical Review B* 10.1 (1974), p. 132.

[87] Adarsh Sandhu et al. "High sensitivity InSb ultra-thin film micro-Hall sensors for bioscreening applications". In: *Japanese journal of applied physics* 43.7A (2004), p. L868.

[88] Romana Schirhagl et al. "Nitrogen-vacancy centers in diamond: nanoscale sensors for physics and biology". In: *Annual review of physical chemistry* 65 (2014), pp. 83–105.

[89] M Schmelz et al. "Thin-Film-Based Ultralow Noise SQUID Magnetometer". In: *IEEE Transactions on Applied Superconductivity* 26.5 (2016), pp. 1–5.

[90] Martin AW Schoen et al. "Ultra-low magnetic damping of a metallic ferromagnet". In: *Nature Physics* 12.9 (2016), pp. 839–842.

[91] SJ Seltzer and MV Romalis. "Unshielded three-axis vector operation of a spin-exchange-relaxation-free atomic magnetometer". In: *Applied physics letters* 85.20 (2004), pp. 4804–4806.

[92] Daniel F Sievenpiper et al. "Experimental validation of performance limits and design guidelines for small antennas". In: *IEEE Transactions on Antennas and Propagation* 60.1 (2012), pp. 8–19.

[93] AJ Slobodnik Jr, PH Carr, and AJ Budreau. "Microwave Frequency Acoustic Surface-Wave Loss Mechanisms on LiNbO3". In: *Journal of Applied Physics* 41.11 (1970), pp. 4380–4387.

[94] AJ Slobodnik Jr, ED Conway, and RT Delmonico. "Microwave acoustics handbook, Vol. 1A, Surface wave velocities". In: *The Journal of the Acoustical Society of America* 56.4 (1974), pp. 1307–1308.

[95] W Richard Smith et al. "Analysis of interdigital surface wave transducers by use of an equivalent circuit model". In: *IEEE Transactions on Microwave Theory and Techniques* 17.11 (1969), pp. 856–864.

[96] W Richard Smith et al. "Design of surface wave delay lines with interdigital transducers". In: *Microwave Theory and Techniques, IEEE Transactions on* 17.11 (1969), pp. 865–873.

[97] Ohsung Song, CA Ballentine, and RC O'Handley. "Giant surface magnetostriction in polycrystalline Ni and NiFe films". In: *Applied physics letters* 64.19 (1994), pp. 2593–2595.

[98] Nicola A Spaldin and Manfred Fiebig. "The renaissance of magnetoelectric multiferroics". In: *Science* 309.5733 (2005), pp. 391–392.

[99] RH Tancrell and MG Holland. "Acoustic surface wave filters". In: *Proceedings of the IEEE* 59.3 (1971), pp. 393–409.

[100] Kunihisa Tashiro et al. "Energy harvesting of magnetic power-line noise". In: *IEEE Transactions on Magnetics* 47.10 (2011), pp. 4441–4444.

[101] Yuan Taur et al. "CMOS scaling into the nanometer regime". In: *Proceedings of the IEEE* 85.4 (1997), pp. 486–504.

[102] L. Thevenard et al. "Surface-acoustic-wave-driven ferromagnetic resonance in (Ga,Mn)(As,P) epilayers". In: *Phys. Rev. B* 90 (9 Sept. 2014), p. 094401.

[103] Morgan Trassin. "Low energy consumption spintronics using multiferroic heterostructures". In: *Journal of Physics: Condensed Matter* 28.3 (2015), p. 033001.

[104] Kenji Uchino. *Advanced piezoelectric materials: Science and technology*. Elsevier, 2010.

[105] K Vad, S Mészáros, and G Halász. "Biomagnetic measurements with a third order gradiometer". In: *Acta Physica Hungarica* 62.1 (1987), pp. 63–66.

[106] Toeno Van der Sar et al. "Nanometre-scale probing of spin waves using single electron spins". In: *Nature communications* 6 (2015).

[107] Peter M Vetoshko, Michael V Valeiko, and Petr I Nikitin. "Epitaxial yttrium iron garnet film as an active medium of an even-harmonic magnetic field transducer". In: *Sensors and Actuators A: Physical* 106.1 (2003), pp. 270–273.

[108] J Vrba and SE Robinson. "SQUID sensor array configurations for magnetoencephalography applications". In: *Superconductor Science and Technology* 15.9 (2002), R51.

[109] J Walowski et al. "Intrinsic and non-local Gilbert damping in polycrystalline nickel studied by Ti: sapphire laser fs spectroscopy". In: *Journal of Physics D: Applied Physics* 41.16 (2008), p. 164016.

[110] JBNJ Wang et al. "Epitaxial BiFeO3 multiferroic thin film heterostructures". In: *science* 299.5613 (2003), pp. 1719–1722.

[111] M. Weiler et al. "Elastically Driven Ferromagnetic Resonance in Nickel Thin Films". In: *Phys. Rev. Lett.* 106 (11 Mar. 2011), p. 117601.

[112] M. Weiler et al. "Spin Pumping with Coherent Elastic Waves". In: *Phys. Rev. Lett.* 108 (17 Apr. 2012), p. 176601.

[113] Harold A Wheeler. "Fundamental limitations of small antennas". In: *Proceedings of the IRE* 35.12 (1947), pp. 1479–1484.

[114] William C Wilson and Gary M Atkinson. "1st Order Modeling of a SAW Delay Line using MathCAD". In: (2007).

[115] Chris S Wolfe et al. "Off-resonant manipulation of spins in diamond via precessing magnetization of a proximal ferromagnet". In: *Physical Review B* 89.18 (2014), p. 180406.

[116] CS Wolfe et al. "Spatially resolved detection of complex ferromagnetic dynamics using optically detected nitrogen-vacancy spins". In: *Applied Physics Letters* 108.23 (2016), p. 232409.

[117] Janik Wolters et al. "Nitrogen Vacancy Centers in Diamond for Quantum Information Processing on Hybrid Platforms". In: *Quantum Information and Measurement*. Optical Society of America. 2014, QTh4A–7.

[118] Kazuhiko Yamanouchi, Felix M Nyffeler, and Kimio Shibayama. "Low insertion loss acoustic surface wave filter using group-type unidirectional interdigital transducer". In: *1975 Ultrasonics Symposium*. IEEE. 1975, pp. 317–321.

[119] Zhi Yao and Yuanxun Ethan Wang. "Dynamic analysis of acoustic wave mediated multiferroic radiation via FDTD methods". In: *Antennas and Propagation Society International Symposium (APSURSI), 2014 IEEE*. IEEE. 2014, pp. 731–732.

[120] Zhi Yao et al. "Bulk acoustic wave-mediated multiferroic antennas: Architecture and performance bound". In: *IEEE Transactions on Antennas and Propagation* 63.8 (2015), pp. 3335–3344.

[121] H. Zhou et al. "Multilayer magnetostrictive structure based surface acoustic wave devices". In: *Applied Physics Letters* 104.11, 114101 (2014).